



Università degli Studi di Firenze

FACOLTÀ DI INGEGNERIA

**TESI DI LAUREA SPECIALISTICA IN
INGEGNERIA ELETTRONICA**

**MODEL ORDER REDUCTION IN FULL-WAVE
ANALYSIS OF PHASED ARRAY ANTENNAS**

di Laurent Ntibarikure

Relatori :

Prof. Giuseppe Pelosi

Dr. Ing. Stefano Selleri

Corelatori :

Prof. Dr. Romanus Dyczij-Edlinger

Dr.-Ing. Ortwin Farle

Anno Accademico 2008-2009

SOMMARIO

Lo scopo della presente tesi è di illustrare l'applicazione di tecniche di riduzione della complessità del modello di radiazione di antenne a schiera fasate, simulate con approccio *full-wave* mediante la tecnica degli elementi finiti.

Si sviluppa, inizialmente, la formulazione matematica che permette la trasformazione da campo vicino a campo lontano. Segue un'analisi approfondita del comportamento del campo vicino a fronte di variazioni dell'angolo di puntamento, in vista di una sua approssimazione. Vengono inoltre presentate tecniche di interpolazione polinomiale del funzionale di trasformazione da campo vicino a campo lontano. Infine, il sistema lineare del modello di radiazione, derivato da una formulazione Galerkin-elementi finiti, viene parametrizzato nella direzione di puntamento, operazione che ne permette una riduzione sistematica della complessità. Esempi numerici illustrano il grado di accuratezza ottenuto nella computazione del campo lontano in seguito alle approssimazioni eseguite.

ACKNOWLEDGMENTS

During my stage at the *Lehrstuhl für Teoretische Elektrotechnik*, several persons have contributed to my work and without their support it would have been impossible for me to complete it. That is why I wish to dedicate this section to recognize their support.

I would like to express my sincere gratitude to the professors of my graduate committee: Prof. Giuseppe Pelosi and Dr. Ing. Stefano Selleri, without whom this marvelous experience may have never happened.

I would like to express my deep appreciation to Univ-Prof. Dr. Romanus Dyczij-Edlinger and Dr-Ing. Ortwin Farle, for their guidance, motivation and support during this period.

Special thanks to all the employees, researchers and students at the LTE for their courtesy, the pieces of advice and help they gave me, and most of all for the good times spent together.

I would also like to express my heartfelt gratitude to my family for encouragement and continuous support given throughout my life.

Last but not least I would like to express my appreciation to my sweetheart, Veronica, for her love, patience, support and understanding throughout these difficult and challenging months.

CONTENTS

Acknowledgments	vii
Contents	ix
Introduction	1
1 Near Field to Far Field Transformation	5
1.1 Radiation in a bounded medium	6
1.1.1 Symmetrized form of the Maxwell's equations	9
1.1.2 The wave equation	10
1.1.3 Scalar Huygens' principle	11
1.1.4 Vector Huygens' principle	14
1.2 Scalar near field to far field transformation	19
1.2.1 Computation steps	20
1.2.2 Computations on a bounding sphere	21
1.2.3 Computations on a bounding parallelepiped	31
1.3 Vector near fields to far fields transformations	38
1.3.1 Direct computation of the fields from current sources	38
1.3.2 Near fields to far fields computations	41
1.3.3 Radiation pattern	41
1.3.4 Numerical results	43
2 Low-Rank Approximations for Fields Transformations	49
2.1 Approximations of the near fields	50

2.1.1	Proper orthogonal decomposition	50
2.1.2	Singular value decomposition	51
2.1.3	Space spanned by the scanned near fields	53
2.2	Approximations of the near field to far field operator	67
2.2.1	Polynomial interpolation of the N2F operator	68
2.2.2	Trigonometric polynomials interpolation of the N2F Operator	76
2.3	Low-rank approximations on a bounding parallelepiped	81
3	Model Order Reduction of Phased Array Antennas	83
3.1	The FEM vector Helmholtz formulation	84
3.2	Projection-based model order reduction	89
3.3	Scan and look angles parameterized radiation model	90
3.4	Proper choice of the trial and test spaces	93
3.5	Numerical examples	94
3.5.1	3 by 5 patch antennas array	95
3.5.2	40 dual-polarized tapered slot antennas	109
	Conclusions	113
	References	115

INTRODUCTION

Phased array antennas consist of a stationary spatial disposition of multiple coherently fed antennas that, acting on the phase of the excitations, allow to control the direction of the maximum gain achieved by the whole radiating structure. The array radiation pattern, as a result of far fields constructive and destructive interferences, is dependent on the relative phase shifts between the far fields produced by the antennas or *array elements*. An additional phase shift in the excitations simply modifies the directions of the constructive and destructive interferences, allowing a *beamsteering* operation. Also, variable amplitude control of the excitations is often provided for pattern shaping. [1–5]

These radiating structures are of a great importance in modern radar and communication systems. For example, modern fire control and artillery location radars make use of phased array antennas instead of mechanical beam steering systems, the latter ones having higher reaction times in target tracking and lower times to failure than mechanically fixed ones. Also, current cellular communication systems require, for the base stations, the ability to modify the radiation pattern in order to fit the illuminated zones to the desired ones and, if necessary, to hide undesired interferers by null-steering, that is the synthesis of a destructive interference in the direction of the interferer. These so-called *smart antennas* [6] are currently employed in the modern spatial diversity based communications techniques as the third generation cellular systems.

An accurate prediction of array parameters using numerical methods not only reduces the development cost and design period but also renders invaluable informa-

tion to design engineers. For this purpose, several techniques like the method of moments (MoM), the finite-element method (FEM) and finite-difference time-domain (FDTD) are available. To accurately model the electromagnetic field behavior inside each array element and the mutual coupling between the elements, a three dimensional full-wave analysis is necessary. Furthermore, an accurate analysis of radiation problems is impossible without accurate modeling of the feeding structure. Due to its general formulation and versatility in geometrical modeling, the FEM appears to be the most suitable technique as an analysis tool.

However, the FEM requires very large computational and memory resources to allow fast design process. This is particularly true when the number of input parameters to consider in an effective design is high, and the simulations have to be iterated for each parameters set. Several techniques have been introduced in the last two decades to face this problem. One of them, which will be presented in this thesis, splits the computations in two steps. The first, an *off-line* stage somewhat time and resources consuming but that needs to be run only once, provides an accurately chosen approximated model of the electromagnetic structure analyzed. The second, an *on-line* stage, allows a fast computation of the sought informations in front of variable input parameters, with an error dependent on the approximations made in the first step. These techniques are referred to as the *model order reduction* (MOR) techniques, and they have been successfully employed in multi-parameters wave guiding and scattering problems [26, 27, 33, 37].

The FEM analysis of antenna arrays is typically limited to the near fields surrounding the radiating structure, closing the domain with opportune boundary conditions on an encompassing surface. Thus, near fields to far fields transformations are necessary in order to derive the far fields pattern.

The purpose of the present thesis is to discuss the application of projection-based MOR techniques on frequency domain FEM simulations of planar phased arrays, leaving as inputs the excitations of the array elements and rapidly computing the far fields pattern in front of a beamsteering process. In the first chapter, the electromagnetic radiation basics in a bounded medium will be reviewed, and the near field to

far field transformation will be presented for both scalar and vector fields. Then, in chapter 2, the process of finding a suitable approximation space for the near field to far field transformation will be discussed. Finally, in chapter 3, the radiation model of phased arrays parameterized in the scan and look angles will be constructed, then a projection-based MOR technique will be applied. Two numerical examples validate the approximations performed in the second chapter, and the reduced order models will be compared to the respective full models.

NEAR FIELD TO FAR FIELD TRANSFORMATION

This chapter introduces the radiation from a generic distribution of sources located in a bounded medium, and the computation of the far-zone radiation patterns using the near fields given on a surface enclosing the sources. The fields will be derived by a direct integration of the sources.

As it has been widely used for its simplicity in the evaluation of a suitable approximation space for the reduction of the radiation model, the scalar wave Huygens' principle will be presented to treat the near field to far field transformation (N2F). Then, its formulation for vector fields will be given, being necessary to preserve the full-wave FEM formulation.

1.1 Radiation in a bounded medium

The problem of electromagnetic radiation from a generic distribution of current sources in a bounded medium relies on the solution of the Maxwell's equations [7]

$$\nabla \times \mathbf{E}(\mathbf{r}, t) = -\frac{\partial}{\partial t} \mathbf{B}(\mathbf{r}, t) \quad \text{Faraday's law,} \quad (1.1.1)$$

$$\nabla \times \mathbf{H}(\mathbf{r}, t) = \frac{\partial}{\partial t} \mathbf{D}(\mathbf{r}, t) + \mathbf{J}(\mathbf{r}, t) \quad \text{Maxwell-Ampère's law,} \quad (1.1.2)$$

$$\nabla \cdot \mathbf{D}(\mathbf{r}, t) = \rho(\mathbf{r}, t) \quad \text{Poisson's equation,} \quad (1.1.3)$$

$$\nabla \cdot \mathbf{B}(\mathbf{r}, t) = 0 \quad \text{Gauss' law for magnetism,} \quad (1.1.4)$$

where \mathbf{E} is the *electric field intensity*, which carries the S.I.¹ units $[V/m]$, \mathbf{H} the *magnetic field intensity* in $[A/m]$, \mathbf{D} the *electric displacement* in $[C/m^2]$ (or $[As/m^3]$), \mathbf{B} the *magnetic induction* in $[Wb/m^2]$ (or $[Vs/m^2]$), \mathbf{J} the *electric current density* in $[A/m]$ and ρ the *electric charge density* in $[C/m^3]$ (or $[As/m^3]$). All these values are dependent on the position vector $\mathbf{r} \in \mathbb{R}^3$ and on the time variable $t \in \mathbb{R}$. Combining the divergence of (1.1.2) with (1.1.3), we obtain the *continuity equation*

$$\nabla \cdot \mathbf{J}(\mathbf{r}, t) + \frac{\partial}{\partial t} \rho(\mathbf{r}, t) = 0. \quad (1.1.5)$$

In order to solve this system of first order partial differential equations (PDEs) it is necessary to provide the *boundary conditions* and the *initial conditions*. Furthermore, as the number of equations is less than the number of unknowns, we need to supply the *constitutive relations*, which relates the electric displacement and the magnetic induction to the fields:

$$\mathbf{D}(\mathbf{r}, t) = \bar{\bar{\epsilon}}(\mathbf{r}, t) \cdot \mathbf{E}(\mathbf{r}, t) + \bar{\bar{\xi}}(\mathbf{r}, t) \cdot \mathbf{H}(\mathbf{r}, t), \quad (1.1.6)$$

$$\mathbf{B}(\mathbf{r}, t) = \bar{\bar{\zeta}}(\mathbf{r}, t) \cdot \mathbf{E}(\mathbf{r}, t) + \bar{\bar{\mu}}(\mathbf{r}, t) \cdot \mathbf{H}(\mathbf{r}, t), \quad (1.1.7)$$

where $\bar{\bar{\epsilon}}$, $\bar{\bar{\xi}}$, $\bar{\bar{\zeta}}$ and $\bar{\bar{\mu}}$ are dyadic tensors depending on the material in which the fields exist². Furthermore, in presence of conductive materials, the electric field gives birth to an electric current density

$$\mathbf{J}^c(\mathbf{r}, t) = \bar{\bar{\sigma}}(\mathbf{r}, t) \cdot \mathbf{E}(\mathbf{r}, t) \quad \text{Ohm's law,} \quad (1.1.8)$$

¹ Système International d'unités.

² The constitutive relations in (1.1.6-1.1.7) are stated in a very general form and can represent all the types of media, i.e. *isotropic*, *anisotropic*, *biisotropic* and *bianisotropic*.

where $\overline{\overline{\sigma}}$ is the *electric conductivity* dyadic tensor in $[S/m]$, and the superscript c on $\mathbf{J}^c(\mathbf{r}, t)$ indicates that the current density is induced by the electric field. With this additional equation, the current $\mathbf{J}(\mathbf{r}, t)$ in (1.1.2) is considered to be composed by an induced part, $\mathbf{J}^c(\mathbf{r}, t)$, and by an impressed part, $\mathbf{J}^i(\mathbf{r}, t)$, the latter actually being the source generating the electromagnetic fields.

The boundary conditions ensure the continuity of the fields at the interfaces between different media, and this is stated as³, for a surface interfacing two media,

$$\hat{\mathbf{n}} \times (\mathbf{E}_1(\mathbf{r}, t) - \mathbf{E}_2(\mathbf{r}, t)) = 0, \quad (1.1.9)$$

$$\hat{\mathbf{n}} \times (\mathbf{H}_1(\mathbf{r}, t) - \mathbf{H}_2(\mathbf{r}, t)) = \mathbf{J}_s(\mathbf{r}, t), \quad (1.1.10)$$

$$\hat{\mathbf{n}} \cdot (\mathbf{D}_1(\mathbf{r}, t) - \mathbf{D}_2(\mathbf{r}, t)) = \rho_s(\mathbf{r}, t), \quad (1.1.11)$$

$$\hat{\mathbf{n}} \cdot (\mathbf{B}_1(\mathbf{r}, t) - \mathbf{B}_2(\mathbf{r}, t)) = 0, \quad (1.1.12)$$

where $\hat{\mathbf{n}}$ is the unit vector normal to the surface, inwardly directed to the first region, \mathbf{J}_s and ρ_s the *electric surface current density* in $[A/m]$ and *electric surface charge density* in $[C/m^2]$.

For the radiation problem we need to solve in this chapter, we will consider *isotropic* (*homogeneous*) and *time-invariant* media, for which the dyadics relating the fields to the electric displacement and magnetic induction are scalar values. Thus, the constitutive relations become

$$\mathbf{D}(\mathbf{r}, t) = \epsilon \mathbf{E}(\mathbf{r}, t) = \epsilon_0 \epsilon_r \mathbf{E}(\mathbf{r}, t), \quad (1.1.13)$$

$$\mathbf{B}(\mathbf{r}, t) = \mu \mathbf{H}(\mathbf{r}, t) = \mu_0 \mu_r \mathbf{H}(\mathbf{r}, t), \quad (1.1.14)$$

where the constant $\epsilon_0 = 8.854 \cdot 10^{-12} [F/m]$ is the *free-space permittivity*, ϵ_r the *relative permittivity*, a non-dimensional constant, $\mu_0 = 4\pi \cdot 10^{-7} [H/m]$ is the *free-space permeability* and μ_r the *relative permeability*, also non-dimensional. As we expect electromagnetic waves to be generated from the sources, we note their speed as $c = 1/\sqrt{\epsilon\mu} = c_0/\sqrt{\epsilon_r\mu_r}$ with $c_0 \approx 2.998 \cdot 10^8 [m/s]$ the *free-space speed of light*.

³ The continuity equations (1.1.9-1.1.12) are derived from an integral solution of the Maxwell's equations, assuming a connected volume made by a part of region 1 and a part of region 2, i.e. a closed surface crossing the boundary interface between the two regions.

For the solution of Maxwell's equations there must be also given the initial conditions, that is, the values of the sources and the fields on the boundaries at $t = -\infty$. Our treatment will consider the frequency-domain formulation of the fields invoking the spectral representation of time dependent fields by the *Fourier integral theorem*

$$\psi(\mathbf{r}, t) = \frac{1}{2\pi} \int_{-\infty}^{\infty} \tilde{\psi}(\mathbf{r}, \omega) e^{-j\omega t} d\omega.$$

Applying the *Fourier integral theorem* to the Maxwell's equations (1.1.1-1.1.4) we obtain

$$\nabla \times \tilde{\mathbf{E}}(\mathbf{r}, \omega) = -j\omega \tilde{\mathbf{B}}(\mathbf{r}, \omega), \quad (1.1.15)$$

$$\nabla \times \tilde{\mathbf{H}}(\mathbf{r}, \omega) = j\omega \tilde{\mathbf{D}}(\mathbf{r}, \omega) + \tilde{\mathbf{J}}(\mathbf{r}, \omega), \quad (1.1.16)$$

$$\nabla \cdot \tilde{\mathbf{D}}(\mathbf{r}, \omega) = \tilde{\rho}(\mathbf{r}, \omega), \quad (1.1.17)$$

$$\nabla \cdot \tilde{\mathbf{B}}(\mathbf{r}, \omega) = 0, \quad (1.1.18)$$

and to the continuity equation we obtain

$$\nabla \cdot \tilde{\mathbf{J}}(\mathbf{r}, \omega) + j\omega \tilde{\rho}(\mathbf{r}, \omega) = 0, \quad (1.1.19)$$

where we have used the Fourier integral of the time derivatives relation

$$\frac{\partial}{\partial t} \psi(\mathbf{r}, t) \leftrightarrow j\omega \tilde{\psi}(\mathbf{r}, \omega),$$

ω being the angular frequency ($\omega = 2\pi f$ with f the frequency in [Hz]) and the symbol “ \sim ” over the frequency dependent function $\tilde{\psi}(\mathbf{r}, \omega)$ denotes its spectrum (the *Fourier Transform*)

$$\tilde{\psi}(\mathbf{r}, \omega) = \int_{-\infty}^{\infty} \psi(\mathbf{r}, t) e^{j\omega t} dt \quad \in \mathbb{C}, \quad \forall \omega \in \mathbb{R}.$$

The spectral formulation allows us to neglect the initial conditions, the spectrum being computed by an integral over the entire domain of t ($t \in \mathbb{R}$). Also, with the spectral representation, the constitutive relations in isotropic media become

$$\tilde{\mathbf{D}}(\mathbf{r}, \omega) = \epsilon \tilde{\mathbf{E}}(\mathbf{r}, \omega), \quad (1.1.20)$$

$$\tilde{\mathbf{B}}(\mathbf{r}, \omega) = \mu \tilde{\mathbf{H}}(\mathbf{r}, \omega). \quad (1.1.21)$$

1.1.1 Symmetrized form of the Maxwell's equations

Before we face the problem of radiation in a bounded medium, it is interesting, for a mathematical problem solving point of view, to introduce the *symmetrized form of the Maxwell's equations*. As we can find electric charges in nature, let us suppose there exist *magnetic charges*, thus *magnetic charge densities* $\tilde{\rho}_m(\mathbf{r}, \omega)$, and the motion of these charges leads to *magnetic current densities* $\tilde{\mathbf{J}}_m(\mathbf{r}, \omega)$. The S.I. units we should give to those values are, respectively, $[V^s/m^3]$ and $[V/m^2]$, for symmetry reasons. Furthermore, as a stationary electric charge leads to a non vanishing divergence of the electric field and a moving one to a non vanishing curl of the magnetic field, a magnetic charge gives birth to a non vanishing divergence of magnetic field and a moving one to a non vanishing curl of the electric field (*Duality principle*). With these new entities, the Maxwell's equations become

$$\nabla \times \tilde{\mathbf{E}}(\mathbf{r}, \omega) = -j\omega \tilde{\mathbf{B}}(\mathbf{r}, \omega) - \tilde{\mathbf{J}}_m(\mathbf{r}, \omega), \quad (1.1.22)$$

$$\nabla \times \tilde{\mathbf{H}}(\mathbf{r}, \omega) = j\omega \tilde{\mathbf{D}}(\mathbf{r}, \omega) + \tilde{\mathbf{J}}(\mathbf{r}, \omega), \quad (1.1.23)$$

$$\nabla \cdot \tilde{\mathbf{D}}(\mathbf{r}, \omega) = \tilde{\rho}(\mathbf{r}, \omega), \quad (1.1.24)$$

$$\nabla \cdot \tilde{\mathbf{B}}(\mathbf{r}, \omega) = \tilde{\rho}_m(\mathbf{r}, \omega). \quad (1.1.25)$$

Also, there is a continuity equation for magnetic charges

$$\nabla \cdot \tilde{\mathbf{J}}_m(\mathbf{r}, \omega) + j\omega \tilde{\rho}_m(\mathbf{r}, \omega) = 0, \quad (1.1.26)$$

and the continuity of the fields at the interface between media becomes

$$\hat{\mathbf{n}} \times (\tilde{\mathbf{E}}_1(\mathbf{r}, \omega) - \tilde{\mathbf{E}}_2(\mathbf{r}, \omega)) = -\tilde{\mathbf{J}}_{ms}(\mathbf{r}, \omega), \quad (1.1.27)$$

$$\hat{\mathbf{n}} \times (\tilde{\mathbf{H}}_1(\mathbf{r}, \omega) - \tilde{\mathbf{H}}_2(\mathbf{r}, \omega)) = \tilde{\mathbf{J}}_s(\mathbf{r}, \omega), \quad (1.1.28)$$

$$\hat{\mathbf{n}} \cdot (\tilde{\mathbf{D}}_1(\mathbf{r}, \omega) - \tilde{\mathbf{D}}_2(\mathbf{r}, \omega)) = \tilde{\rho}_s(\mathbf{r}, \omega), \quad (1.1.29)$$

$$\hat{\mathbf{n}} \cdot (\tilde{\mathbf{B}}_1(\mathbf{r}, \omega) - \tilde{\mathbf{B}}_2(\mathbf{r}, \omega)) = \tilde{\rho}_{ms}(\mathbf{r}, \omega), \quad (1.1.30)$$

$\tilde{\mathbf{J}}_{ms}$ and $\tilde{\rho}_{ms}$ being, respectively, the *magnetic surface current density* in $[V/m]$ and the *magnetic surface charge density* in $[Wb/m^2]$. Despite there is no physical proof of existence of magnetic monopoles, the symmetrized form of this new set of equations

governing the electromagnetic phenomena represent, as we will see, a powerful tool for the near fields to far fields transformations. In effect, it will be possible to invoke the fields extinction outside of the domain investigated, letting the surface currents and charges keep all the necessary informations on the fields annihilated in such a way out of the domain.

1.1.2 The wave equation

The solutions $\tilde{\mathbf{E}}(\mathbf{r}, \omega)$ and $\tilde{\mathbf{H}}(\mathbf{r}, \omega)$ of the symmetrized Maxwell equations (1.1.22-1.1.25), can be computed using the *frequency-domain wave equations* for electric and magnetic fields, obtained combining the curls of equations (1.1.22) and (1.1.23) and the constitutive relations (1.1.20-1.1.21),

$$\nabla \times \nabla \times \tilde{\mathbf{E}}(\mathbf{r}, \omega) - k^2 \tilde{\mathbf{E}}(\mathbf{r}, \omega) = -\nabla \times \tilde{\mathbf{J}}_m(\mathbf{r}, \omega) - j\omega\mu \tilde{\mathbf{J}}(\mathbf{r}, \omega), \quad (1.1.31)$$

$$\nabla \times \nabla \times \tilde{\mathbf{H}}(\mathbf{r}, \omega) - k^2 \tilde{\mathbf{H}}(\mathbf{r}, \omega) = \nabla \times \tilde{\mathbf{J}}(\mathbf{r}, \omega) - j\omega\epsilon \tilde{\mathbf{J}}_m(\mathbf{r}, \omega), \quad (1.1.32)$$

where $k = \omega\sqrt{\epsilon\mu} = \omega/c = 2\pi/\lambda$, with λ the wavelength, is the *wavenumber*.

Using the equivalence [7]

$$\nabla \times \nabla \times \boldsymbol{\Omega} = \nabla(\nabla \cdot \boldsymbol{\Omega}) - \nabla^2 \boldsymbol{\Omega} \quad (1.1.33)$$

and the constitutive relations to express the equations (1.1.24 - 1.1.25) in the form

$$\nabla \cdot \tilde{\mathbf{E}}(\mathbf{r}, \omega) = \frac{1}{\epsilon} \tilde{\rho}(\mathbf{r}, \omega), \quad (1.1.34)$$

$$\nabla \cdot \tilde{\mathbf{H}}(\mathbf{r}, \omega) = \frac{1}{\mu} \tilde{\rho}_m(\mathbf{r}, \omega), \quad (1.1.35)$$

the wave equations (1.1.31-1.1.32) can be rewritten in the *Helmholtz form* as follows

$$(\nabla^2 + k^2) \tilde{\mathbf{E}}(\mathbf{r}, \omega) = j\omega\mu \tilde{\mathbf{J}}(\mathbf{r}, \omega) + \frac{1}{\epsilon} \nabla \tilde{\rho}(\mathbf{r}, \omega) + \nabla \times \tilde{\mathbf{J}}_m(\mathbf{r}, \omega), \quad (1.1.36)$$

$$(\nabla^2 + k^2) \tilde{\mathbf{H}}(\mathbf{r}, \omega) = j\omega\epsilon \tilde{\mathbf{J}}_m(\mathbf{r}, \omega) + \frac{1}{\mu} \nabla \tilde{\rho}_m(\mathbf{r}, \omega) - \nabla \times \tilde{\mathbf{J}}(\mathbf{r}, \omega). \quad (1.1.37)$$

These equations can be solved, with the previously stated boundary conditions, considering each component $\tilde{\psi}(\mathbf{r}, \omega)$ of the fields separately⁴. This leads to the solution

⁴ According to the fact that fields and currents are vector functions of the space such that and can be expressed by mean of a basis in \mathbb{R}^3 , for example by a linear combination of vectors parallel to the unit vectors of a Cartesian coordinates system.

of a set of three non-homogeneous differential equations for each field, the *scalar Helmholtz wave equations*

$$(\nabla^2 + k^2)\tilde{\psi}(\mathbf{r}, \omega) = -\tilde{S}(\mathbf{r}, \omega), \quad (1.1.38)$$

where the sources terms of the right-hand sides of (1.1.36-1.1.37) have been compacted into the scalar term $\tilde{S}(\mathbf{r}, \omega)$.

1.1.3 Scalar Huygens' principle

Let us face now the problem of radiation in a bounded medium finding a solution to the scalar wave equation (1.1.38) [7]. The figure 1.1 illustrates the geometry of the

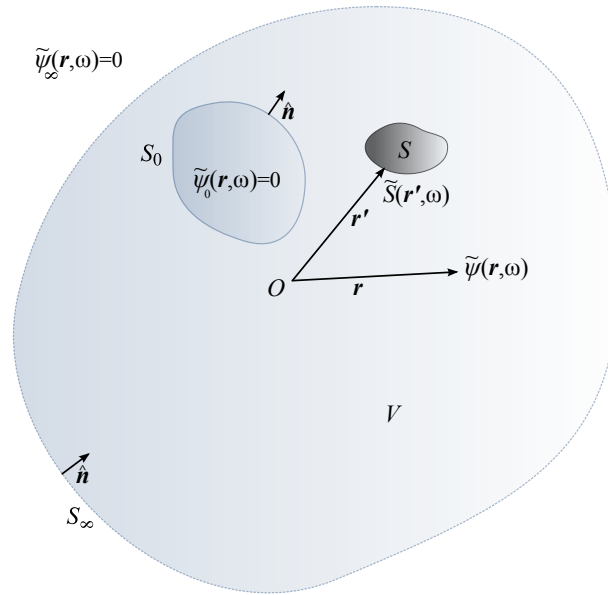


Figure 1.1: Electromagnetic radiation by arbitrary source distribution in an bounded medium.

problem: a volume V , determined by the space between the arbitrarily shaped surfaces S_0 and S_∞ , contains an arbitrarily shaped source distribution S , and the vector \mathbf{r}' points to the *infinitesimal source element* or *point source* $\tilde{S}(\mathbf{r}', \omega)$. The unit vector $\hat{\mathbf{n}}$ normal to the surfaces is chosen to be inwardly directed to V .

As previously said, the solution of this problem consists of solving the frequency domain Helmholtz wave equation (1.1.38) where $\psi(\mathbf{r}'; \omega)$ is any of the components of

the vector fields. To solve $\psi(\mathbf{r}; \omega)$ we must know the field produced by a point source, assuming that the field are given by the superposition⁵ of the field produced by each point source. This is the *Green's function* denoted $G(\mathbf{r}|\mathbf{r}'; \omega)$ and corresponds to the field produced in \mathbf{r} by a point source located in \mathbf{r}' [10]

$$(\nabla^2 + k^2)G(\mathbf{r}|\mathbf{r}'; \omega) = \delta(\mathbf{r} - \mathbf{r}'), \quad (1.1.39)$$

where δ is the Dirac delta, function of the position \mathbf{r} .

Furthermore, a solution to the Helmholtz equation (1.1.38) can be obtained using the *Green's second identity* [7] based on the following identity

$$\nabla \cdot (\Phi \nabla \Psi - \Psi \nabla \Phi) = \Phi \nabla^2 \Psi - \Psi \nabla^2 \Phi, \quad (1.1.40)$$

where Φ and Ψ are arbitrary scalar fields, then integrating over the volume V with respect to the dummy variable \mathbf{r}' and using the *divergence theorem*

$$\int_V \nabla' \cdot \boldsymbol{\Omega} dV' = - \oint_S \boldsymbol{\Omega} \cdot \hat{\mathbf{n}} dS', \quad (1.1.41)$$

where $\boldsymbol{\Omega}$ is a vector-valued function of the space⁶ and $\hat{\mathbf{n}}$ points inward to V . Assuming $\Phi = \tilde{\psi}(\mathbf{r}'; \omega)$ and $\Psi = G(\mathbf{r}|\mathbf{r}'; \omega)$, we obtain

$$\begin{aligned} \int_V [\tilde{\psi}(\mathbf{r}'; \omega) \nabla'^2 G(\mathbf{r}|\mathbf{r}'; \omega) - G(\mathbf{r}|\mathbf{r}'; \omega) \nabla'^2 \tilde{\psi}(\mathbf{r}'; \omega)] dV' = \\ - \oint_S [\tilde{\psi}(\mathbf{r}'; \omega) \nabla' G(\mathbf{r}|\mathbf{r}'; \omega) - G(\mathbf{r}|\mathbf{r}'; \omega) \nabla' \tilde{\psi}(\mathbf{r}'; \omega)] \cdot \hat{\mathbf{n}} dS'. \end{aligned} \quad (1.1.42)$$

Since $\frac{\partial}{\partial n'} = \hat{\mathbf{n}} \cdot \nabla'$, we can rewrite the right-hand side of (1.1.42) in the following manner

$$\begin{aligned} \int_V [\tilde{\psi}(\mathbf{r}'; \omega) \nabla'^2 G(\mathbf{r}|\mathbf{r}'; \omega) - G(\mathbf{r}|\mathbf{r}'; \omega) \nabla'^2 \tilde{\psi}(\mathbf{r}'; \omega)] dV' = \\ - \oint_{S_0 + S_\infty} \left[\tilde{\psi}(\mathbf{r}'; \omega) \frac{\partial G(\mathbf{r}|\mathbf{r}'; \omega)}{\partial n'} - G(\mathbf{r}|\mathbf{r}'; \omega) \frac{\partial \tilde{\psi}(\mathbf{r}'; \omega)}{\partial n'} \right] dS'. \end{aligned} \quad (1.1.43)$$

Then, applying the substitutions

$$\nabla^2 \tilde{\psi}(\mathbf{r}'; \omega) = -k^2 \tilde{\psi}(\mathbf{r}'; \omega) - \tilde{S}(\mathbf{r}', \omega)$$

⁵ According to the linearity property of Maxwell's equations, in particular of the operators $\nabla \cdot$, $\nabla \times$ and ∇ .

⁶ Notice that the gradient of a scalar function of the space is a vector function.

and

$$\nabla^2 G(\mathbf{r}|\mathbf{r}'; \omega) = -k^2 G(\mathbf{r}|\mathbf{r}'; \omega) - \delta(\mathbf{r} - \mathbf{r}')$$

derived from (1.1.38-1.1.39) in the left-hand side of equation (1.1.43), we obtain

$$\begin{aligned} & \int_V \left[\tilde{\psi}(\mathbf{r}'; \omega) \left(-k^2 G(\mathbf{r}|\mathbf{r}'; \omega) - \delta(\mathbf{r} - \mathbf{r}') \right) - \right. \\ & \quad \left. G(\mathbf{r}|\mathbf{r}'; \omega) \left(-k^2 \tilde{\psi}(\mathbf{r}'; \omega) - \tilde{S}(\mathbf{r}'; \omega) \right) \right] dV' = \\ & \quad - \oint_{S_0+S_\infty} \left[\tilde{\psi}(\mathbf{r}'; \omega) \frac{\partial G(\mathbf{r}|\mathbf{r}'; \omega)}{\partial n'} - G(\mathbf{r}|\mathbf{r}'; \omega) \frac{\partial \tilde{\psi}(\mathbf{r}'; \omega)}{\partial n'} \right] dS'. \end{aligned} \quad (1.1.44)$$

Being equivalent, the terms with the wavenumber k vanish, and the sifting property of the Dirac delta gives the following equation

$$\begin{aligned} \tilde{\psi}(\mathbf{r}; \omega) &= \int_V G(\mathbf{r}|\mathbf{r}'; \omega) \tilde{S}(\mathbf{r}'; \omega) dV' + \\ & \quad \oint_{S_0+S_\infty} \left[\tilde{\psi}(\mathbf{r}'; \omega) \frac{\partial G(\mathbf{r}|\mathbf{r}'; \omega)}{\partial n'} - G(\mathbf{r}|\mathbf{r}'; \omega) \frac{\partial \tilde{\psi}(\mathbf{r}'; \omega)}{\partial n'} \right] dS', \end{aligned} \quad (1.1.45)$$

if \mathbf{r} is chosen to lie within V , otherwise $\tilde{\psi}(\mathbf{r}; \omega) = 0^7$.

The integral over S_∞ vanishes when $\mathbf{r}' \rightarrow \infty$, as the field $\tilde{\psi}(\mathbf{r}; \omega)$ and its derivative go to zero for the *Sommerfeld's radiation conditions*⁸ expressed by the following limits

$$\lim_{r \rightarrow \infty} \tilde{\psi}(\mathbf{r}; \omega) = 0, \quad (1.1.46)$$

$$\lim_{r \rightarrow \infty} \left[j k \tilde{\psi}(\mathbf{r}; \omega) + \frac{\partial}{\partial r} \tilde{\psi}(\mathbf{r}; \omega) \right] = 0. \quad (1.1.47)$$

Removing the integral over S_∞ means that we are removing the outer bounding surface of V , letting the radiation externally unbounded. This is necessary in order to compute the radiation pattern, which considers fields infinitely far away from the sources. Hence, the equation (1.1.45) becomes

$$\begin{aligned} \tilde{\psi}(\mathbf{r}; \omega) &= \int_V G(\mathbf{r}|\mathbf{r}'; \omega) \tilde{S}(\mathbf{r}'; \omega) dV' + \\ & \quad \oint_{S_0} \left[\tilde{\psi}(\mathbf{r}'; \omega) \frac{\partial G(\mathbf{r}|\mathbf{r}'; \omega)}{\partial n'} - G(\mathbf{r}|\mathbf{r}'; \omega) \frac{\partial \tilde{\psi}(\mathbf{r}'; \omega)}{\partial n'} \right] dS'. \end{aligned} \quad (1.1.48)$$

⁷ The sifting property of Dirac delta is such that, for fields evaluated out of the integration domain, the integral becomes null as $\int_V f(\mathbf{r}') \delta(\mathbf{r} - \mathbf{r}') dV' = 0$, $\forall \mathbf{r} \notin V$, $f(\mathbf{r})$ being a generic function of the space.

⁸ These limits actually express the physically observable attenuation of the electromagnetic fields as we get away from the sources.

The equation (1.1.48) states that the field $\tilde{\psi}(\mathbf{r}; \omega)$ within V ($V \equiv \mathbb{R}^3 / \{V_{S_0}\}$), can be determined once one knows the source distribution S within V and the field and its normal derivative on S_0 .

The problem of near field to far field transformation can be split into two parts. The first concerns in the determination of the near field over an arbitrary surface S_C encompassing the whole sources distribution, that is computing the first integral of (1.1.48) to obtain the field and its normal derivative on S_C , such that the sources can be excluded from V in the second part. The second part uses the near field and derivative previously obtained to calculate the field in V . This is the scalar Huygen's principle, stated in the second integral of (1.1.48), which says that all the necessary informations about the sources enclosed is kept in the fields they produce on the enclosing surface. The near-to-far transformation with scalar field will be discussed in section 1.2. We first proceed with the extension of the radiation in a bounded medium to vector fields.

1.1.4 Vector Huygens' principle

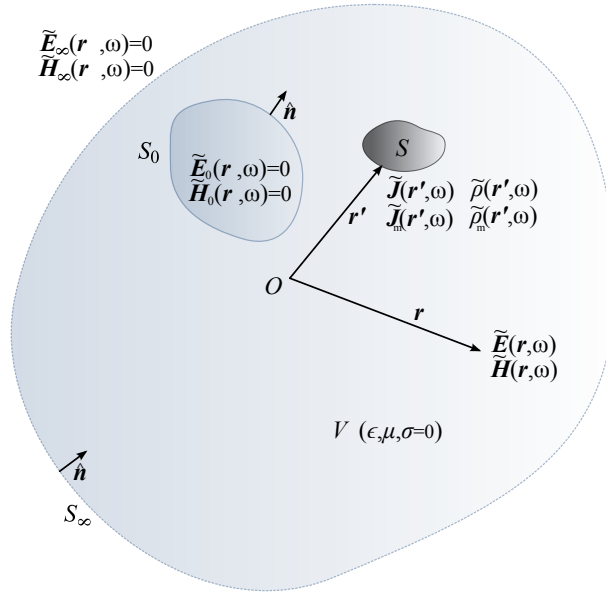


Figure 1.2: Electromagnetic radiation by arbitrary currents and charges distribution in a bounded medium.

Proceeding in the same manner as for the scalar Huygens' principle, we now use the *Green's second identity* (1.1.40) extended to vector fields to compute the electric field in the bounded medium depicted in figure 1.2. We obtain

$$\begin{aligned} & \int_V \left[\tilde{\mathbf{E}}(\mathbf{r}'; \omega) \nabla'^2 G(\mathbf{r}|\mathbf{r}'; \omega) - G(\mathbf{r}|\mathbf{r}'; \omega) \nabla'^2 \tilde{\mathbf{E}}(\mathbf{r}'; \omega) \right] dV' = \\ & - \oint_{S_0 + S_\infty} \left[\tilde{\mathbf{E}}(\mathbf{r}'; \omega) (\hat{\mathbf{n}} \cdot \nabla' G(\mathbf{r}|\mathbf{r}'; \omega)) - G(\mathbf{r}|\mathbf{r}'; \omega) (\hat{\mathbf{n}} \cdot \nabla' \tilde{\mathbf{E}}(\mathbf{r}'; \omega)) \right] dS', \end{aligned} \quad (1.1.49)$$

where $\hat{\mathbf{n}}$ is inwardly directed to V . We now apply to the left-hand side integrand of (1.1.49) the substitutions

$$\nabla^2 \tilde{\mathbf{E}}(\mathbf{r}, \omega) = -k^2 \tilde{\mathbf{E}}(\mathbf{r}, \omega) + j\omega\mu \tilde{\mathbf{J}}(\mathbf{r}, \omega) + \frac{1}{\epsilon} \nabla \tilde{\rho}(\mathbf{r}, \omega) + \nabla \times \tilde{\mathbf{J}}_m(\mathbf{r}, \omega)$$

and

$$\nabla^2 G(\mathbf{r}|\mathbf{r}'; \omega) = -k^2 G(\mathbf{r}|\mathbf{r}'; \omega) - \delta(\mathbf{r} - \mathbf{r}')$$

respectively derived from (1.1.36) and (1.1.39) to obtain the equation

$$\begin{aligned} & \int_V \left[-\tilde{\mathbf{E}} \delta(\mathbf{r} - \mathbf{r}') - G \left(j\omega\mu \tilde{\mathbf{J}} + \frac{1}{\epsilon} \nabla' \tilde{\rho} + \nabla' \times \tilde{\mathbf{J}}_m \right) \right] dV' = \\ & - \oint_{S_0 + S_\infty} \left[\tilde{\mathbf{E}} (\hat{\mathbf{n}} \cdot \nabla' G) - G (\hat{\mathbf{n}} \cdot \nabla' \tilde{\mathbf{E}}) \right] dS', \end{aligned} \quad (1.1.50)$$

where, for compactness in notation, we have made the substitutions $\tilde{\mathbf{E}} = \tilde{\mathbf{E}}(\mathbf{r}'; \omega)$, $G = G(\mathbf{r}|\mathbf{r}'; \omega)$, $\tilde{\mathbf{J}} = \tilde{\mathbf{J}}(\mathbf{r}', \omega)$, $\tilde{\rho} = \tilde{\rho}(\mathbf{r}', \omega)$ and $\tilde{\mathbf{J}}_m = \tilde{\mathbf{J}}_m(\mathbf{r}', \omega)$. Once again, the terms with the wavenumber k have cancelled each other. The sifting property of the Dirac delta allows the calculation of the field $\tilde{\mathbf{E}}(\mathbf{r}; \omega)$ in an arbitrary point of V (elsewhere null, see note 7), and (1.1.50) becomes

$$\begin{aligned} \tilde{\mathbf{E}}(\mathbf{r}; \omega) = & - \int_V \left[G \left(j\omega\mu \tilde{\mathbf{J}} + \frac{1}{\epsilon} \nabla' \tilde{\rho} + \nabla' \times \tilde{\mathbf{J}}_m \right) \right] dV' + \\ & \oint_{S_0 + S_\infty} \left[\tilde{\mathbf{E}} (\hat{\mathbf{n}} \cdot \nabla' G) - G (\hat{\mathbf{n}} \cdot \nabla' \tilde{\mathbf{E}}) \right] dS'. \end{aligned} \quad (1.1.51)$$

Using the integral theorems (respectively *gradient theorem* and *curl theorem*) [7]

$$\int_V \nabla' \Psi dV' = - \oint_S \Psi \cdot \hat{\mathbf{n}} dS', \quad (1.1.52)$$

$$\int_V \nabla' \times \boldsymbol{\Omega} dV' = - \oint_S \hat{\mathbf{n}} \times \boldsymbol{\Omega} dS', \quad (1.1.53)$$

with $\hat{\mathbf{n}}$ pointing inward to V , one can rewrite the first integral term of right-hand side of (1.1.51) as

$$\begin{aligned} & - \int_V \left[j\omega\mu G \tilde{\mathbf{J}} + \frac{1}{\epsilon} G \nabla' \tilde{\rho} + G \nabla' \times \tilde{\mathbf{J}}_m \right] dV' = \\ & - \int_V \left[j\omega\mu G \tilde{\mathbf{J}} - \frac{1}{\epsilon} \tilde{\rho} \nabla' G + \tilde{\mathbf{J}}_m \times \nabla' G \right] dV' + \\ & \oint_{S_0+S_\infty} \left[\hat{\mathbf{n}} \frac{1}{\epsilon} \tilde{\rho} G + \hat{\mathbf{n}} \times \tilde{\mathbf{J}}_m G \right] dS', \end{aligned} \quad (1.1.54)$$

where the vector identities [8]

$$\nabla(\Psi\Phi) = \Psi\nabla\Phi + \Phi\nabla\Psi, \quad (1.1.55)$$

$$\nabla \times (\Psi\mathbf{\Omega}) = \Psi\nabla \times \mathbf{\Omega} + \nabla\Phi \times \mathbf{\Omega}, \quad (1.1.56)$$

have been employed with $\Psi = G$, $\Phi = \tilde{\rho}$ and $\mathbf{\Omega} = \tilde{\mathbf{J}}_m$. Then, using the following vector identity [8]

$$\begin{aligned} \Psi(\hat{\mathbf{n}} \cdot \nabla \mathbf{\Omega}) - \mathbf{\Omega}(\hat{\mathbf{n}} \cdot \nabla \Psi) &= [\hat{\mathbf{n}} \cdot \nabla(\Psi\mathbf{\Omega}) + \hat{\mathbf{n}} \times (\nabla \times (\Psi\mathbf{\Omega})) - \hat{\mathbf{n}} \nabla \cdot (\Psi\mathbf{\Omega})] + \\ & [\hat{\mathbf{n}} \Psi \nabla \cdot \mathbf{\Omega} - (\hat{\mathbf{n}} \times \mathbf{\Omega}) \times \nabla \Psi - \Psi \hat{\mathbf{n}} \times (\nabla \times \mathbf{\Omega}) - (\hat{\mathbf{n}} \cdot \mathbf{\Omega}) \nabla \Psi], \end{aligned} \quad (1.1.57)$$

and assuming $\Psi = G$ and $\mathbf{\Omega} = \tilde{\mathbf{E}}$, the second integrand term in the right-hand side of (1.1.51) can be expressed as

$$\begin{aligned} & \oint_{S_0+S_\infty} [\tilde{\mathbf{E}}(\hat{\mathbf{n}} \cdot \nabla' G) - G(\hat{\mathbf{n}} \cdot \nabla' \tilde{\mathbf{E}})] dS' = \\ & - \oint_{S_0+S_\infty} [\hat{\mathbf{n}} \cdot \nabla' (G\tilde{\mathbf{E}}) + \hat{\mathbf{n}} \times (\nabla' \times (G\tilde{\mathbf{E}})) \hat{\mathbf{n}} \nabla' \cdot (G\tilde{\mathbf{E}})] dS' + \\ & - \oint_{S_0+S_\infty} [\hat{\mathbf{n}} G \nabla' \cdot \tilde{\mathbf{E}} - (\hat{\mathbf{n}} \times \tilde{\mathbf{E}}) \times \nabla' G - G \hat{\mathbf{n}} \times (\nabla' \times \tilde{\mathbf{E}}) - (\hat{\mathbf{n}} \cdot \tilde{\mathbf{E}}) \nabla' G] dS' \end{aligned} \quad (1.1.58)$$

The integral theorem [8]

$$\begin{aligned} & \oint_S (\hat{\mathbf{n}} \times \nabla') \times (\Psi\mathbf{\Omega}) dS = 0 = \\ & \oint_S [\hat{\mathbf{n}} \times (\nabla' \times (\Psi\mathbf{\Omega})) + (\hat{\mathbf{n}} \cdot \nabla') (\Psi\mathbf{\Omega}) - \hat{\mathbf{n}} (\nabla' \cdot (\Psi\mathbf{\Omega}))] dS \end{aligned} \quad (1.1.59)$$

allows us to neglect the first integral term in right-hand side of (1.1.58), and (1.1.51) can be expressed as

$$\tilde{\mathbf{E}}(\mathbf{r}; \omega) = - \int_V \left[j\omega\mu G \tilde{\mathbf{J}} - \frac{1}{\epsilon} \tilde{\rho} \nabla' G + \tilde{\mathbf{J}}_m \times \nabla' G \right] dV' +$$

$$\oint_{S_0+S_\infty} \left[\hat{\mathbf{n}} \frac{1}{\epsilon} \tilde{\rho} G + \hat{\mathbf{n}} \times \tilde{\mathbf{J}}_m G \right] dS' - \oint_{S_0+S_\infty} \left[\hat{\mathbf{n}} G \nabla' \cdot \tilde{\mathbf{E}} - (\hat{\mathbf{n}} \times \tilde{\mathbf{E}}) \times \nabla' G - G \hat{\mathbf{n}} \times (\nabla' \times \tilde{\mathbf{E}}) - (\hat{\mathbf{n}} \cdot \tilde{\mathbf{E}}) \nabla' G \right] dS' \quad (1.1.60)$$

The divergence and curl of the electric field terms in the integrand of the third surface integral of right-hand side of (1.1.60) can be substituted, respectively, using the Poisson's equation (1.1.34) and the symmetrized Faraday's law (1.1.22) together with the constitutive equation of the magnetic field (1.1.21). As a result, the second integral of right-hand side of (1.1.60) vanishes and we obtain

$$\tilde{\mathbf{E}}(\mathbf{r}; \omega) = \int_V \left[-j\omega\mu G \tilde{\mathbf{J}} + \frac{1}{\epsilon} \tilde{\rho} \nabla' G - \tilde{\mathbf{J}}_m \nabla' \times G \right] dV' + \oint_{S_0+S_\infty} \left[-j\omega\mu G (\hat{\mathbf{n}} \times \tilde{\mathbf{H}}) + (\hat{\mathbf{n}} \cdot \tilde{\mathbf{E}}) \nabla' G + (\hat{\mathbf{n}} \times \tilde{\mathbf{E}}) \times \nabla' G \right] dS', \quad (1.1.61)$$

where $\tilde{\mathbf{H}} = \tilde{\mathbf{H}}(\mathbf{r}'; \omega)$. Then, considering the medium externally unbounded, that is letting the bounding surface S_∞ going far away from the sources positions and applying the *Sommerfeld's radiation conditions* for vector fields [7]

$$\lim_{r \rightarrow \infty} r \tilde{\mathbf{E}}(\mathbf{r}; \omega) < \infty, \quad (1.1.62)$$

$$\lim_{r \rightarrow \infty} r \left[\zeta \hat{\mathbf{r}} \times \tilde{\mathbf{H}}(\mathbf{r}; \omega) + \tilde{\mathbf{E}}(\mathbf{r}; \omega) \right] = 0, \quad (1.1.63)$$

with $\zeta = \sqrt{\frac{\mu}{\epsilon}} = \zeta_0 \sqrt{\frac{\mu_r}{\epsilon_r}}$, $\zeta_0 \approx 376.73[\Omega]$ the *plane wave impedance*, we obtain the following equation for the electric field

$$\tilde{\mathbf{E}}(\mathbf{r}; \omega) = \int_V \left[-j\omega\mu G \tilde{\mathbf{J}} + \frac{1}{\epsilon} \tilde{\rho} \nabla' G - \tilde{\mathbf{J}}_m \nabla' \times G \right] dV' + \oint_{S_0} \left[-j\omega\mu G (\hat{\mathbf{n}} \times \tilde{\mathbf{H}}) + (\hat{\mathbf{n}} \cdot \tilde{\mathbf{E}}) \nabla' G + (\hat{\mathbf{n}} \times \tilde{\mathbf{E}}) \times \nabla' G \right] dS'. \quad (1.1.64)$$

Proceeding analogously, we derive an equation for the magnetic field

$$\tilde{\mathbf{H}}(\mathbf{r}; \omega) = \int_V \left[-j\omega\epsilon G \tilde{\mathbf{J}}_m + \frac{1}{\mu} \tilde{\rho}_m \nabla' G - \tilde{\mathbf{J}} \nabla' \times G \right] dV' + \oint_{S_0} \left[j\omega\epsilon G (\hat{\mathbf{n}} \times \tilde{\mathbf{E}}) + (\hat{\mathbf{n}} \cdot \tilde{\mathbf{H}}) \nabla' G + (\hat{\mathbf{n}} \times \tilde{\mathbf{H}}) \times \nabla' G \right] dS', \quad (1.1.65)$$

with the additional equivalence $\tilde{\rho}_m = \tilde{\rho}_m(\mathbf{r}', \omega)$. The radiation conditions corresponding to (1.1.65) are

$$\lim_{r \rightarrow \infty} r \tilde{\mathbf{H}}(\mathbf{r}; \omega) < \infty, \quad (1.1.66)$$

$$\lim_{r \rightarrow \infty} r [\zeta \tilde{\mathbf{H}}(\mathbf{r}; \omega) - \hat{\mathbf{r}} \times \tilde{\mathbf{E}}(\mathbf{r}; \omega)] = 0. \quad (1.1.67)$$

Equations (1.1.64) and (1.1.65) are the so-called *Stratton-Chu formulas* [9] which, similarly to (1.1.48) for the scalar field, have two integrals: the first one dealing with the direct computation of the fields from sources distributions, the second one to formulate the vector Huygen's principle.

It is to be noted that, for the fields extinction out of V and for the continuity equations of the fields (1.1.28-1.1.30)⁹, the terms $\hat{\mathbf{n}} \times \tilde{\mathbf{E}}(\mathbf{r}'; \omega)$, $\hat{\mathbf{n}} \times \tilde{\mathbf{H}}(\mathbf{r}'; \omega)$, $\hat{\mathbf{n}} \cdot \tilde{\mathbf{E}}(\mathbf{r}'; \omega)$ and $\hat{\mathbf{n}} \cdot \tilde{\mathbf{H}}(\mathbf{r}'; \omega)$ in the second integrands of (1.1.64) and (1.1.65) correspond to, respectively, the surface currents $-\tilde{\mathbf{J}}_{ms}(\mathbf{r}, \omega)$ and $\tilde{\mathbf{J}}_s(\mathbf{r}, \omega)$, and surface charges related terms $1/\epsilon \tilde{\rho}_s(\mathbf{r}, \omega)$ and $1/\mu \tilde{\rho}_{ms}(\mathbf{r}, \omega)$, all of them located on S_0 . These surface sources are also named *equivalent sources* as they take place to represent the equivalent unbounded electromagnetic problem.

For a practical use of the Stratton-Chu formulas (1.1.64-1.1.65), it is interesting to convert them into a form that does not contain charge densities sources and equivalent surface charge densities. This is achieved with the use of the continuity equations for the charges (1.1.19) and (1.1.26). We begin for the electric field, recasting the second integrand term of the first integral of (1.1.64) in the following manner:

$$\begin{aligned} \int_V \frac{1}{\epsilon} \tilde{\rho} \nabla' G \, dV' &= -\frac{1}{j\omega\epsilon} \int_V (\nabla' \cdot \tilde{\mathbf{J}}) \nabla' G \, dV' \\ &= -\frac{1}{j\omega\epsilon} \left[\int_V \nabla' \cdot (\tilde{\mathbf{J}} \nabla' G) \, dV' - \int_V (\tilde{\mathbf{J}} \cdot \nabla') \nabla' G \, dV' \right], \end{aligned} \quad (1.1.68)$$

where the vector identity [7]

$$\nabla \cdot (\boldsymbol{\Omega} \Psi) = (\nabla \cdot \boldsymbol{\Omega}) \Psi + \boldsymbol{\Omega} \cdot (\nabla \Psi) = (\nabla \cdot \boldsymbol{\Omega}) \Psi + (\boldsymbol{\Omega} \cdot \nabla) \Psi \quad (1.1.69)$$

have been employed with $\Psi = \nabla G$ and $\boldsymbol{\Omega} = \tilde{\mathbf{J}}$. The first integral in right-hand side of (1.1.68), for the divergence theorem (1.1.41), becomes

$$-\frac{1}{j\omega\epsilon} \int_V \nabla' \cdot (\tilde{\mathbf{J}} \nabla' G) \, dV' = \frac{1}{j\omega\epsilon} \oint_S (\tilde{\mathbf{J}} \nabla' G) \cdot \hat{\mathbf{n}} \, dS', \quad (1.1.70)$$

⁹ $\tilde{\mathbf{E}}_2(\mathbf{r}'; \omega) = \tilde{\mathbf{H}}_2(\mathbf{r}'; \omega) = 0$, $\tilde{\mathbf{E}}(\mathbf{r}'; \omega) = \tilde{\mathbf{H}}_1(\mathbf{r}'; \omega)$, $\tilde{\mathbf{H}}(\mathbf{r}'; \omega) = \tilde{\mathbf{E}}_1(\mathbf{r}'; \omega)$ and $\hat{\mathbf{n}}$ inwardly directed to V (region 1).

which vanishes if the volume V surrounded by S is chosen such that it slightly exceed that needed to contain the impressed sources. We obtain

$$\int_V \frac{1}{\epsilon} \tilde{\rho} \nabla' G dV' = \frac{1}{j\omega\epsilon} \int_V (\tilde{\mathbf{J}} \cdot \nabla') \nabla' G dV'. \quad (1.1.71)$$

Assuming now the charge and current densities of (1.1.71) to be located on the surface S_0 (to be of surface kind) and using the continuity equations (1.1.28-1.1.30), we can write

$$\begin{aligned} \int_V [j\omega\tilde{\rho}_s - (\tilde{\mathbf{J}}_s \cdot \nabla')] \nabla' G dV' &= 0 = \\ \oint_{S_0} [j\omega\epsilon (\hat{\mathbf{n}} \cdot \tilde{\mathbf{E}}) - ((\hat{\mathbf{n}} \times \tilde{\mathbf{H}}) \cdot \nabla')] \nabla' G dS'. \end{aligned} \quad (1.1.72)$$

Thus, the Stratton-Chu equation for the electric field (1.1.64) can be rewritten into the following *Kottler's form* [8]

$$\begin{aligned} \tilde{\mathbf{E}}(\mathbf{r}; \omega) &= \frac{1}{j\omega\epsilon} \int_V [k^2 G \tilde{\mathbf{J}} + (\tilde{\mathbf{J}} \cdot \nabla') \nabla' G - j\omega\epsilon \tilde{\mathbf{J}}_m \times \nabla' G] dV' + \\ \frac{1}{j\omega\epsilon} \oint_{S_0} [k^2 G (\hat{\mathbf{n}} \times \tilde{\mathbf{H}}) + ((\hat{\mathbf{n}} \times \tilde{\mathbf{H}}) \cdot \nabla') \nabla' G + j\omega\epsilon (\hat{\mathbf{n}} \times \tilde{\mathbf{E}}) \times \nabla' G] dS'. \end{aligned} \quad (1.1.73)$$

Analogously for the magnetic field, (1.1.65) becomes

$$\begin{aligned} \tilde{\mathbf{H}}(\mathbf{r}; \omega) &= \frac{1}{j\omega\mu} \int_V [k^2 G \tilde{\mathbf{J}}_m + (\tilde{\mathbf{J}}_m \cdot \nabla') \nabla' G + j\omega\mu \tilde{\mathbf{J}} \times \nabla' G] dV' + \\ \frac{1}{j\omega\mu} \oint_{S_0} [-k^2 G (\hat{\mathbf{n}} \times \tilde{\mathbf{E}}) - ((\hat{\mathbf{n}} \times \tilde{\mathbf{E}}) \cdot \nabla') \nabla' G + j\omega\mu (\hat{\mathbf{n}} \times \tilde{\mathbf{H}}) \times \nabla' G] dS'. \end{aligned} \quad (1.1.74)$$

The surface integrals of Kottler's equations (1.1.73-1.1.74) state the so-called *Love's equivalence principle* [7] while considering the *equivalent electric and magnetic currents* $\tilde{\mathbf{J}}_s^{eq} = \hat{\mathbf{n}} \times \tilde{\mathbf{H}}$ and $\tilde{\mathbf{J}}_{ms}^{eq} = -\hat{\mathbf{n}} \times \tilde{\mathbf{E}}$ on the bounding surface S_0 .

1.2 Scalar near field to far field transformation

In this section, we present a numerical implementation of the scalar near field to far field transformation (scalar N2F), relying on the mathematical formulation discussed in section 1.1.3. We first recall in a generic form the steps to be followed for

the scalar N2F, then a computation will be performed in Matlab¹⁰ environment considering as enclosing surface first a sphere then a parallelepiped. The results will be compared to the direct computation of the far fields, assuming an unbounded medium.

1.2.1 Computation steps

For the computation of the near field or *Fresnel-zone* field, we need to consider the sources distributed within the volume $V_S \subset V$, determined by the arbitrary surface S_C , chosen to be relatively close¹¹ to the sources. We also consider the surface S_0 going to zero, such that the second integral term in the right-hand side of equation (1.1.48) vanishes. We obtain:

$$\tilde{\psi}(\mathbf{r}; \omega) \Big|_{S_C} = \int_{V_S} G(\mathbf{r}|\mathbf{r}'; \omega) \tilde{S}(\mathbf{r}', \omega) dV' \quad (1.2.75)$$

where \mathbf{r}' is a vector pointing to an infinitesimal source element. The problem's geometry is depicted in figure 1.3. The Green's function that will be used is the well-known *Green's function for free space*

$$G(\mathbf{r}|\mathbf{r}'; \omega) = \frac{e^{-jk|\mathbf{r}-\mathbf{r}'|}}{4\pi|\mathbf{r}-\mathbf{r}'|} \quad (1.2.76)$$

and the sources will be assumed to be radiating isotropically such that the whole radiating structure emits a unit of power, that is $\sum_{n=1}^N |\tilde{S}_n(\mathbf{r}', \omega)|^2 = 1$, with N the number of sources.

The computation of the far field or *Fraunhofer-zone* field can be performed by simply setting the modulus of the vectors \mathbf{r} of a consistent number of wavelengths (see note 11). This is the direct computation of the far field from an arbitrary sources distribution. However, we are interested in the computation of the far field not directly from the sources but from the near field they produce. Looking at the equation

¹⁰ Matlab[®] Mathworks. Further informations available on www.mathworks.com.

¹¹ The distance $\frac{2L^2}{\lambda}$, where L is the highest length in a planar distribution of point sources and λ the wavelength, is the distance from the sources where we commit a maximum phase error of $\pi/8$ in the plane wave approximation directed perpendicularly to the point sources distribution. This distance can be taken as a reference for the near-zone to far-zone fields transition and the near fields are typically considered to lie within $d \ll \frac{2L^2}{\lambda}$.

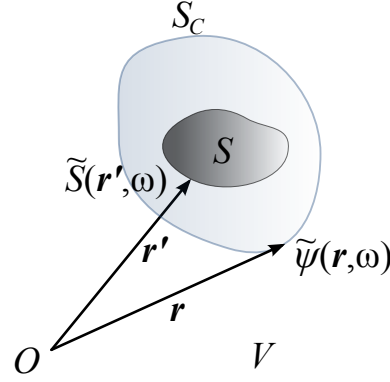


Figure 1.3: Near fields computations.

(1.1.48), we see that we can achieve this by letting S_0 be wide enough to encompass all the sources, such that they are not anymore part of V and the first integral term in the right-hand side of (1.1.48) goes to zero. Then, from the field $\tilde{\psi}(\mathbf{r}'; \omega)$ computed over S_0 , we compute the second integral term to obtain the field $\tilde{\psi}(\mathbf{r}; \omega) \forall \mathbf{r} \in V$. To make sure that the field previously calculated with (1.2.75) equals $\tilde{\psi}(\mathbf{r}'; \omega)$, we choose S_0 equal to S_C . Now, the expression to evaluate is

$$\tilde{\psi}(\mathbf{r}; \omega) = \oint_{S_0=S_C} \left[\tilde{\psi}(\mathbf{r}'; \omega) \frac{\partial G(\mathbf{r}|\mathbf{r}'; \omega)}{\partial n'} - G(\mathbf{r}|\mathbf{r}'; \omega) \frac{\partial \tilde{\psi}(\mathbf{r}'; \omega)}{\partial n'} \right] dS'. \quad (1.2.77)$$

The scalar N2F step is depicted in figure 1.4.

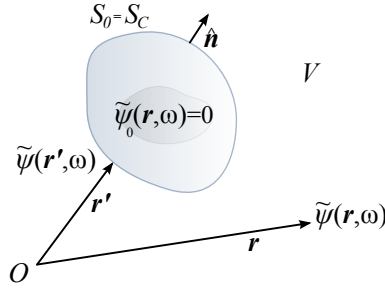


Figure 1.4: Near-to-far fields transformations.

1.2.2 Computations on a bounding sphere

Let us now assume the bounding surface $S_0 = S_C$ to be a sphere, and the origin of the reference system O to be located at the center of the sphere. The geometry of the

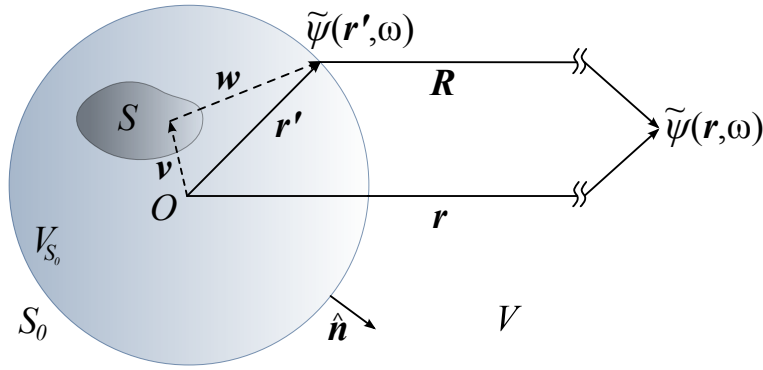


Figure 1.5: Near-to-far fields transformations from a bounding sphere.

problem is depicted in figure 1.5. The volume V is the entire free space, excluded V_{S_0} which contains all the sources. The spherical geometry of the problem allows us to use spherical coordinates computing the previous relations (1.2.75) and (1.2.77).

The near field is computed using the (1.2.75) for the given geometry and we have

$$\tilde{\psi}(\mathbf{r}'; \omega) \Big|_{S_0} = \int_{V_{S_0}} \frac{e^{-jk|\mathbf{r}'-\mathbf{v}|}}{4\pi|\mathbf{r}'-\mathbf{v}|} \tilde{S}(\mathbf{v}, \omega) dV_v. \quad (1.2.78)$$

(1.2.78) gives the value of the near field surface density on a single infinitesimal point of the sphere indicated by \mathbf{r}' (i.e. determined by the Green's function) and produced by the enclosed sources distribution.

We now proceed with the scalar N2F, provided that $\tilde{\psi}(\mathbf{r}'; \omega)$ and its gradient $\nabla' \tilde{\psi}(\mathbf{r}'; \omega)$ are known on the entire sphere.

Using $\frac{e^{-jk|\mathbf{R}|}}{4\pi|\mathbf{R}|} = \frac{e^{-jk|\mathbf{r}-\mathbf{r}'|}}{4\pi|\mathbf{r}-\mathbf{r}'|}$ as Green's function, the far field becomes the following

$$\tilde{\psi}(\mathbf{r}; \omega) = \oint_{S_0} \left[\tilde{\psi}(\mathbf{r}'; \omega) \frac{\partial}{\partial n'} \frac{e^{-jk|\mathbf{R}|}}{4\pi|\mathbf{R}|} - \frac{e^{-jk|\mathbf{R}|}}{4\pi|\mathbf{R}|} \frac{\partial \tilde{\psi}(\mathbf{r}'; \omega)}{\partial n'} \right] dS'. \quad (1.2.79)$$

The gradient of the Green's function is

$$\nabla_{\mathbf{R}} \frac{e^{-jk|\mathbf{R}|}}{4\pi|\mathbf{R}|} = - \left(jk + \frac{1}{|\mathbf{R}|} \right) \frac{e^{-jk|\mathbf{R}|}}{4\pi|\mathbf{R}|} \frac{\mathbf{R}}{|\mathbf{R}|} \quad (1.2.80)$$

and its normal derivative

$$\begin{aligned} \frac{\partial}{\partial n'} \frac{e^{-jk|\mathbf{R}|}}{4\pi|\mathbf{R}|} &= \hat{\mathbf{n}} \cdot \nabla' \frac{e^{-jk|\mathbf{r}-\mathbf{r}'|}}{4\pi|\mathbf{r}-\mathbf{r}'|} = -\hat{\mathbf{n}} \cdot \nabla \frac{e^{-jk|\mathbf{r}-\mathbf{r}'|}}{4\pi|\mathbf{r}-\mathbf{r}'|} = -\hat{\mathbf{n}} \cdot \nabla_{\mathbf{R}} \frac{e^{-jk|\mathbf{R}|}}{4\pi|\mathbf{R}|} \\ &= \left(jk + \frac{1}{|\mathbf{R}|} \right) \frac{e^{-jk|\mathbf{R}|}}{4\pi|\mathbf{R}|} \left(\frac{\mathbf{R}}{|\mathbf{R}|} \cdot \hat{\mathbf{n}} \right). \end{aligned} \quad (1.2.81)$$

For the spherical shape of the surface S_0 , its normal inwardly directed to V is $\hat{\mathbf{n}} = \frac{\mathbf{r}'}{|\mathbf{r}'|}$ and the integral relation (1.2.79) can be rewritten as follows

$$\begin{aligned}
 \tilde{\psi}(\mathbf{r}; \omega) &= \oint_{S_0} \left[\tilde{\psi}(\mathbf{r}'; \omega) \left(jk + \frac{1}{|\mathbf{R}|} \right) \frac{e^{-jk|\mathbf{R}|}}{4\pi|\mathbf{R}|} \left(\frac{\mathbf{R}}{|\mathbf{R}|} \cdot \frac{\mathbf{r}'}{|\mathbf{r}'|} \right) - \frac{e^{-jk|\mathbf{R}|}}{4\pi|\mathbf{R}|} \frac{\partial \tilde{\psi}(\mathbf{r}'; \omega)}{\partial n'} \right] dS' \\
 &= \oint_{S_0} \frac{e^{-jk|\mathbf{R}|}}{4\pi|\mathbf{R}|} \left[\left(jk + \frac{1}{|\mathbf{R}|} \right) \tilde{\psi}(\mathbf{r}'; \omega) \left(\frac{\mathbf{R}}{|\mathbf{R}|} \cdot \frac{\mathbf{r}'}{|\mathbf{r}'|} \right) - \frac{\partial \tilde{\psi}(\mathbf{r}'; \omega)}{\partial n'} \right] dS' \\
 &= \oint_{S_0} \frac{e^{-jk|\mathbf{R}|}}{4\pi|\mathbf{R}|} \left[\left(jk + \frac{1}{|\mathbf{R}|} \right) \tilde{\psi}(\mathbf{r}'; \omega) \left(\frac{\mathbf{R}}{|\mathbf{R}|} \cdot \frac{\mathbf{r}'}{|\mathbf{r}'|} \right) - \right. \\
 &\quad \left. \frac{\partial \tilde{\psi}(\mathbf{r}'; \omega)}{\partial r'} \left(\frac{\mathbf{r}'}{|\mathbf{r}'|} \cdot \frac{\mathbf{r}'}{|\mathbf{r}'|} \right) \right] dS' \\
 &= \oint_{S_0} \frac{e^{-jk|\mathbf{R}|}}{4\pi|\mathbf{R}|} \left[\left(jk + \frac{1}{|\mathbf{R}|} \right) \tilde{\psi}(\mathbf{r}'; \omega) \left(\frac{\mathbf{R}}{|\mathbf{R}|} \cdot \frac{\mathbf{r}'}{|\mathbf{r}'|} \right) - \frac{\partial \tilde{\psi}(\mathbf{r}'; \omega)}{\partial r'} \right] dS'. \quad (1.2.82)
 \end{aligned}$$

where we have used the identity $\frac{\partial}{\partial n'} = \left(\frac{\mathbf{r}'}{|\mathbf{r}'|} \cdot \hat{\mathbf{n}} \right) \frac{\partial}{\partial r'}$.

As we are only interested in the far field, we can make the following approximations for $|\mathbf{R}|$ noting that

$$R = \sqrt{(\mathbf{r} - \mathbf{r}') \cdot (\mathbf{r} - \mathbf{r}')} = \sqrt{r^2 - 2(\mathbf{r} \cdot \mathbf{r}') + r'^2}, \quad (1.2.83)$$

such that for \mathbf{R} in the far-zone we have $r \gg r'$, hence $\frac{\mathbf{R}}{|\mathbf{R}|} = \hat{\mathbf{R}} \approx \hat{\mathbf{r}}$ and the dominant terms of a Taylor expansion for the square root gives

$$R = r \sqrt{1 - 2 \frac{(\hat{\mathbf{r}} \cdot \mathbf{r}')}{r} + \left(\frac{r'}{r} \right)^2} \approx r \left[1 - \frac{(\hat{\mathbf{r}} \cdot \mathbf{r}')}{r} \right] = r - \hat{\mathbf{r}} \cdot \mathbf{r}'. \quad (1.2.84)$$

Thus, the Green's function may be approximated as

$$G(\mathbf{r}|\mathbf{r}'; \omega) = \frac{e^{-jk|\mathbf{R}|}}{4\pi|\mathbf{R}|} \approx \frac{e^{-jkr}}{4\pi r} e^{jk\hat{\mathbf{r}} \cdot \mathbf{r}'}. \quad (1.2.85)$$

The integral of (1.2.82) becomes

$$\begin{aligned}
 \tilde{\psi}(\mathbf{r}; \omega) \Big|_{r \gg r'} &\approx \oint_{S_0} \frac{e^{-jkr}}{4\pi r} e^{jk\hat{\mathbf{r}} \cdot \mathbf{r}'} \left[\left(jk + \frac{1}{r} \right) \tilde{\psi}(\mathbf{r}'; \omega) (\hat{\mathbf{r}} \cdot \hat{\mathbf{r}}') - \frac{\partial \tilde{\psi}(\mathbf{r}'; \omega)}{\partial r'} \right] dS' \\
 &\approx \frac{e^{-jkr}}{4\pi r} \oint_{S_0} e^{jk\hat{\mathbf{r}} \cdot \mathbf{r}'} \left[\left(jk + \frac{1}{r} \right) \tilde{\psi}(\mathbf{r}'; \omega) (\hat{\mathbf{r}} \cdot \hat{\mathbf{r}}') - \frac{\partial \tilde{\psi}(\mathbf{r}'; \omega)}{\partial r'} \right] dS' \\
 &\approx_{kr \gg 1} \frac{e^{-jkr}}{4\pi r} \oint_{S_0} e^{jk\hat{\mathbf{r}} \cdot \mathbf{r}'} \left[jk \tilde{\psi}(\mathbf{r}'; \omega) (\hat{\mathbf{r}} \cdot \hat{\mathbf{r}}') - \frac{\partial \tilde{\psi}(\mathbf{r}'; \omega)}{\partial r'} \right] dS'. \quad (1.2.86)
 \end{aligned}$$

Finally, the radiation pattern is computed from (1.2.86), removing the distance r dependence by the following limit

$$\begin{aligned}
 \mathcal{P}(\hat{\mathbf{r}}; \omega) &= \lim_{r \rightarrow \infty} 4\pi r^2 |\tilde{\psi}(\mathbf{r}; \omega)|^2 \\
 &= \left| \oint_{S_0} e^{jk\hat{\mathbf{r}} \cdot \mathbf{r}'} \left[jk\tilde{\psi}(\mathbf{r}'; \omega) (\hat{\mathbf{r}} \cdot \hat{\mathbf{r}}') - \frac{\partial \tilde{\psi}(\mathbf{r}'; \omega)}{\partial r'} \right] dS' \right|^2 \\
 &= |\tilde{\psi}_r^*|^2,
 \end{aligned} \tag{1.2.87}$$

where $\tilde{\psi}_r^* \in \mathbb{C}$ is the *far field detector*.

1.2.2.1 Pattern in spherical coordinates

For the spherical symmetry of the sphere's N2F problem, it is interesting to express the vectors \mathbf{r} and \mathbf{r}' with spherical variables for the computation of (1.2.87). To evaluate the scalar products, we can rely on Cartesian unit vectors basis with the components of the vectors are dependent on spherical variables. The unit vectors involved in the far field detector are,

$$\begin{aligned}
 \hat{\mathbf{r}}' &= \cos(\theta_{r'}) \cos(\phi_{r'}) \hat{\mathbf{i}}_x + \cos(\theta_{r'}) \sin(\phi_{r'}) \hat{\mathbf{i}}_y + \sin(\theta_{r'}) \hat{\mathbf{i}}_z, \\
 \hat{\mathbf{r}} &= \cos(\theta_r) \cos(\phi_r) \hat{\mathbf{i}}_x + \cos(\theta_r) \sin(\phi_r) \hat{\mathbf{i}}_y + \sin(\theta_r) \hat{\mathbf{i}}_z,
 \end{aligned} \tag{1.2.88}$$

and their scalar product is given by

$$\begin{aligned}
 \xi(\theta_r, \phi_r, \theta_{r'}, \phi_{r'}) &= \cos(\theta_r) \cos(\phi_r) \cos(\theta_{r'}) \cos(\phi_{r'}) + \\
 &\quad \cos(\theta_r) \sin(\phi_r) \cos(\theta_{r'}) \sin(\phi_{r'}) + \\
 &\quad \sin(\theta_r) \sin(\theta_{r'}) \\
 &= \sin(\theta_r) \sin(\theta_{r'}) \cos(\phi_r - \phi_{r'}) + \\
 &\quad \cos(\theta_r) \cos(\theta_{r'}).
 \end{aligned} \tag{1.2.89}$$

The relation (1.2.87) can be written as follows

$$\mathcal{P}(\theta_r, \phi_r; \omega) = \left| \int_0^{2\pi} \int_0^\pi e^{jk r' \xi'} \left[jk \tilde{\psi}'_{r'} \xi' - \frac{\partial \tilde{\psi}'_{r'}}{\partial r'} \right] r'^2 \sin(\theta_{r'}) d\theta_{r'} d\phi_{r'} \right|^2, \tag{1.2.90}$$

where $\tilde{\psi}'_{r'} = \tilde{\psi}(r', \theta_{r'}, \phi_{r'}; \omega)$ and $\xi' = \xi(\theta_r, \phi_r, \theta_{r'}, \phi_{r'})$.

1.2.2.2 Numerical implementation

We present the results obtained from a Matlab implementation that computes the pattern from planar array of 3 by 5 point sources ($N = 15$ point sources), the firsts disposed along the x direction and the latter along y . The point sources or array elements are chosen to be equally spaced of $\lambda/2$. Due to power normalization, the maximum gain or *directivity* the array can achieve is given by the total number of point sources, that is $10 \log_{10}(N) \approx 11.76$ dB [4].

From (1.2.86), we can see that the values we have to compute in the first step are the near field $\tilde{\psi}(\mathbf{r}'; \omega)$ and its radial derivative $\frac{\partial \tilde{\psi}(\mathbf{r}'; \omega)}{\partial r'}$. The first is achieved by the numerical integration of the volume integral (1.2.78), considering $\tilde{S}(\mathbf{v}_n, \omega) = \tilde{S}_n \delta(\mathbf{v} - \mathbf{v}_n)$, $n = 1 \dots N$. We obtain

$$\tilde{\psi}_m(\mathbf{r}'_m; \omega) = \sum_{n=1}^N \frac{e^{-jk|\mathbf{r}'_m - \mathbf{v}_n|}}{4\pi|\mathbf{r}'_m - \mathbf{v}_n|} \tilde{S}_n \quad n = 1 \dots N, m = 1 \dots M \quad (1.2.91)$$

where we have discretized the sphere in M sampling points. The second one, noting that $\tilde{S}(\mathbf{v}, \omega)$ has no dependence on the vector \mathbf{r}' , can be evaluated proceeding in the following manner

$$\begin{aligned} \frac{\partial \tilde{\psi}(\mathbf{r}'; \omega)}{\partial r'} &= \frac{\partial}{\partial r'} \int_{V_{S_0}} \frac{e^{-jk|\mathbf{r}' - \mathbf{v}|}}{4\pi|\mathbf{r}' - \mathbf{v}|} \tilde{S}(\mathbf{v}, \omega) dV_v \\ &= \int_{V_{S_0}} \frac{\partial}{\partial r'} \frac{e^{-jk|\mathbf{r}' - \mathbf{v}|}}{4\pi|\mathbf{r}' - \mathbf{v}|} \tilde{S}(\mathbf{v}, \omega) dV_v \quad \forall \mathbf{r}' \neq \mathbf{v} \\ &= - \int_{V_{S_0}} \left(jk + \frac{1}{|\mathbf{r}' - \mathbf{v}|} \right) \frac{e^{-jk|\mathbf{r}' - \mathbf{v}|}}{4\pi|\mathbf{r}' - \mathbf{v}|} \left(\frac{\mathbf{r}' - \mathbf{v}}{|\mathbf{r}' - \mathbf{v}|} \cdot \hat{\mathbf{r}}' \right) \tilde{S}(\mathbf{v}, \omega) dV_v, \end{aligned} \quad (1.2.92)$$

which becomes, in a numerical form,

$$\frac{\partial \tilde{\psi}_m(\mathbf{r}'_m; \omega)}{\partial r'_m} = - \sum_{n=1}^N \left(jk + \frac{1}{|\mathbf{r}'_m - \mathbf{v}_n|} \right) \frac{e^{-jk|\mathbf{r}'_m - \mathbf{v}_n|}}{4\pi|\mathbf{r}'_m - \mathbf{v}_n|} \left(\frac{\mathbf{r}'_m - \mathbf{v}_n}{|\mathbf{r}'_m - \mathbf{v}_n|} \cdot \hat{\mathbf{r}}'_m \right) \tilde{S}_n \quad n = 1 \dots N, m = 1 \dots M. \quad (1.2.93)$$

The scalar N2F from a bounding sphere, varying the sampling resolution in terms of wavelengths and using a *midpoint*¹² numerical integration of (1.2.87) over the sphere,

¹² The fields sampling points are located in the middle of surface patches ΔS_n , and an integration of a discretized function Φ_n is obtained by the sum $\sum_{n=1}^N \Phi_n \Delta S_n$. The *Trapezoidal rule* have also been tested, with no significant improvement in the pattern error. Further enhancements can be achieved with *Gaussian quadrature*. [12]

will be compared to the direct computation of the pattern (the gain for several look angles). We obtain the N2F numerical formula

$$\begin{aligned} \mathcal{P}_{p\text{N2F}}(\hat{\mathbf{r}}_p; \omega) &= \left| \tilde{\psi}_{r_p}^* \right|^2 = \\ &= \left| \sum_{m=1}^M e^{jk\hat{\mathbf{r}}_p \cdot \mathbf{r}'_m} \left[jk\tilde{\psi}_m(\mathbf{r}'_m; \omega) (\hat{\mathbf{r}}_p \cdot \hat{\mathbf{r}}'_m) - \frac{\partial \tilde{\psi}_m(\mathbf{r}'_m; \omega)}{\partial r'_m} \right] \Delta S_m \right|^2. \\ &\quad m = 1 \dots M, p = 1 \dots P \end{aligned} \quad (1.2.94)$$

The direct field computation is derived from formula (1.2.91), with \mathbf{r}'_m to become the far-zone unit vectors $\hat{\mathbf{r}}_p$, assuming the far field approximation (1.2.85) and applying the far-zone limit used in (1.2.87), that is

$$\begin{aligned} \mathcal{P}_{p\text{Direct}}(\hat{\mathbf{r}}_p; \omega) &= \lim_{r_p \rightarrow \infty} 4\pi r_p^2 \left| \frac{e^{-jk r_p}}{4\pi r_p} \sum_{n=1}^N e^{jk\hat{\mathbf{r}}_p \cdot \mathbf{v}_n} \tilde{S}_n \right|^2 \\ &= \left| \sum_{n=1}^N e^{jk\hat{\mathbf{r}}_p \cdot \mathbf{v}_n} \tilde{S}_n \right|^2 \quad n = 1 \dots N, p = 1 \dots P \end{aligned} \quad (1.2.95)$$

The geometry of the discretized domain is depicted in figure 1.6. The radius of the sphere is set to be radially $\lambda/2$ away from the corner elements, i.e. $|\mathbf{r}'_m| = 1.618\lambda$ and the angles $\theta_{r'}$ and $\phi_{r'}$ of near field sampling are computed assuming $|\mathbf{r}'_m| \Delta\theta_{r'} \approx |\mathbf{r}'_m| \Delta\phi_{r'} \approx \lambda/10$.

Notice that the radial extension of the sphere from the array cannot be lower than the sampling resolution (inferior limit), and the superior limit is associated to the increasing memory consumption, in order to keep the desired resolution, as the sphere radius grows.

Figures 1.7 and 1.8 show the radiation patterns computed¹³, respectively, in the $\phi_r = 0^\circ$ (XZ) and $\phi_r = 90^\circ$ (YZ) cut planes. The solid line corresponds to the N2F computed pattern while the crosses correspond to the direct pattern.

Let us discuss now on the error committed in the N2F computation, relatively to the direct one. In effect, the values of the gain in the two cases are slightly different, mainly due to the accuracy of the integration method used. Figure 1.9 shows the

¹³ Notice that the plotted patterns in 1.7 and 1.8 correspond to the *array factor*, the *element factor* being unitary in an array analysis. [2]

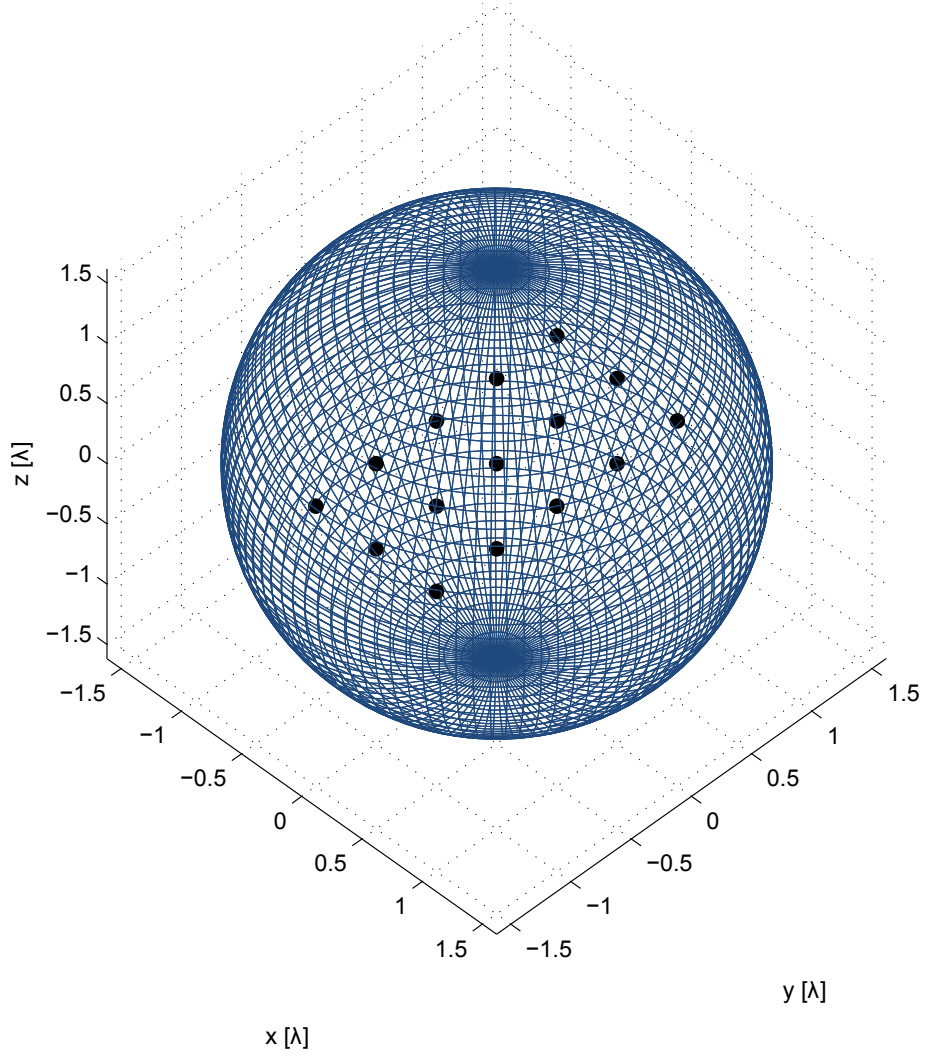


Figure 1.6: N2F bounding sphere and 3 by 5 point sources, with $\lambda/10$ sampling resolution.

error in $\tilde{\psi}_{r \text{ N2F}}^*$ relatively to $\tilde{\psi}_{r \text{ Direct}}^*$ in the \mathcal{L}^1 , \mathcal{L}^2 and \mathcal{L}^∞ norms [17] for different resolutions, starting from $\lambda/2$ and progressively halving the resolution. We have chosen the \mathcal{L}^2 norm or *Euclidean norm* to compare the values of $\tilde{\psi}_{r \text{ N2F}}^*$ and $\tilde{\psi}_{r \text{ Direct}}^*$. This is motivated by the fact that the \mathcal{L}^2 norm preserves energy information. Thus, the scalar N2F relative error will be given by the following relation¹⁴

$$\mathfrak{E}_{[\lambda/n]} = \frac{\|\tilde{\psi}_{r \text{ Direct}}^* - \tilde{\psi}_{r \text{ N2F}}^*\|_2}{\|\tilde{\psi}_{r \text{ Direct}}^*\|_2} \quad n \in \mathbb{N}^+ / \{1\}. \quad (1.2.96)$$

As we can see in figures 1.7 and 1.8, the sampling resolution of $\lambda/10$ with an er-

¹⁴ For *Shannon's sampling theorem*, the lowest sampling resolution that can be used equals $\lambda/2$.

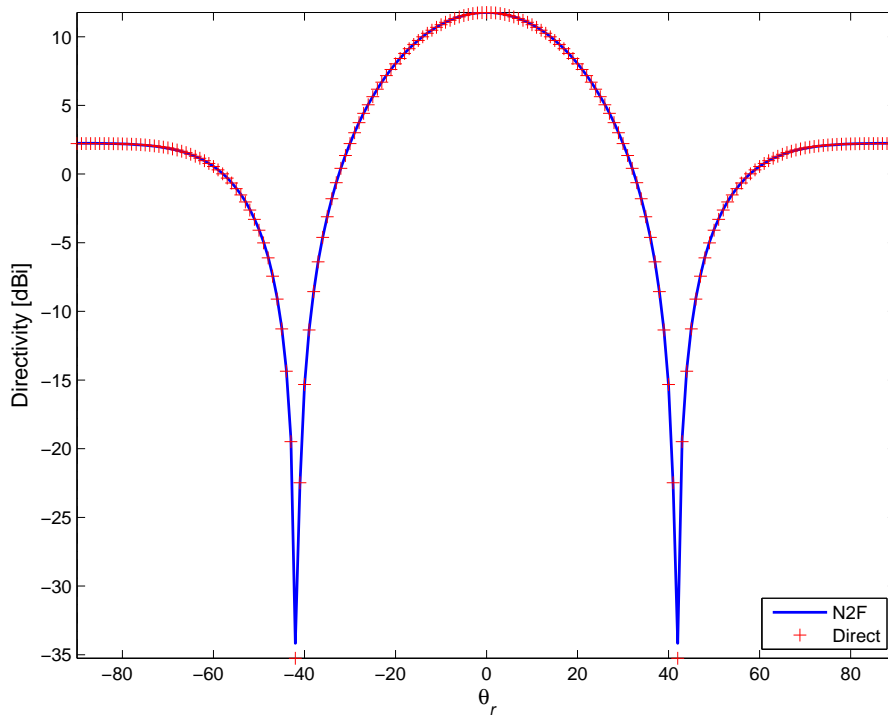


Figure 1.7: Pattern computed for equally phased point sources (broadside pattern) on the $\phi = 0^\circ$ cut plane with $\lambda/10$ sampling resolution.

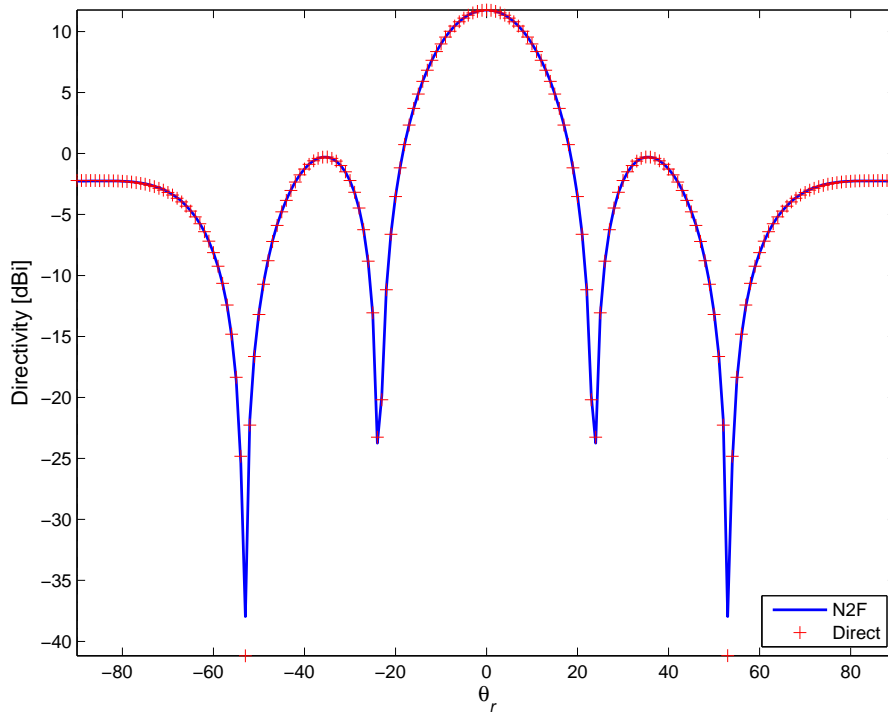


Figure 1.8: Pattern computed for equally phased point sources on the $\phi = 90^\circ$ cut plane with $\lambda/10$ sampling resolution.

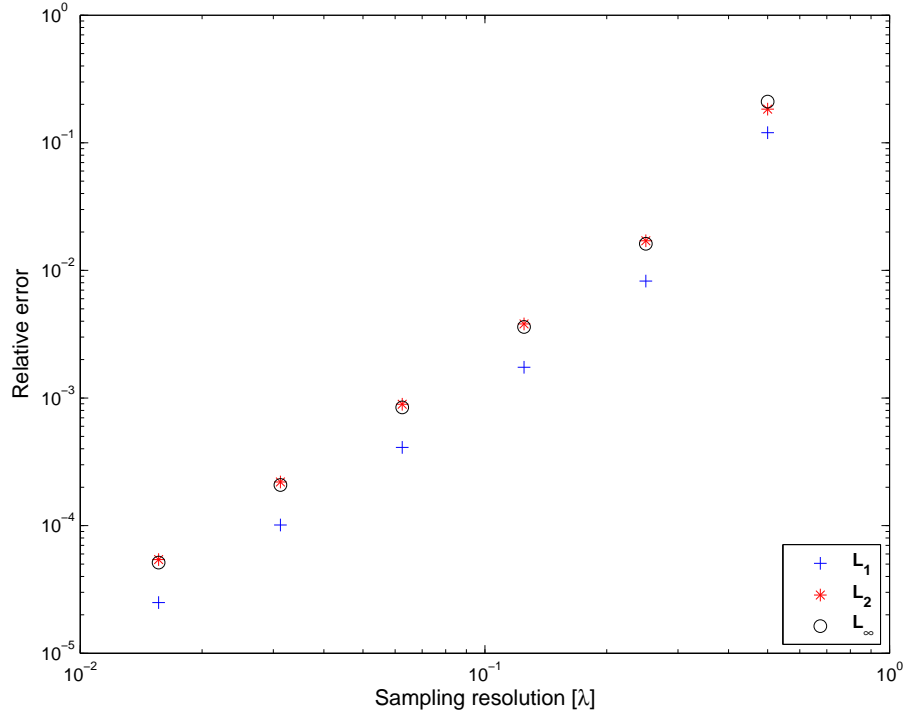


Figure 1.9: Relative broadside far field detector $\tilde{\psi}_r^*$ error in the \mathcal{L}^1 , \mathcal{L}^2 and \mathcal{L}^∞ norms for several sampling resolutions.

ror of $\varepsilon_{[\lambda/10]} = 2.398 \cdot 10^{-3}$ for 181 *look angles* ($\Delta\theta_r = 1^\circ$), that is the far zone directions in which $\tilde{\psi}_{r \text{ N2F}}^*$ and $\tilde{\psi}_{r \text{ Direct}}^*$ are computed, provides a pattern that can be considered reasonably accurate. As we can see in figure 1.10, the number of look angles chosen does not significantly modify the error order even if the pattern is coarsely sampled (low number of look angles). However, there is a converging behavior while increasing the pattern sampling resolution ($\Delta\theta_r \rightarrow 0$). In order to define an accuracy criterion for the pattern computation, we will assume error values $\varepsilon_{[\lambda/n]} \leq 5 \cdot 10^{-3}$ to be admissible, and the integer n will be consequently defined for the employed bounding surface. To motivate this choice, an example of pattern resulting in a higher error value ($\varepsilon_{[\lambda/3]} = 3.387 \cdot 10^{-2}$) is given in figure 1.11, showing a sensible misfit comparing to the reference pattern (directly computed), especially in the side lobes.

Before we proceed with the N2F computations from a parallelepiped, let us face the steering operation, choosing opportunely the phase of \tilde{S}_n , $n = 1 \dots N$, such that the main lobe in the pattern results in a desired direction. For a planar array with arbitrarily spaced sources, the phase values are $\phi_n = -k(x_n \sin(\theta_x) + y_n \sin(\theta_y))$ [2] where

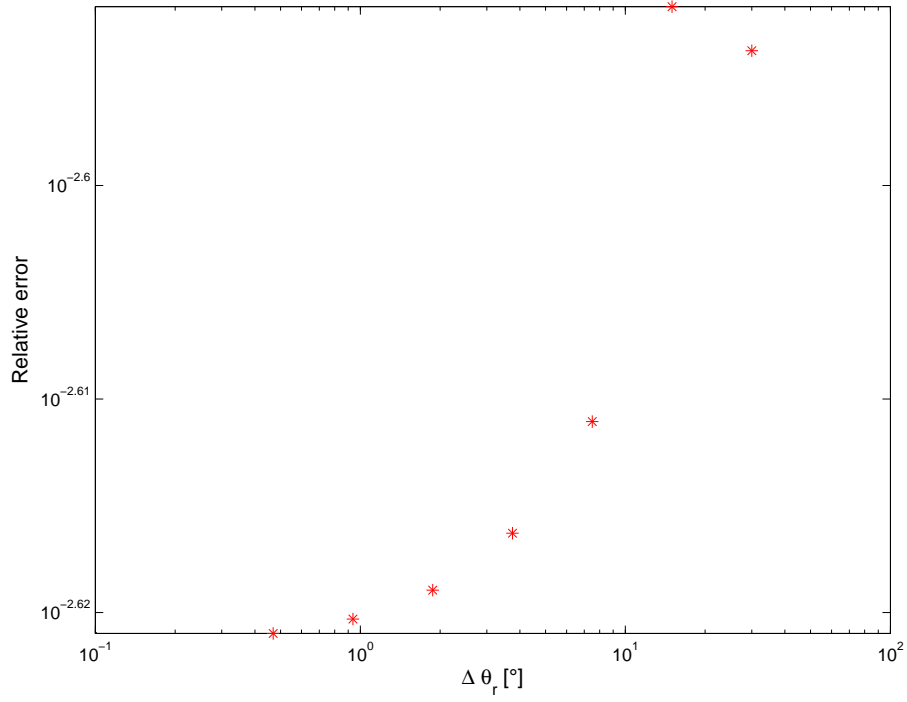


Figure 1.10: Relative broadside far field detector pattern $\tilde{\psi}_r^*$ error in the \mathcal{L}^2 norm for several $\Delta\theta_r$, i.e. increasing the pattern resolution.

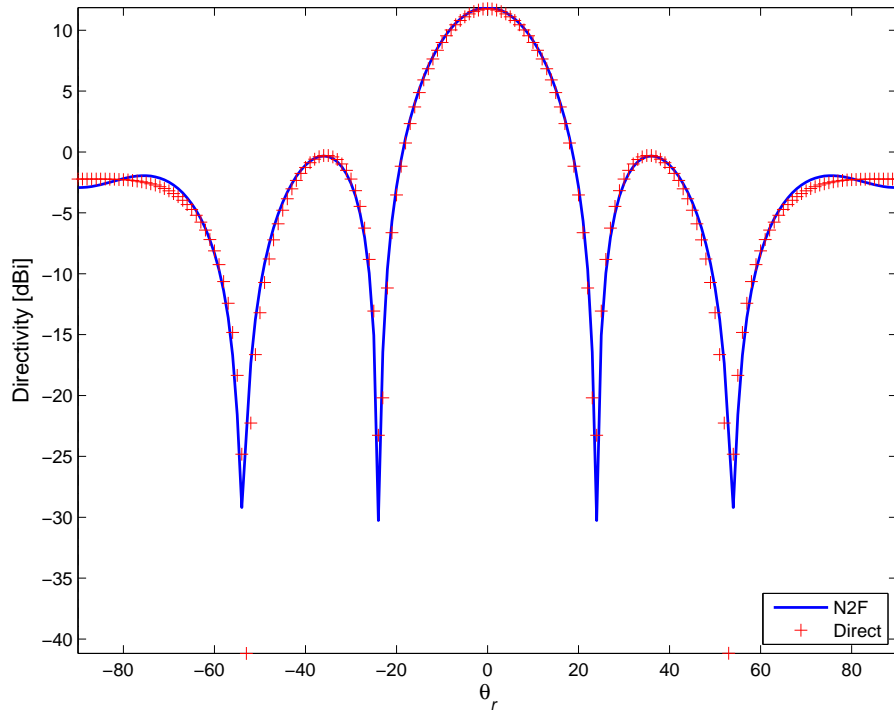


Figure 1.11: Pattern computed on the $\phi = 90^\circ$ cut plane with $\lambda/3$ sampling resolution. Notice the visible error on the side lobes.

(x_n, y_n) are the position coordinates of the n^{th} source, θ_x and θ_y are, respectively, the *scan angles* along the x and y directions. Considering also the power normalization (see section 1.2.1), the sources phasors become

$$\tilde{S}_n = \frac{1}{\sqrt{N}} e^{-jk(x_n \sin(\theta_x) + y_n \sin(\theta_y))} \quad n = 1 \dots N \quad (1.2.97)$$

Figures 1.12 and 1.13 show the patterns on the cut planes XZ and YZ resulting from the steering operation of $\theta_x = 10^\circ$ and $\theta_y = 30^\circ$.

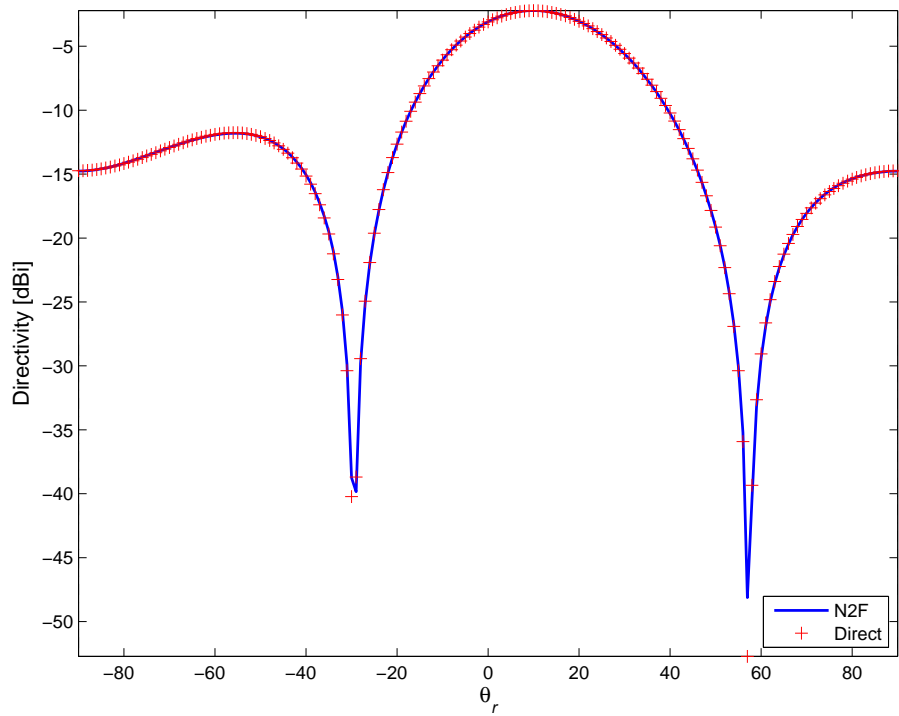


Figure 1.12: Pattern computed on the $\phi = 0^\circ$ cut plane with $\lambda/10$ sampling resolution and scan angles $\theta_x = 10^\circ$ and $\theta_y = 30^\circ$.

1.2.3 Computations on a bounding parallelepiped

The N2F computation on a bounding parallelepiped or box is achieved similarly to the one from a bounding sphere. Figure 1.14 shows the mesh realized for the array of 3 by 5 point sources, with a resolution of $\lambda/10$. The minimum distance between a point source and a surface patch is of $\lambda/2$.

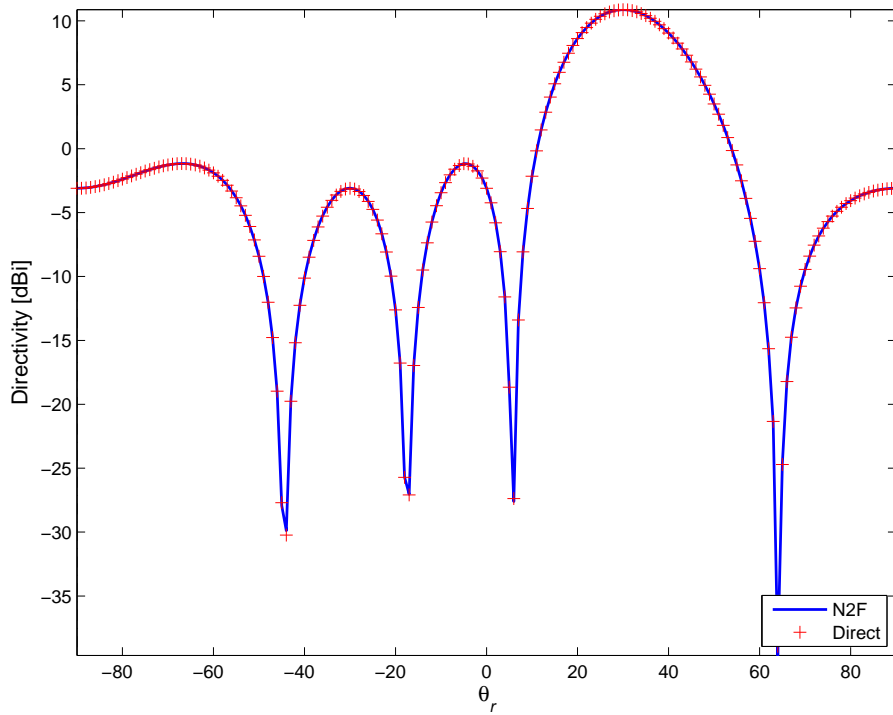


Figure 1.13: Pattern computed on the $\phi = 90^\circ$ cut plane with $\lambda/10$ sampling resolution and scan angles $\theta_x = 10^\circ$ and $\theta_y = 30^\circ$.

The main difference between the two kinds of sampling geometries resides in the fact that the box requires a lower number of samples to achieve the same error as sphere's one. The box is in fact a closer encompassing surface. As we get far away from the point sources, we need a higher number of near field sampling points to keep the resolution desired. In effect, the sphere surface patches (ΔS_m) become larger as we increase the sphere radius, leading to a coarse integration of the near fields and their derivatives. Furthermore, as we get away from the sources, the fields present higher structure, until they behave like the radiation patterns, that is varying rapidly of several orders of magnitude. Thus, we need to lower the dimension of the sphere patches for an accurate integration¹⁵. In figure 1.15 and table 1.1, it is shown the improvement we obtain using a bounding box. In the average and for the chosen array, the box needs about half of the sphere's number of sampling points, thus halving the memory requirements while keeping the same error level.

¹⁵ A triangulated sphere, where the surface patches are composed of triangles of equal size, have also been used. Nevertheless, this kind of discretization approach leads to higher computational re-

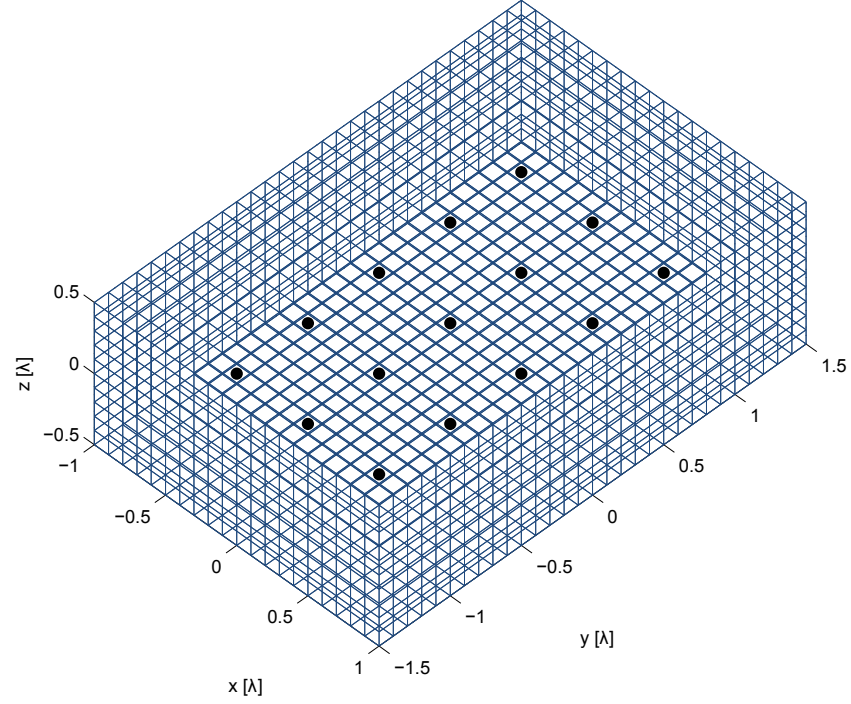


Figure 1.14: N2F bounding parallelepiped and 3 by 5 point sources, with $\lambda/10$ sampling resolution.

Resolution	Sphere samples	Sphere error	Box samples	Box error
$\lambda/2$	180	$2.11 \cdot 10^{-1}$	88	$1.61 \cdot 10^{-1}$
$\lambda/4$	760	$1.4 \cdot 10^{-2}$	352	$1.68 \cdot 10^{-2}$
$\lambda/8$	3 159	$3.09 \cdot 10^{-3}$	1 408	$3.71 \cdot 10^{-3}$
$\lambda/16$	12 960	$7.24 \cdot 10^{-4}$	5 632	$9.01 \cdot 10^{-4}$
$\lambda/32$	52 325	$1.78 \cdot 10^{-4}$	22 528	$2.24 \cdot 10^{-4}$
$\lambda/64$	210 600	$4.39 \cdot 10^{-5}$	90 112	$5.58 \cdot 10^{-5}$
$\lambda/128$	844 349	$1.09 \cdot 10^{-5}$	360 448	$1.39 \cdot 10^{-5}$

Table 1.1: Plotted values of figure 1.15.

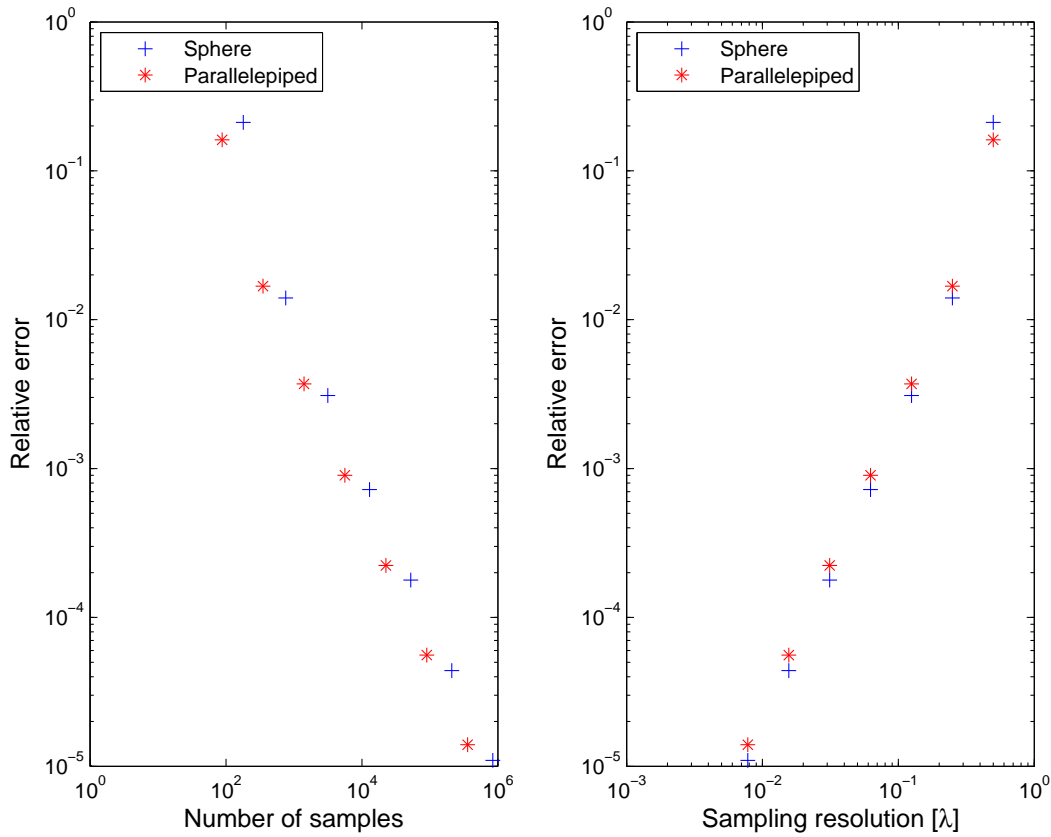


Figure 1.15: Near fields sampling points comparisons between the one required by the sphere and those for the parallelepiped for the 3 by 5 point sources array.

An interesting issue, seeking for further sampling coarsening to reduce the memory requirements, is to see what may happen if we omit some of the faces of the box, keeping the ones we expect to have higher power. The near field sampled on the box in a broadside steering condition are plotted in figures 1.16 and 1.17.

We can see that the highest intensities are located on the top and bottom faces. To avoid significant disturbance in the remotion of the lateral faces, we prefer to further reduce the fields intensities on those faces increasing the top and bottom planes dimensions as shown in figure 1.18. The omitted edge faces of the box have been set to lie 2.5λ away from the point sources located at the corners of the array. The patterns computed from the two planes are depicted in figures 1.19 and 1.20. The main lobe results to be accurately matched, and the error grows as we move to *end fire* ($\pm 90^\circ$)

quirements.

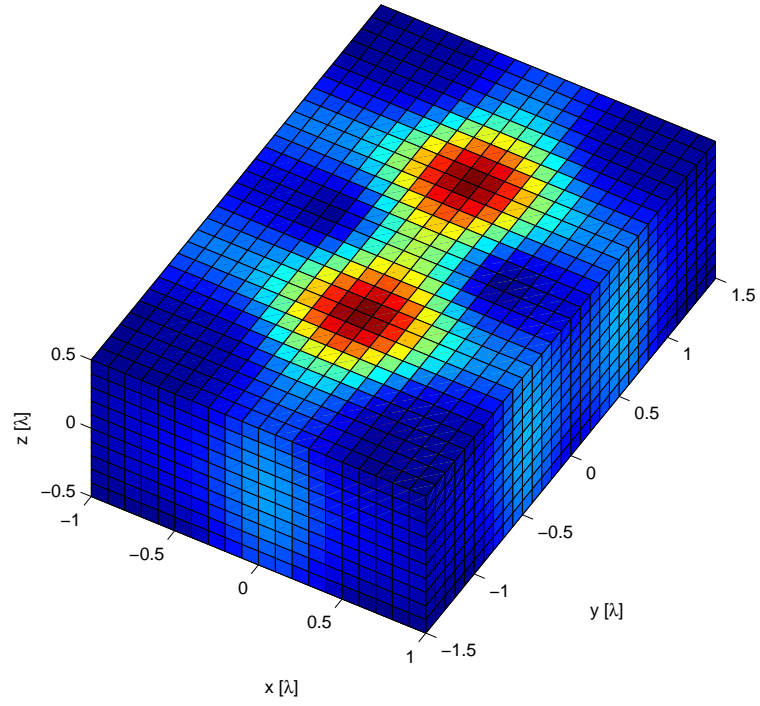


Figure 1.16: Near fields intensity $|\tilde{\psi}_m(\mathbf{r}'_m; \omega)|$ on the box with faces $\lambda/2$ away from the point sources.

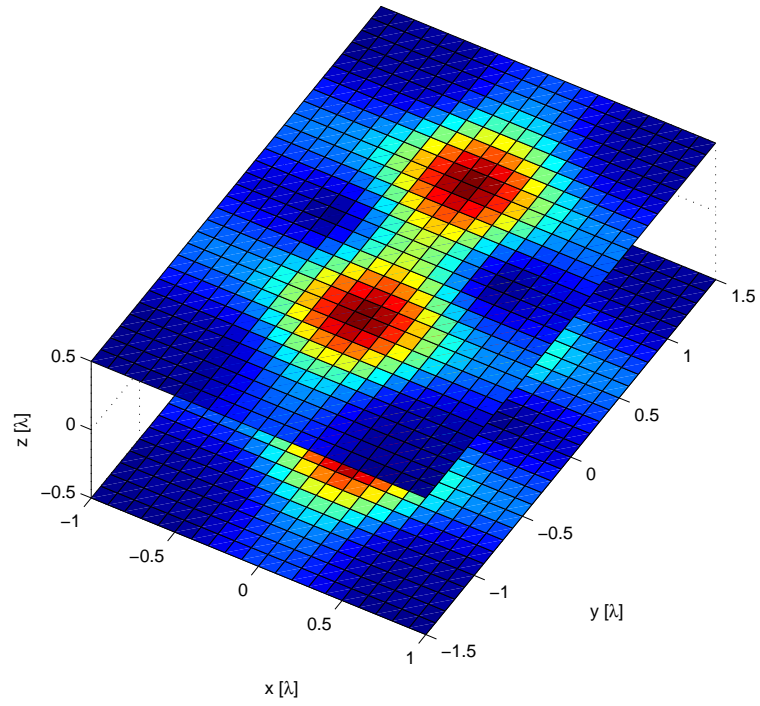


Figure 1.17: Near fields intensity on the top and bottom faces.

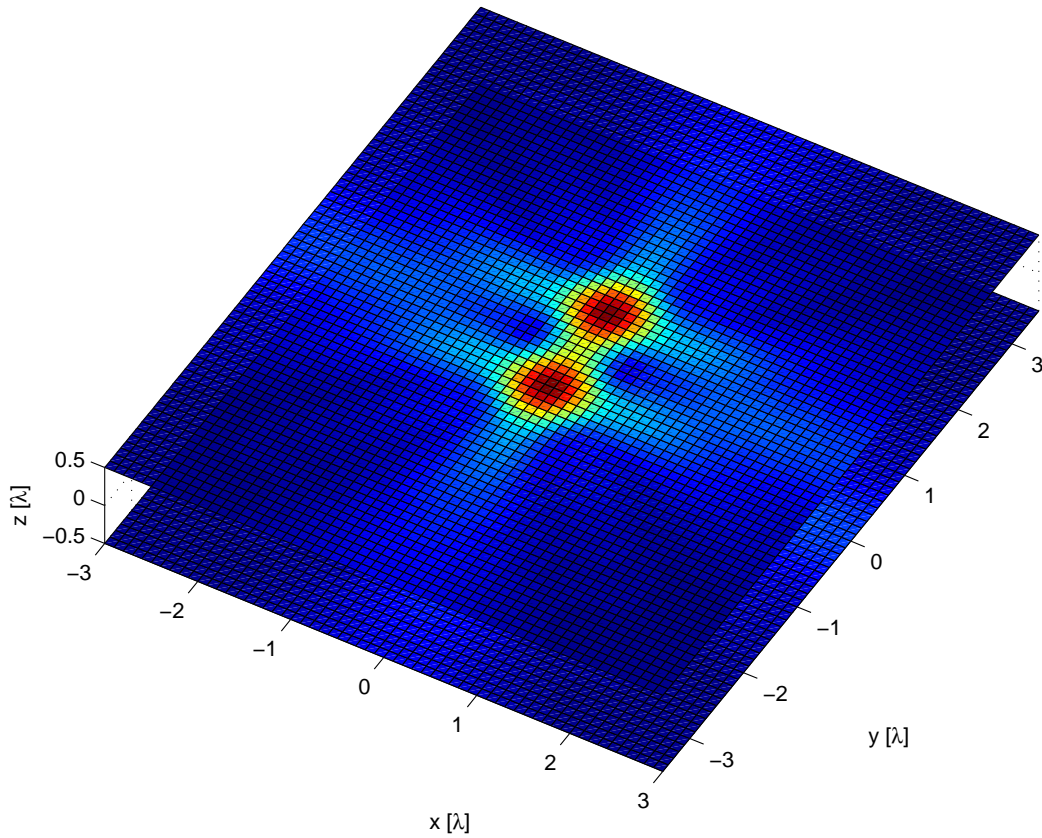


Figure 1.18: Top and bottom planes for truncated surface computation. Lateral extension from the edge point sources is set to 2.5λ .

look angles : the total pattern error is of $\varepsilon_{[\lambda/10]} = 0.214$. It is clear that with this configuration, the scan angles will be restricted to a lower range around the broadside direction in order to preserve the main lobe accuracy, and an increase in the planes dimensions results into a wider range. However this increases the memory requirements, leading into a less numerically efficient configuration, especially for very large arrays (50 by 50 radiating elements for example).

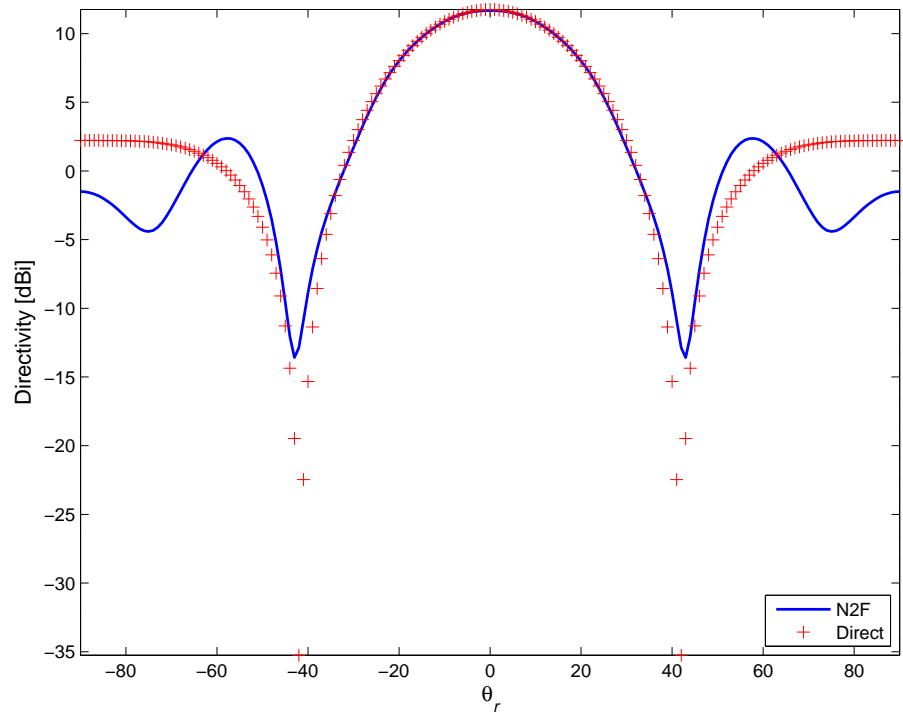


Figure 1.19: Pattern computed from the top and bottom faces of the box on the $\phi = 0^\circ$ cut plane ($\lambda/10$ sampling resolution).

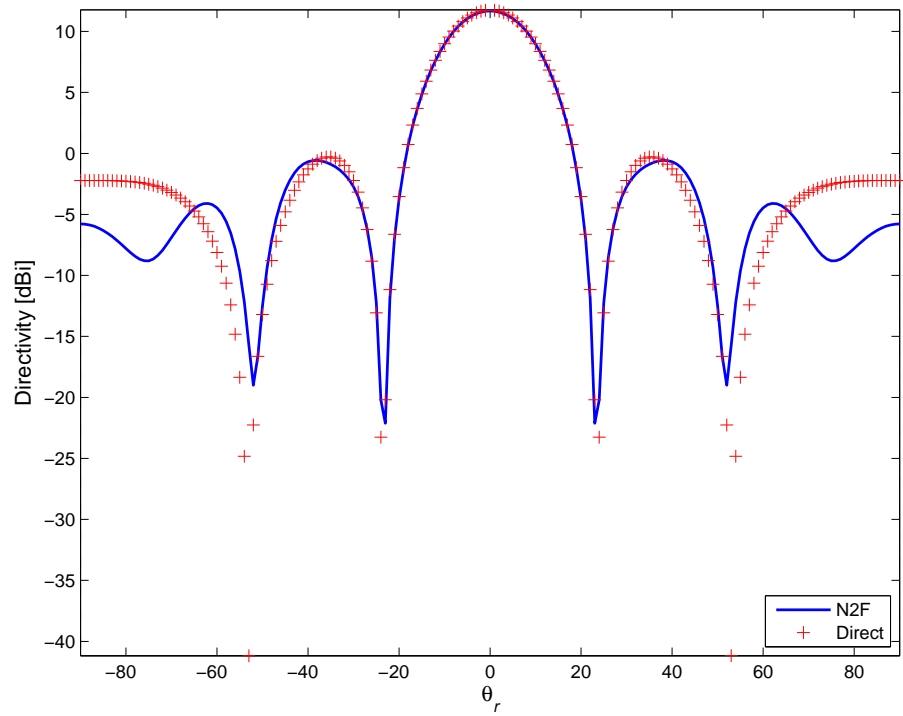


Figure 1.20: Pattern computed from the top and bottom faces of the box on the $\phi = 90^\circ$ cut plane ($\lambda/10$ sampling resolution).

1.3 Vector near fields to far fields transformations

In this section, we present a numerical implementation of the vector near fields to far fields transformations (vector N2F), relying on the mathematical formulation discussed in section 1.1.4. The computation steps are the same as discussed in section 1.2.1. The results of an implementation in Matlab environment will be shown, considering as enclosing surface a parallelepiped. These results will be compared to ones obtained by means of the commercial CAD FEKO¹⁶.

1.3.1 Direct computation of the fields from current sources

The Kottler's formulas (1.1.73-1.1.74) contains informations on both direct fields computations (first integral) and on N2F fields computations (second integral). To numerically evaluate the vector N2F, we have chosen to enclose an array of 3 by 5 *Huygens' sources* [3] with a box, in a similar manner as it has been done in section 1.2.3. Huygens' sources are made of an infinitesimal electric current $\tilde{\mathbf{J}}(\mathbf{r}'; \omega)$ crossing perpendicularly an infinitesimal magnetic current $\tilde{\mathbf{J}}_m(\mathbf{r}'; \omega)$. The amplitude of the magnetic current has to be ζ times bigger to achieve the same radiated power than the electric one. Hugins' sources are constructed as if they where derived from far fields (plane wave behavior) and applying the equivalence principle (analog to Huygens' principle with equivalent currents, from which the name given to the sources). Now, to build the array, we have chosen the electric currents to be directed in $-\hat{\mathbf{y}}$ and the magnetic ones in $\hat{\mathbf{x}}$, such that the main radiation lobe is to be $\hat{\mathbf{z}}$ -directed. Thus, we can express the currents of the array as

$$\tilde{\mathbf{J}}(\mathbf{r}'; \omega) = -\tilde{J}\delta(\mathbf{r} - \mathbf{r}')\hat{\mathbf{y}} \quad (1.3.98)$$

$$\tilde{\mathbf{J}}_m(\mathbf{r}'; \omega) = \zeta \tilde{J}_m\delta(\mathbf{r} - \mathbf{r}')\hat{\mathbf{x}} \quad (1.3.99)$$

where $\delta(\mathbf{r} - \mathbf{r}')$ is the Dirac delta, with its well known sifting property of integrals.

¹⁶ FEKO[®] EM Software & Systems. Further informations available on www.feko.info.

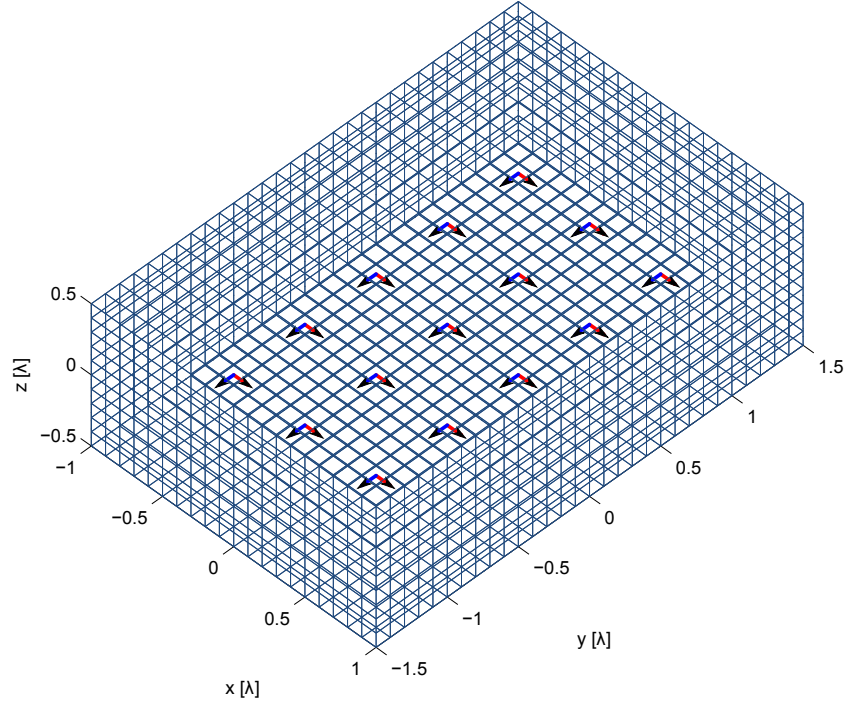


Figure 1.21: N2F bounding parallelepiped and 3 by 5 Huygens' sources, with $\lambda/10$ sampling resolution.

Let us now express analytically the terms involved with the Green's function (1.2.76) in the first integrals of Kottler's equations. Using the relation

$$\nabla G(\mathbf{r}|\mathbf{r}'; \omega) = -\nabla' G(\mathbf{r}|\mathbf{r}'; \omega) = \hat{\mathbf{R}} \frac{\partial}{\partial R} G(R; \omega), \quad (1.3.100)$$

with

$$G(\mathbf{r}|\mathbf{r}'; \omega) = \frac{e^{-jk|\mathbf{r}-\mathbf{r}'|}}{4\pi|\mathbf{r}-\mathbf{r}'|} = \frac{e^{-jkR}}{4\pi R} = G(R; \omega),$$

we have

$$\nabla' G(\mathbf{r}|\mathbf{r}'; \omega) = \left(jk + \frac{1}{R} \right) \frac{e^{-jkR}}{4\pi R} \hat{\mathbf{R}}. \quad (1.3.101)$$

We need now to express explicitly the local gradient of (1.3.101) [11] which is a vector-valued function of R . To do this, we express in spherical components the gradient operator to evaluate $\nabla A_R(R) \hat{\mathbf{R}}$, A_R being the radial component of a vector-valued function \mathbf{A} of R , where the transverse components A_θ and A_ϕ are null. We obtain

$$\nabla A(R) = \left(\hat{\mathbf{R}} \frac{\partial}{\partial R} + \hat{\boldsymbol{\theta}} \frac{1}{R} \frac{\partial}{\partial \theta} + \hat{\boldsymbol{\phi}} \frac{1}{R \sin(\theta)} \frac{\partial}{\partial \phi} \right) A_R \hat{\mathbf{R}}$$

$$\begin{aligned}
&= \hat{\mathbf{R}} \frac{\partial}{\partial R} A_R \hat{\mathbf{R}} + \hat{\boldsymbol{\theta}} \frac{1}{R} \frac{\partial}{\partial \theta} A_R \hat{\mathbf{R}} + \hat{\boldsymbol{\phi}} \frac{1}{R \sin(\theta)} \frac{\partial}{\partial \phi} A_R \hat{\mathbf{R}} \\
&= \hat{\mathbf{R}} \hat{\mathbf{R}} \frac{\partial}{\partial R} A_R + \hat{\boldsymbol{\theta}} \hat{\boldsymbol{\theta}} \frac{1}{R} A_R + \hat{\boldsymbol{\phi}} \hat{\boldsymbol{\phi}} \frac{1}{R} A_R,
\end{aligned} \tag{1.3.102}$$

where we have made the substitutions $\frac{\partial \hat{\mathbf{R}}}{\partial \theta} = \hat{\boldsymbol{\theta}}$ and $\frac{1}{\sin(\theta)} \frac{\partial \hat{\mathbf{R}}}{\partial \phi} = \hat{\boldsymbol{\phi}}$. With the use of the *identity dyadic* $\bar{\bar{\mathbf{I}}} = \hat{\mathbf{R}} \hat{\mathbf{R}} + \hat{\boldsymbol{\theta}} \hat{\boldsymbol{\theta}} + \hat{\boldsymbol{\phi}} \hat{\boldsymbol{\phi}} = \hat{\mathbf{x}} \hat{\mathbf{x}} + \hat{\mathbf{y}} \hat{\mathbf{y}} + \hat{\mathbf{z}} \hat{\mathbf{z}}$ in both spherical and Cartesian components, equation (1.3.102) can be rewritten as

$$\nabla A(R) = \hat{\mathbf{R}} \hat{\mathbf{R}} \frac{\partial}{\partial R} A_R + \left(\bar{\bar{\mathbf{I}}} - \hat{\mathbf{R}} \hat{\mathbf{R}} \right) \frac{1}{R} A_R. \tag{1.3.103}$$

Now, $A(R)$ is substituted by $\nabla' G(\mathbf{r}|\mathbf{r}'; \omega)$ and using (1.3.100) we can write

$$\nabla' \nabla' G(\mathbf{r}|\mathbf{r}'; \omega) = - \left(\hat{\mathbf{R}} \hat{\mathbf{R}} \frac{\partial}{\partial R} + \left(\bar{\bar{\mathbf{I}}} - \hat{\mathbf{R}} \hat{\mathbf{R}} \right) \frac{1}{R} \right) \left(jk + \frac{1}{R} \right) \frac{e^{-jkR}}{4\pi R}. \tag{1.3.104}$$

Noting that $\tilde{\mathbf{J}} \cdot \bar{\bar{\mathbf{I}}} = \tilde{\mathbf{J}}$, Kottler's equations for an unbounded medium can be rewritten as, with $G = G(R; \omega)$,

$$\begin{aligned}
\tilde{\mathbf{E}}(\mathbf{r}; \omega) &= \frac{1}{j\omega\epsilon} \int_V \left[\tilde{\mathbf{J}} \left(k^2 - \frac{jk}{R} - \frac{1}{R^2} \right) G + (\tilde{\mathbf{J}} \cdot \hat{\mathbf{R}}) \hat{\mathbf{R}} \left(-k^2 + \frac{3jk}{R} + \frac{3}{R^2} \right) G - \right. \\
&\quad \left. j\omega\epsilon \tilde{\mathbf{J}}_m \times \hat{\mathbf{R}} \left(jk + \frac{1}{R} \right) G \right] dV' \\
&= \frac{\zeta k^2}{4\pi} \int_V \left[\tilde{\mathbf{J}} \left(-\frac{j}{kR} - \frac{1}{k^2 R^2} + \frac{j}{k^3 R^3} \right) + (\tilde{\mathbf{J}} \cdot \hat{\mathbf{R}}) \hat{\mathbf{R}} \left(\frac{j}{kR} + \frac{3}{k^2 R^2} - \frac{3j}{k^3 R^3} \right) - \right. \\
&\quad \left. \frac{1}{\zeta} \tilde{\mathbf{J}}_m \times \hat{\mathbf{R}} \left(\frac{j}{kR} + \frac{1}{k^2 R^2} \right) \right] e^{-jkR} dV',
\end{aligned} \tag{1.3.105}$$

$$\begin{aligned}
\tilde{\mathbf{H}}(\mathbf{r}; \omega) &= \frac{1}{j\omega\mu} \int_V \left[\tilde{\mathbf{J}}_m \left(k^2 - \frac{jk}{R} - \frac{1}{R^2} \right) G + (\tilde{\mathbf{J}}_m \cdot \hat{\mathbf{R}}) \hat{\mathbf{R}} \left(-k^2 + \frac{3jk}{R} + \frac{3}{R^2} \right) G + \right. \\
&\quad \left. j\omega\mu \tilde{\mathbf{J}} \times \hat{\mathbf{R}} \left(jk + \frac{1}{R} \right) G \right] dV' \\
&= \frac{k^2}{4\pi\zeta} \int_V \left[\tilde{\mathbf{J}}_m \left(-\frac{j}{kR} - \frac{1}{k^2 R^2} + \frac{j}{k^3 R^3} \right) + \right. \\
&\quad \left. (\tilde{\mathbf{J}}_m \cdot \hat{\mathbf{R}}) \hat{\mathbf{R}} \left(\frac{j}{kR} + \frac{3}{k^2 R^2} - \frac{3j}{k^3 R^3} \right) + \right. \\
&\quad \left. \zeta \tilde{\mathbf{J}} \times \hat{\mathbf{R}} \left(\frac{j}{kR} + \frac{1}{k^2 R^2} \right) \right] e^{-jkR} dV'.
\end{aligned} \tag{1.3.106}$$

We can now compute the fields on the bounding surface, integrating over the volume enclosed and using the sifting property of the Dirac delta. The integration is

done considering each vector component separately in a Cartesian coordinates system. Also, using the far fields approximation of the Green's function by (1.2.85), one can compute the pattern directly from the sources distribution.

1.3.2 Near fields to far fields computations

The second integral term of Kottler's equations (1.1.73-1.1.74) can be straightforwardly obtained from (1.3.105-1.3.106), assuming the current terms to be equivalent currents on the bounding surface, such that the volume integrals reduce into surface integrals. Thus, we have

$$\begin{aligned} \tilde{E}(\mathbf{r}; \omega) = & \frac{\zeta k^2}{4\pi} \oint_{S_0} \left[\tilde{\mathbf{J}}_s^{eq} \left(-\frac{j}{kR} - \frac{1}{k^2 R^2} + \frac{j}{k^3 R^3} \right) + \right. \\ & \left(\tilde{\mathbf{J}}_s^{eq} \cdot \hat{\mathbf{R}} \right) \hat{\mathbf{R}} \left(\frac{j}{kR} + \frac{3}{k^2 R^2} - \frac{3j}{k^3 R^3} \right) - \\ & \left. \frac{1}{\zeta} \tilde{\mathbf{J}}_{ms}^{eq} \times \hat{\mathbf{R}} \left(\frac{j}{kR} + \frac{1}{k^2 R^2} \right) \right] e^{-jkR} dS', \end{aligned} \quad (1.3.107)$$

$$\begin{aligned} \tilde{H}(\mathbf{r}; \omega) = & \frac{k^2}{4\pi\zeta} \oint_{S_0} \left[\tilde{\mathbf{J}}_{ms}^{eq} \left(-\frac{j}{kR} - \frac{1}{k^2 R^2} + \frac{j}{k^3 R^3} \right) + \right. \\ & \left(\tilde{\mathbf{J}}_{ms}^{eq} \cdot \hat{\mathbf{R}} \right) \hat{\mathbf{R}} \left(\frac{j}{kR} + \frac{3}{k^2 R^2} - \frac{3j}{k^3 R^3} \right) + \\ & \left. \zeta \tilde{\mathbf{J}}_s^{eq} \times \hat{\mathbf{R}} \left(\frac{j}{kR} + \frac{1}{k^2 R^2} \right) \right] e^{-jkR} dS', \end{aligned} \quad (1.3.108)$$

where $\tilde{\mathbf{J}}_s^{eq} = \tilde{\mathbf{J}}_s^{eq}(\mathbf{r}'; \omega) = \hat{\mathbf{n}} \times \tilde{\mathbf{H}}(\mathbf{r}'; \omega)$ and $\tilde{\mathbf{J}}_{ms}^{eq} = \tilde{\mathbf{J}}_{ms}^{eq}(\mathbf{r}'; \omega) = -\hat{\mathbf{n}} \times \tilde{\mathbf{E}}(\mathbf{r}'; \omega)$. With the far fields approximation of the Green's function (1.2.85), the second integral term of Kottler's equations (1.3.107-1.3.108) become

$$\tilde{E}(\mathbf{r}; \omega) \Big|_{r \gg r'} \approx j\zeta k \frac{e^{-jkr}}{4\pi r} \oint_{S_0} e^{jk\hat{\mathbf{r}} \cdot \mathbf{r}'} \left[-\tilde{\mathbf{J}}_s^{eq} + \left(\tilde{\mathbf{J}}_s^{eq} \cdot \hat{\mathbf{r}} \right) \hat{\mathbf{r}} - \frac{1}{\zeta} \tilde{\mathbf{J}}_{ms}^{eq} \times \hat{\mathbf{r}} \right] dS', \quad (1.3.109)$$

$$\tilde{H}(\mathbf{r}; \omega) \Big|_{r \gg r'} \approx j \frac{k}{\zeta} \frac{e^{-jkr}}{4\pi r} \oint_{S_0} e^{jk\hat{\mathbf{r}} \cdot \mathbf{r}'} \left[-\tilde{\mathbf{J}}_{ms}^{eq} + \left(\tilde{\mathbf{J}}_{ms}^{eq} \cdot \hat{\mathbf{r}} \right) \hat{\mathbf{r}} + \zeta \tilde{\mathbf{J}}_s^{eq} \times \hat{\mathbf{r}} \right] dS'. \quad (1.3.110)$$

1.3.3 Radiation pattern

With (1.3.109-1.3.110), we can now derive the far fields pattern. As the computations are done considering the Cartesian components of the currents $\tilde{\mathbf{J}}$ and $\tilde{\mathbf{J}}_m$, or $\tilde{\mathbf{J}}_s^{eq}$

and $\tilde{\mathbf{J}}_{ms}^{eq}$ in the vector N2F, and the Cartesian components of the unit vector $\hat{\mathbf{R}} \underset{r \gg r'}{\approx} \hat{\mathbf{r}}$, the resulting far fields detectors $\tilde{\mathbf{E}}^*$ and $\tilde{\mathbf{H}}^*$ are in Cartesian components : $\tilde{\mathbf{E}}_x^*, \tilde{\mathbf{E}}_y^*, \tilde{\mathbf{E}}_z^*$ and $\tilde{\mathbf{H}}_x^*, \tilde{\mathbf{H}}_y^*, \tilde{\mathbf{H}}_z^*$. To simplify the pattern computations, these can be converted into spherical components¹⁷ and discard the radial components $\tilde{\mathbf{E}}_r^*$ and $\tilde{\mathbf{H}}_r^*$ which must be null in the far zones. Furthermore, the plane wave behavior of the electromagnetic fields in the far zones, that is

$$\tilde{\mathbf{H}}^* = \frac{1}{\zeta} \hat{\mathbf{r}} \times \tilde{\mathbf{E}}^*, \quad (1.3.111)$$

allows us to keep either the electric field or the magnetic field to derive the pattern of the radiating structure. We have chosen to keep the electric far field detectors $\tilde{\mathbf{E}}_\theta^*$ and $\tilde{\mathbf{E}}_\phi^*$ from which the gain can be obtained in term of θ and ϕ polarizations by the following expressions [3, 7]

$$\mathcal{P}_\theta(\hat{\mathbf{r}}; \omega) = \lim_{r \rightarrow \infty} 4\pi r^2 \frac{S_{r[\theta]}}{P_r} = 4\pi \frac{|\tilde{\mathbf{E}}_\theta^*|^2}{2\zeta P_r} = 2\pi \frac{|\tilde{\mathbf{E}}_\theta^*|^2}{\zeta P_r}, \quad (1.3.112)$$

$$\mathcal{P}_\phi(\hat{\mathbf{r}}; \omega) = \lim_{r \rightarrow \infty} 4\pi r^2 \frac{S_{r[\phi]}}{P_r} = 4\pi \frac{|\tilde{\mathbf{E}}_\phi^*|^2}{2\zeta P_r} = 2\pi \frac{|\tilde{\mathbf{E}}_\phi^*|^2}{\zeta P_r}, \quad (1.3.113)$$

where $S_{r[\theta]}$ and $S_{r[\phi]}$ are the active power densities related to each of the polarizations¹⁸. The term P_r is the radiated power that, for practical reasons, has to be computed from the fields on the bounding surface. In effect, we could compute the total power using the far fields detectors, selecting the appropriate number of look angles to cover a sphere, but this is excessively time consuming. The computation of the power radiated from the near fields is achieved by an integration of the flux of the Poynting vector and keeping half of the real part. In other terms

$$\begin{aligned} P_r &= \frac{1}{2} \Re \left\{ \oint_{S_0} \mathbf{S}_r(\mathbf{r}'; \omega) \cdot \hat{\mathbf{n}} \, dS' \right\} \\ &= \frac{1}{2} \Re \left\{ \oint_{S_0} [\tilde{\mathbf{E}}(\mathbf{r}'; \omega) \times \tilde{\mathbf{H}}^\dagger(\mathbf{r}'; \omega)] \cdot \hat{\mathbf{n}} \, dS' \right\} \end{aligned} \quad (1.3.114)$$

¹⁷ $\mathbf{A}_r = \mathbf{A}_x \sin(\theta) \cos(\phi) + \mathbf{A}_y \sin(\theta) \sin(\phi) + \mathbf{A}_z \cos(\theta)$, $\mathbf{A}_\theta = \mathbf{A}_x \cos(\theta) \cos(\phi) + \mathbf{A}_y \cos(\theta) \sin(\phi) - \mathbf{A}_z \sin(\theta)$ and $\mathbf{A}_\phi = -\mathbf{A}_x \sin(\phi) + \mathbf{A}_y \cos(\phi)$. [1]

¹⁸ Real part of the radial component of the *Poynting vector*, the first due to θ -polarized electric field and the second due to ϕ -polarized electric field.

where the symbol \dagger indicates the complex conjugate. The total pattern, polarization independent, is given by

$$\mathcal{P}(\hat{\mathbf{r}}; \omega) = \mathcal{P}_\theta(\hat{\mathbf{r}}; \omega) + \mathcal{P}_\phi(\hat{\mathbf{r}}; \omega). \quad (1.3.115)$$

1.3.4 Numerical results

We proceed with the numerical implementation that computes the vector N2F on the array depicted in figure 1.21, comparing it to results obtained with FEKO. All the surface integrals have been computed by means of numerical midpoint integrations for each vector component separately, in a similar manner as it was done for scalar fields in section 1.2 (see note 12). Figure 1.22 shows the power density on the box surface computed by our implementation. Notice that, as the sources are not radiating isotropically but mainly along the $\hat{\mathbf{z}}$ direction, the level of the fields on the lateral faces of the box is low when compared to those generated by point sources (figure 1.16). In order to compare our implementation results to FEKO's ones, the frequency of the sources has been set to 1 GHz in both simulation environments. Also, the electric currents are set to be of 1 [A] and the magnetic currents are of $\zeta_0 \approx 376.73$ [V]. The FEKO model of the array analyzed is depicted in figure 1.23.

The patterns on the XZ and YZ cut planes computed with FEKO are shown in figures 1.24 and 1.25. Both of them are the total fields directivity patterns (no polarization splitting) and they have a maximum value of 16.474 [dBi] on the broadside direction. The total power radiated by the array, for FEKO, is of $1.3346 \cdot 10^5$ [W], while our implementation gives $1.33528 \cdot 10^5$ [W] with $\lambda/10$ of sampling resolution on the box, that is -0.051 % of relative error. Notice that errors in the power radiated computation can vary sensibly to the maximum gain, but not the pattern shape. The total pattern achieved with our implementation is depicted in figure 1.26. The maximum gain achieved is of 16.481 [dBi], slightly higher than the one computed by FEKO, and this is mainly due to the misfit in the power radiated computation (coarse integration of the power density on the box). In effect, as we will see below, the error on the fields detectors have resulted to be very low. However, for practical applications, that error

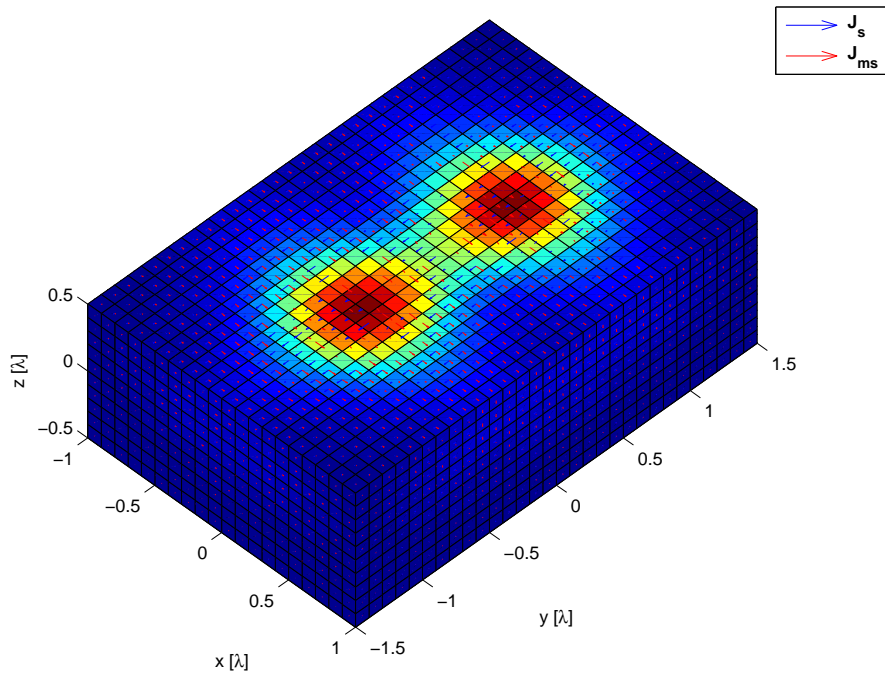


Figure 1.22: Surface power density and real part of the equivalent currents computed on the box of figure 1.21.

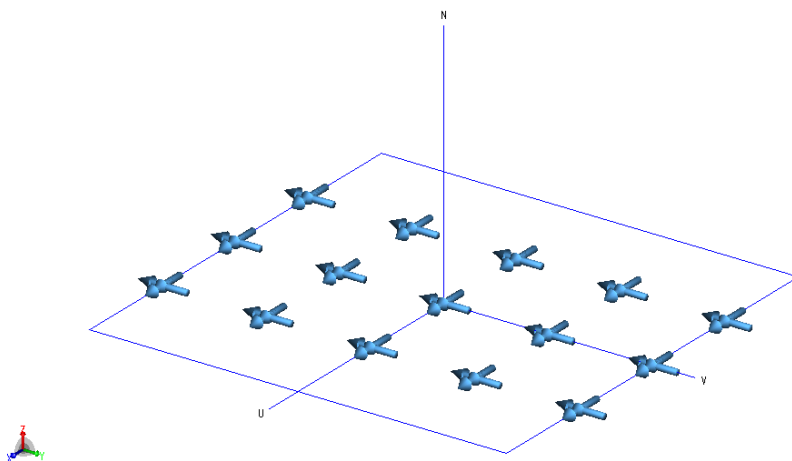


Figure 1.23: FEKO model of the 3 by 5 Huygens' sources array of figure 1.21.

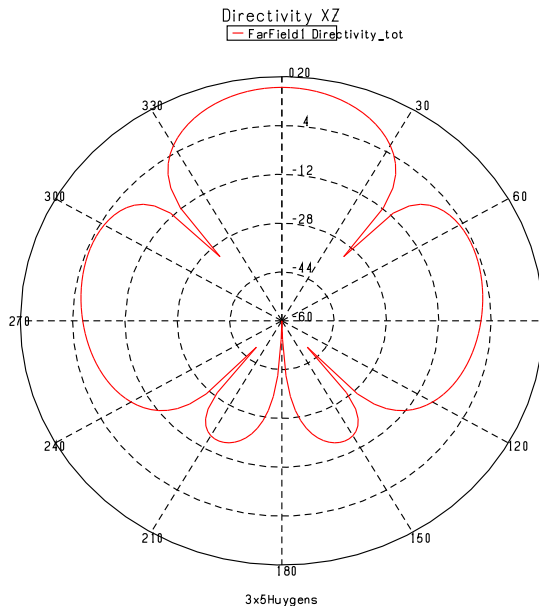


Figure 1.24: Pattern computed with FEKO on the $\phi = 0^\circ$ cut plane.

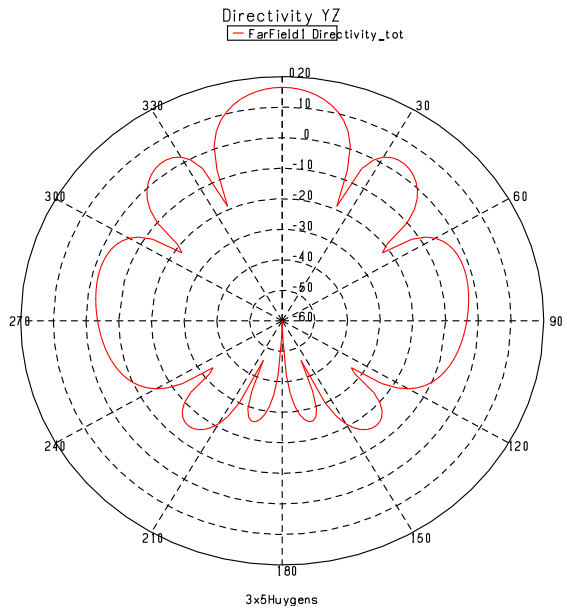


Figure 1.25: Pattern computed with FEKO on the $\phi = 90^\circ$ cut plane.

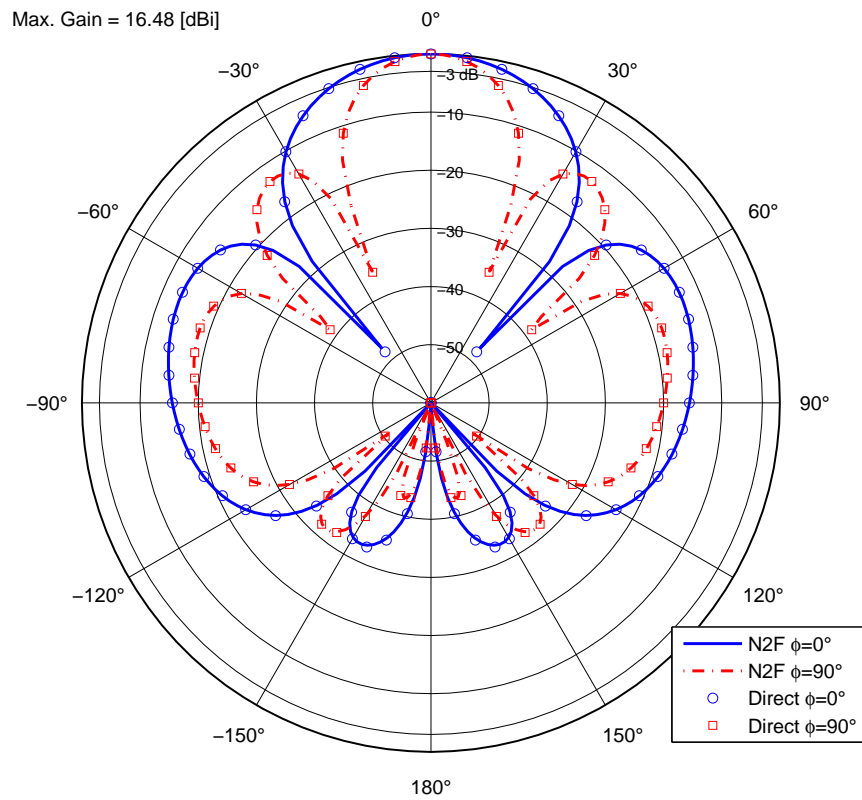


Figure 1.26: N2F and direct total fields patterns computed for the array of figure 1.22.

can be considered to be low enough and the pattern sufficiently accurate.

The pattern formulation has been split into θ and ϕ polarizations, and this allows us to evaluate the cross-polarizations behavior of real antennas. Plots of $\mathcal{P}_\theta(\hat{\mathbf{r}}; \omega)$ and $\mathcal{P}_\phi(\hat{\mathbf{r}}; \omega)$ are given in figures 1.27 and 1.28.

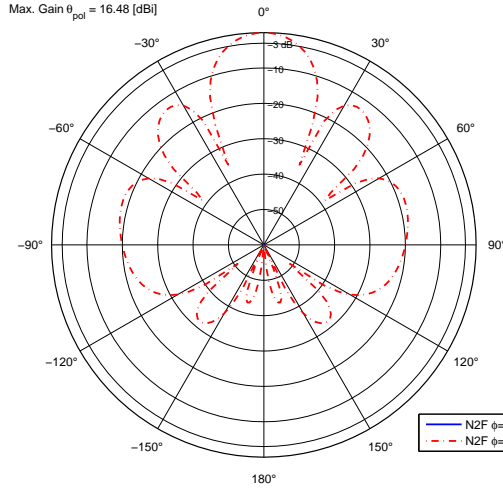


Figure 1.27: θ polarization pattern $\mathcal{P}_\theta(\hat{\mathbf{r}}; \omega)$ of the 3 by 5 Huygens sources array.

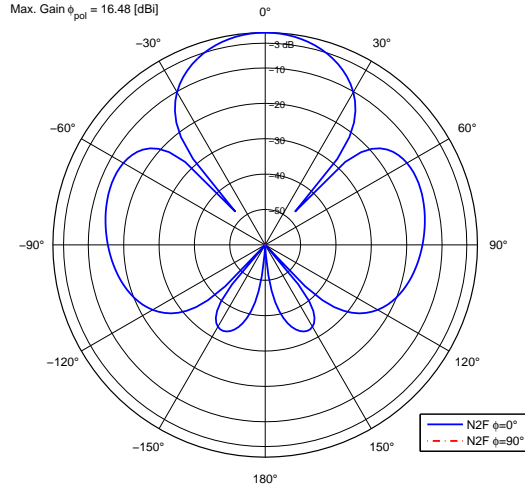


Figure 1.28: ϕ polarization pattern $\mathcal{P}_\phi(\hat{\mathbf{r}}; \omega)$ of the 3 by 5 Huygens sources array.

Let us now quantify the error between the patterns computed by N2F and direct processes, using the following relation, similarly to 1.2.96,

$$\epsilon_{[\text{Direct}-\text{N2F}]} = \frac{\left\| \left(\tilde{\mathbf{E}}_{\text{Direct}\theta}^* + \tilde{\mathbf{E}}_{\text{Direct}\phi}^* \right) - \left(\tilde{\mathbf{E}}_{\text{N2F}\theta}^* + \tilde{\mathbf{E}}_{\text{N2F}\phi}^* \right) \right\|_2}{\left\| \tilde{\mathbf{E}}_{\text{Direct}\theta}^* + \tilde{\mathbf{E}}_{\text{Direct}\phi}^* \right\|_2}. \quad (1.3.116)$$

The FEKO results have been compared first to those of the direct computation using (1.3.116). The error in this case is of $\epsilon_{[\text{Direct}-\text{FEKO}]} = 1.487 \cdot 10^{-4}$, which significantly validates our implementation. Then, comparing them to the N2F results, we have $\epsilon_{[\text{N2F } [\lambda/10]-\text{FEKO}]} = 1.821 \cdot 10^{-3}$. Finally, as we expected, the error committed in the N2F computation with $\lambda/10$ sampling resolution on the box, relatively to the direct computation, is of $\epsilon_{[\text{Direct}-\text{N2F } [\lambda/10]]} = \epsilon_{[\lambda/10]} = 1.842 \cdot 10^{-3}$, similar to $\epsilon_{[\text{N2F } [\lambda/10]-\text{FEKO}]}$ as $\epsilon_{[\text{Direct}-\text{FEKO}]}$ is of an order below. Also, notice that the N2F error is of the same order that one computed for scalar field in section 1.2.2.2 ($2.398 \cdot 10^{-3}$). Figure 1.29 shows the same

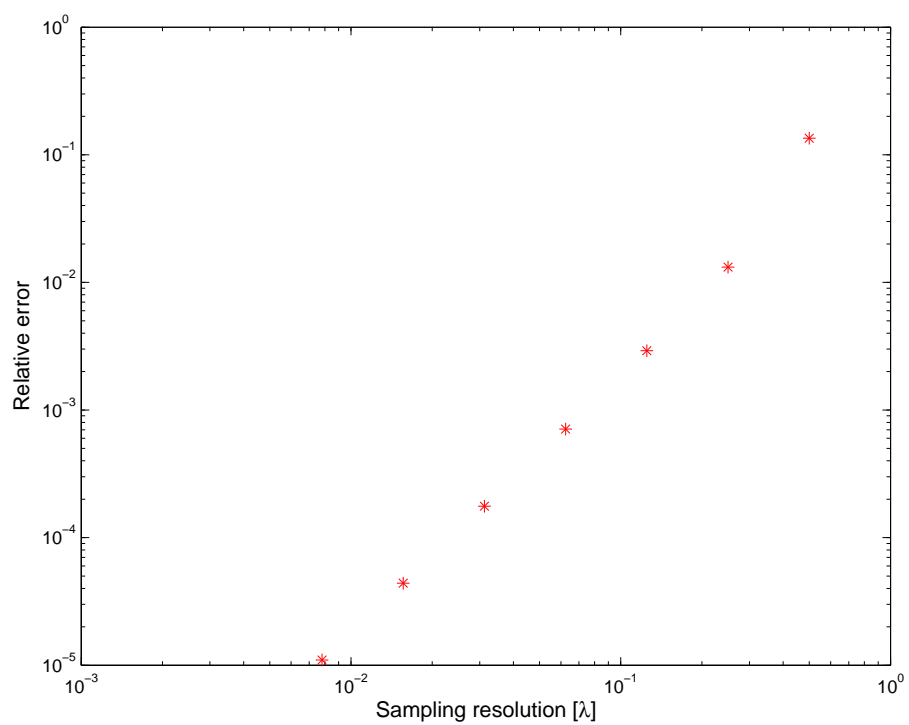


Figure 1.29: Relative error between N2F and direct far fields detectors for several sampling resolutions.

convergence behavior of the vector N2F, analogously to the scalar N2F (1.15), while increasing the sampling resolution.

LOW-RANK APPROXIMATIONS FOR FIELDS TRANSFORMATIONS

In this chapter we present the approximation techniques that have been applied on the scalar near field and on the scalar near field to far field process, in order to find suitable spanning spaces for the beamsteering operation. We recall that what we are seeking for is an adequate approximation method, with controllable accuracy, in order to apply it to a full FEM model of a phased array.

We will first begin with a *Singular Value Decomposition* (SVD) based technique that will be applied on the near fields in order to define the possible number of unknowns of a reduced model. Then a *polynomial interpolation* and a *Discrete Fourier Transform* (DFT) based technique, the *DFT-truncation*, will be tested on the near field to far field operator, seeking for basis functions to express the N2F process. The accuracy of these techniques will be given in terms of error induced to the pattern, relatively to the non approximated N2F pattern and to the directly computed pattern.

2.1 Approximations of the near fields

To introduce the SVD, we first discuss on the *Proper Orthogonal Decomposition* (POD), for which the SVD is the discrete case. The POD is a powerful and elegant method of data analysis aimed of obtaining low-dimensional approximate descriptions of high dimensional processes. The POD is often used to extract *mode shapes* or basis functions, from experimental data or detailed simulations of high-dimensional systems, for subsequent use in *Petrov-Galerkin projections* [13] that yield low dimensional dynamical models [14].

2.1.1 Proper orthogonal decomposition

Let $z(\mathbf{r}) \in \mathbb{C}$ be a function of the position vector $\mathbf{r} \in \mathbb{R}^3$ over the domain of interest $S \subset \mathbb{R}^3$. Now, suppose we wish to approximate the function $z(\mathbf{r})$ as a finite sum

$$z(\mathbf{r}) = \sum_{m=1}^M a_m \phi_m(\mathbf{r}), \quad a_m, \phi_m(\mathbf{r}) \in \mathbb{C}, \quad (2.1.1)$$

with the reasonable expectation that the approximation becomes exact in the limit as $M \rightarrow \infty$, except possibly on a set of measure zero [15]. The representation (2.1.1) of the function $z(\mathbf{r})$ is not unique. If the domain of \mathbf{r} is a bounded interval S , then the functions $\phi_m(\mathbf{r})$ can be chosen as a Fourier series, or Legendre polynomials, or Chebyshev polynomials, and so on. For each such choice of a sequence $\phi_m(\mathbf{r})$ that forms a basis for some suitable class of functions $z(\mathbf{r})$, assuming these functions bounded and integrable, the sequence of coefficients¹ a_m is different. The POD is concerned with one possible choice of the functions $\phi_m(\mathbf{r})$. If we have chosen orthonormal basis functions, i.e.

$$\oint_S \phi_m^\dagger(\mathbf{r}') \phi_n(\mathbf{r}') dS' = \delta_{mn}, \quad (2.1.2)$$

where $\delta_{mn} = 1$ if $m = n$, 0 otherwise is the *Kronecker's delta*, then

$$a_m = \oint_S \phi_m^\dagger(\mathbf{r}') z(\mathbf{r}') dS', \quad (2.1.3)$$

¹ We have supposed our function $z(\mathbf{r})$ to be time independent, as we are interested in the approximation of fields in a frequency domain formulation. However, if we had $z(\mathbf{r}, t)$ with t the time variable, the coefficients a_m would become functions $a_m(t)$ to hold the time dependence.

that is the coefficient a_m depends only on the related function $\phi_m(\mathbf{r}')$ and not on the others. By the integral (2.1.3), the function $z(\mathbf{r}')$ is said to be *tested* by the function $\phi_m(\mathbf{r}')$, operation after which we derive a *weighting* coefficient a_m of $\phi_m(\mathbf{r}')$ for the approximating sum (2.1.1). The sum (2.1.1) is the POD of $z(\mathbf{r})$ if the orthonormal functions are ordered such that the best approximant $\phi_m(\mathbf{r})$ of $z(\mathbf{r})$ have lower indices, that is, as M grows $\rightarrow \infty$, the series (2.1.1) converges monotonically to $z(\mathbf{r})$ in a *least squares sense* (\mathcal{L}^2 norm error),

2.1.2 Singular value decomposition

As said before, the SVD is the discrete case of the POD. We proceed with the definition of the SVD. [20, 21]

Definition 1 Consider $\mathbf{A} \in \mathbb{C}^{m \times n}$, $m \geq n$. The triple factorization $\mathbf{A} =: \mathbf{U}\mathbf{\Sigma}\mathbf{V}^H$, \mathbf{V}^H being the conjugate transpose \mathbf{V} , is called *singular value decomposition* (in the reduced form) of \mathbf{A} if $\mathbf{U} \in \mathbb{C}^{m \times n}$, $\mathbf{V} \in \mathbb{C}^{n \times n}$, $\mathbf{\Sigma} \in \mathbb{R}^{n \times n}$ are such that $\mathbf{U}^H \mathbf{U} = \mathbf{V}^H \mathbf{V} = \mathbf{V} \mathbf{V}^H = \mathbf{I}_n$, \mathbf{I}_n being the identity matrix, and $\mathbf{\Sigma} = \text{diag}(\sigma_1, \dots, \sigma_n)$.

The matrix \mathbf{U} consists of n orthonormal eigenvectors associated with the n largest eigenvalues of $\mathbf{A}\mathbf{A}^H$, and the matrix \mathbf{V} consists of the orthonormal eigenvectors of $\mathbf{A}^H \mathbf{A}$. The columns of \mathbf{U} are called the *left singular vectors*, the columns of \mathbf{V} are called the *right singular vectors*. The diagonal elements of $\mathbf{\Sigma}$ are the *nonnegative square roots* of the eigenvalues of $\mathbf{A}^H \mathbf{A}$ and they are called *singular values*. We shall assume that $\sigma_1 \geq \sigma_2 \geq \dots \geq \sigma_n \geq 0$. Thus if $\text{rank}(\mathbf{A}) = r$, $\sigma_{r+1} = \sigma_{r+2} = \dots = \sigma_n = 0$. In other terms,

$$\begin{aligned} \mathbf{U} &= [\mathbf{U}_1 \mathbf{U}_2], \quad \mathbf{\Sigma} = \begin{pmatrix} \mathbf{\Sigma}_1 & \mathbf{0} \\ \mathbf{0} & \mathbf{\Sigma}_2 \end{pmatrix} \in \mathbb{R}^{n \times n}, \quad \mathbf{V} = [\mathbf{V}_1 \mathbf{V}_2] \\ \mathbf{\Sigma}_1 &= \begin{pmatrix} \sigma_1 & & \\ & \ddots & \\ & & \sigma_r \end{pmatrix}, \quad \mathbf{\Sigma}_2 = \mathbf{0} \in \mathbb{R}^{n-r \times n-r} \\ \mathbf{U}_1 &\in \mathbb{C}^{m \times r}, \mathbf{U}_2 = \mathbf{0} \in \mathbb{C}^{m \times n-r}, \quad \mathbf{V}_1 \in \mathbb{C}^{r \times n}, \mathbf{V}_2 = \mathbf{0} \in \mathbb{C}^{n-r \times n} \end{aligned}$$

As a consequence of definition 1, the following relations on four fundamental spaces of \mathbf{A} hold

$$\begin{aligned}\text{colsp}\{\mathbf{A}\} &= \text{colsp}\{\mathbf{U}_1\}, \\ \text{colsp}\{\mathbf{A}^H\} &= \text{colsp}\{\mathbf{V}_1\}, \\ \ker\{\mathbf{A}\} &= \text{colsp}\{\mathbf{V}_2\}, \\ \ker\{\mathbf{A}^H\} &= \text{colsp}\{\mathbf{U}_2\}.\end{aligned}\tag{2.1.4}$$

where *colsp* is the space spanned by the column vectors of a matrix, that is the *range*, and *ker* is the *kernel* or *null space* of a matrix. [20]

By analogy with the POD previously presented, the left singular vectors \mathbf{U} correspond to the orthonormal basis functions $\phi_m(\mathbf{r})$. These singular vectors actually constitute a space of *testing vectors* for matrices spanned by the same range of \mathbf{A} that provides the coefficients of an expansion in terms of vectors \mathbf{U} (the *trial* vectors which in this case are the same as the testing vectors). The coefficients a_m can be viewed as the testing matrix multiplication $\mathbf{U}^H\mathbf{A} = \mathbf{K}$, $\mathbf{K} \in \mathbb{C}^{m \times n}$ being a matrix of coefficients that weights the basis \mathbf{U} . In other terms, if $\text{rank}(\mathbf{A}) = r$ we can build a matrix $\mathbf{\Pi} = \mathbf{U}\mathbf{U}^H \in \mathbb{C}^{m \times m}$, an *orthogonal projection* [18] of any matrix onto the r dimensional subspace spanned by the columns of \mathbf{U} ($\text{colsp}\{\mathbf{A}\}$) and along the kernel of \mathbf{U}^H (left singular vectors associated to null singular values, that is $\ker\{\mathbf{A}^H\}$).

Another interesting issue of the SVD is the fact that the singular vectors are ordered in function of their importance in the representation of the matrix \mathbf{A} , the singular values being ordered monotonically in a decreasing order. We can thus select $q \leq r$ left singular vectors, associated to the first q singular values, to build a projector $\mathbf{\Pi}_q \in \mathbb{C}^{m \times m}$ and $\text{rank}(\mathbf{\Pi}_q) = q$ such that $\tilde{\mathbf{A}}_q = \mathbf{\Pi}_q\mathbf{A}$ is a q^{th} order *low-rank approximation* of the matrix \mathbf{A} , achieved by a projection technique. By analogy with the POD, q corresponds to the degree of approximation M . Furthermore, the following important theorem on the approximation holds [20]

Theorem 1 Let $\mathbf{A} \in \mathbb{C}^{m \times n}$, $m \geq n$ be a matrix with singular value decomposition $\mathbf{U}\mathbf{\Sigma}\mathbf{V}^H$. For any $q : 0 \leq q \leq r$, $\mathbf{A}_q = \sum_{j=1}^q \sigma_j \mathbf{u}_j \mathbf{v}_j^\dagger$, $\mathbf{u}_j, \mathbf{v}_j$ column vectors. If $q =$

$\min(m, n) = \text{rank}(\mathbf{A}) = r, \sigma_{q+1} = 0$. Then

$$\|\mathbf{A} - \mathbf{A}_q\|_2 = \inf_{\substack{\mathbf{B} \in \mathbb{C}^{m \times n} \\ \text{rank}(\mathbf{B}) \leq q}} \|\mathbf{A} - \mathbf{B}\|_2 = \sigma_{q+1}.$$

Theorem 1 states that we can compute the error for the approximation and that the approximation is optimal with respect to the spectral norm².

2.1.3 Space spanned by the scanned near fields

Along a beamsteering process, the dimension of the *scan angle space* that can hold all the configurations of the near field is *a priori* unknown. The SVD comes out helping us to find it. We may first collect some *pictures* of the near field behavior for some scan angles (θ_x, θ_y) (see section 1.2.2.2) to build our space. In other words, the near fields sampled values for each n scan angle chosen will constitute spanning vectors ψ_n such that $\mathbf{A}_\theta = \text{span} \left\{ \bigcup_{n=1}^N \psi_n \right\}$. The rank will be checked performing an SVD on $\mathbf{A}_\theta = \mathbf{U}_\theta \Sigma_\theta \mathbf{V}_\theta^H$ and looking at the singular values to derive informations on the importance of the vectors collected. Relying on definition 1, the singular values of \mathbf{A}_θ become null as soon as the number of spanning vectors N supersedes the rank of the scan angle space, expressing in such a way its dimension.

The choice of the scan angles (θ_x, θ_y) is arbitrary, and we also don't know *a priori* which sequence may lead to a rapid convergence into the full rank scan angle space. In a first attempt, we choose the broadside direction, obtaining the vector $\psi_{(0^\circ, 0^\circ)}$. Then, limiting the scanning operation in the x direction, we select the end fire steering angle in that direction. Thus, we have the new spanning vector $\psi_{(90^\circ, 0^\circ)}$. The next vectors will be chosen in between of $(0^\circ, 0^\circ)$ and $(90^\circ, 0^\circ)$, halving iteratively the steering intervals inserting a new vector in the middle. We obtain the sequence $\psi_{(0^\circ, 0^\circ)}, \psi_{(90^\circ, 0^\circ)}, \psi_{(45^\circ, 0^\circ)}, \psi_{(22.5^\circ, 0^\circ)}, \psi_{(67.5^\circ, 0^\circ)}, \psi_{(11.25^\circ, 0^\circ)}, \dots$ and so on, until we achieve the sought full rank space. Notice that, considering the set of equally spaced scan angles, this is an exponential growth of the spanning space of the kind $\dim(\mathbf{A}_\theta) = \lfloor 2^{n-1} \rfloor + 1$, $n = 0, 1, 2, \dots$, and we will call this sequence *exponential scan angle selection*.

² Natural norm induced by the \mathcal{L}^2 norm : $\|\mathbf{A}\|_2 = \sup_{\|\mathbf{x}\|_2 \neq 0} \frac{\|\mathbf{A}\mathbf{x}\|_2}{\|\mathbf{x}\|_2}$.

As we are building the space increasing progressively the number of spanning vectors, we may test the basis completeness applying the projector resulting from the left singular vectors onto a picture of the near fields that is not contained in the vectors that spans \mathbf{A}_θ (otherwise we have exact approximation). We have arbitrarily chosen the scan angle $(23.3251^\circ, 0^\circ)$, and the fields are produced on an enclosing sphere by an array of 17 by 1 point sources (as we are scanning along θ_x , a linear array can be used to achieve faster computations), varying the spacing between the point sources. Figures 2.1-2.5 show the error (see chapter 1), while increasing the dimension of the spanning space, on the near field

$$\mathfrak{E}_{\text{Near } [\lambda/10] - \text{Near approx } [\lambda/10]} = \frac{\|\tilde{\psi}_{r'}^{\text{Near}} - \tilde{\psi}_{r'}^{\text{Near approx}}\|_2}{\|\tilde{\psi}_{r'}^{\text{Near}}\|_2},$$

the N2F far field detectors computed from the approximated and non approximated near fields

$$\mathfrak{E}_{\text{N2F } [\lambda/10] - \text{N2F approx } [\lambda/10]} = \frac{\|\tilde{\psi}_r^*{}^{\text{N2F}} - \tilde{\psi}_r^*{}^{\text{N2F approx}}\|_2}{\|\tilde{\psi}_r^*{}^{\text{N2F}}\|_2},$$

and, similarly, relatively to the direct far field

$$\mathfrak{E}_{\text{Direct} - \text{N2F approx } [\lambda/10]} = \frac{\|\tilde{\psi}_r^*{}^{\text{Direct}} - \tilde{\psi}_r^*{}^{\text{N2F approx}}\|_2}{\|\tilde{\psi}_r^*{}^{\text{Direct}}\|_2}.$$

Notice that, as we have chosen an exponential scan angles selection, the error is computed only once all the selected angles are equidistant in the beam steering range.

The limit in the spacing between the point sources, in order to avoid the insurgence of *grating lobes* [2], that is constructive directions of the far field different from the desired ones, is of $\approx 0.6 \lambda$. However, we have extended that range to illustrate the changes in the singular values. The direct far field relative error is inferiorly limited by the sampling resolution, chosen to be of $\lambda/10$. We can see that the singular values drop below two orders of magnitude over the double precision used ($\approx 10^{-16}$), and we will refer to this low level as the *numerical null threshold* [21], after the 17th singular value, that is the number of point sources disposed along x . However, the relative error in the pattern is not always null when spanning with 17 vectors. Thus, relying on definition 1, we conclude that:

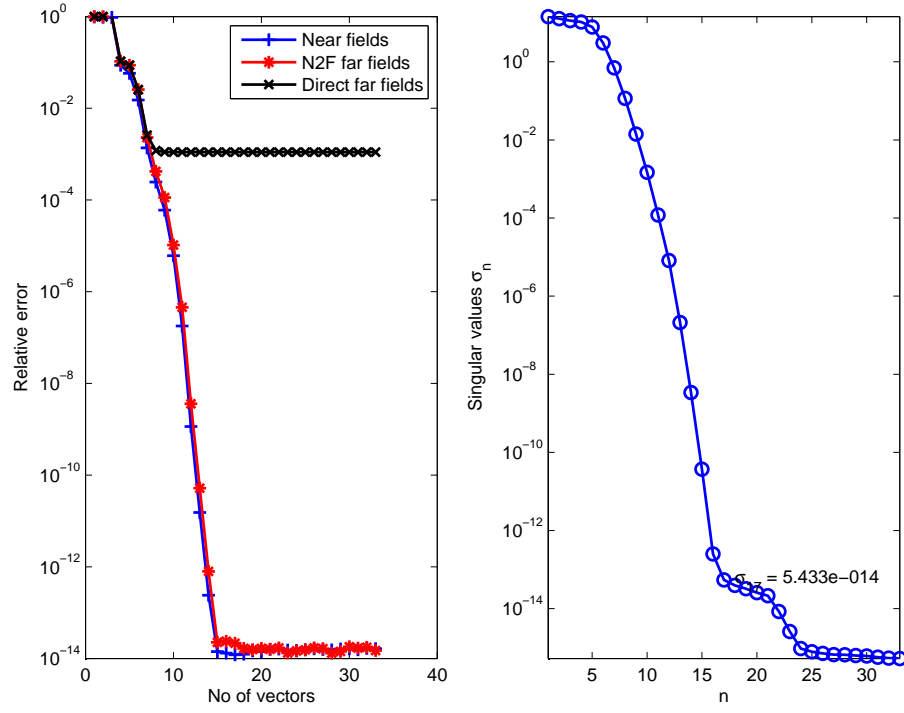


Figure 2.1: Error plot relative to the number of vectors $\Psi_{(\theta_x^\circ, 0^\circ)}$ used in the scan angle space (left) and singular values related to the scan angle space build with 33 vectors (right) for the chosen array of 17 by 1 point sources equally spaced of $\lambda/4$.

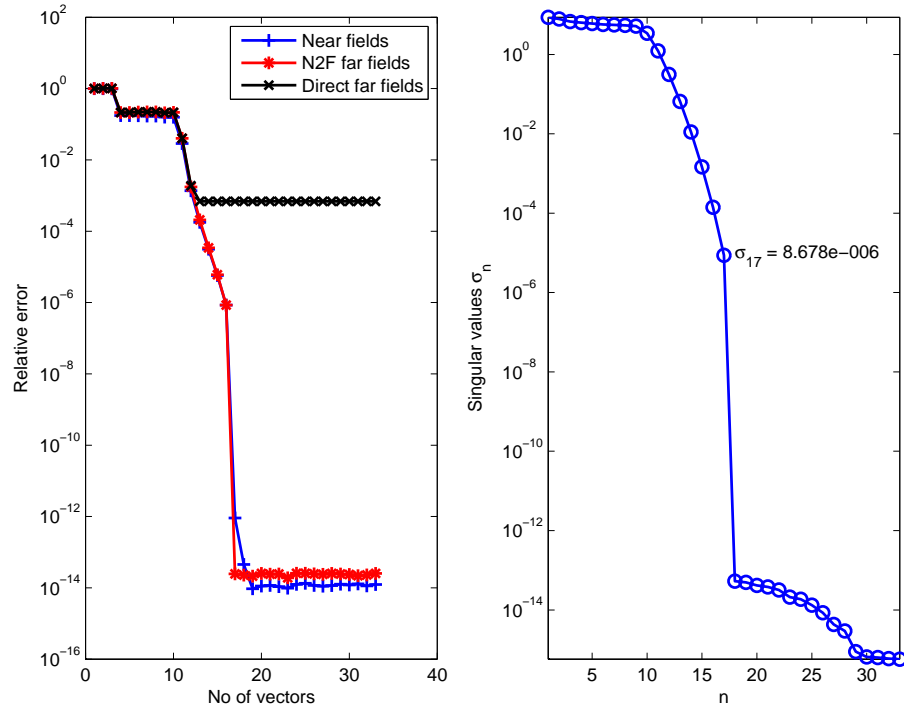


Figure 2.2: Error plot for the chosen array of 17 by 1 point sources equally spaced of $\lambda/2$.

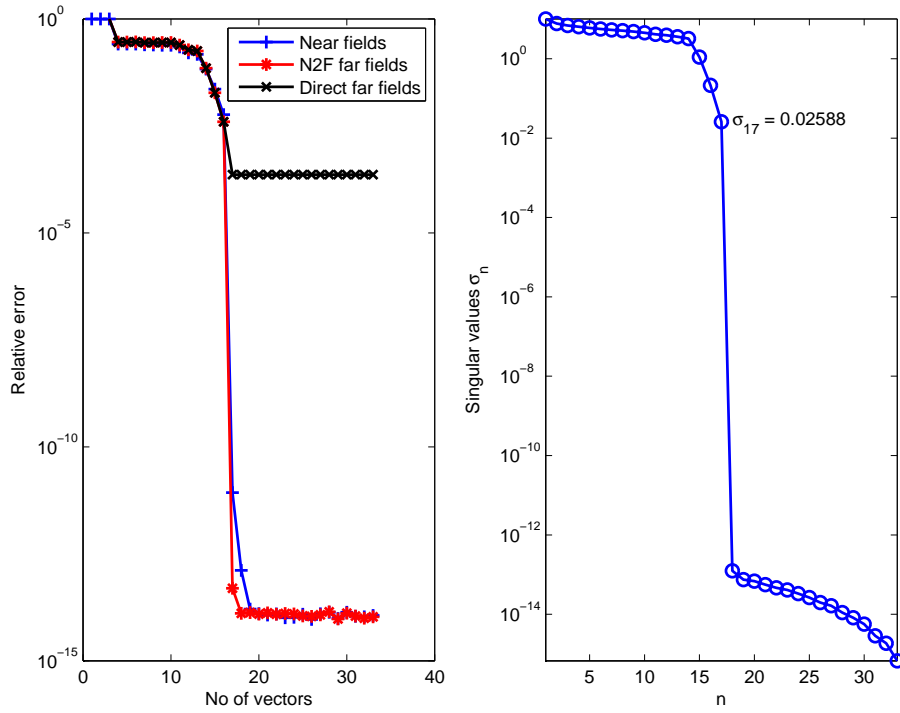


Figure 2.3: Error plot for the chosen array of 17 by 1 point sources equally spaced of $3\lambda/4$.

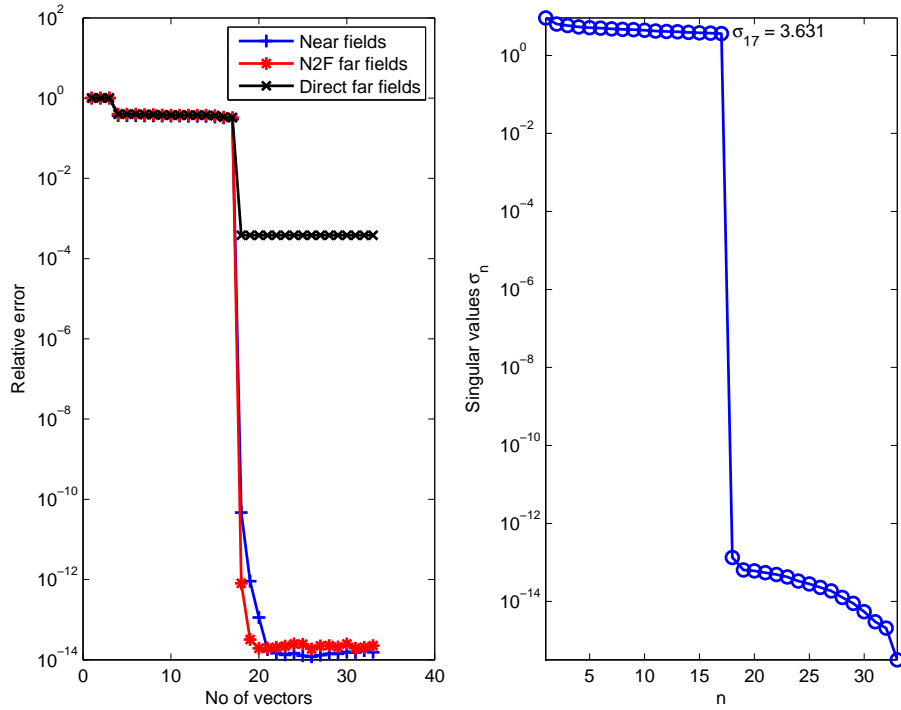


Figure 2.4: Error plot for the chosen array of 17 by 1 point sources equally spaced of λ .

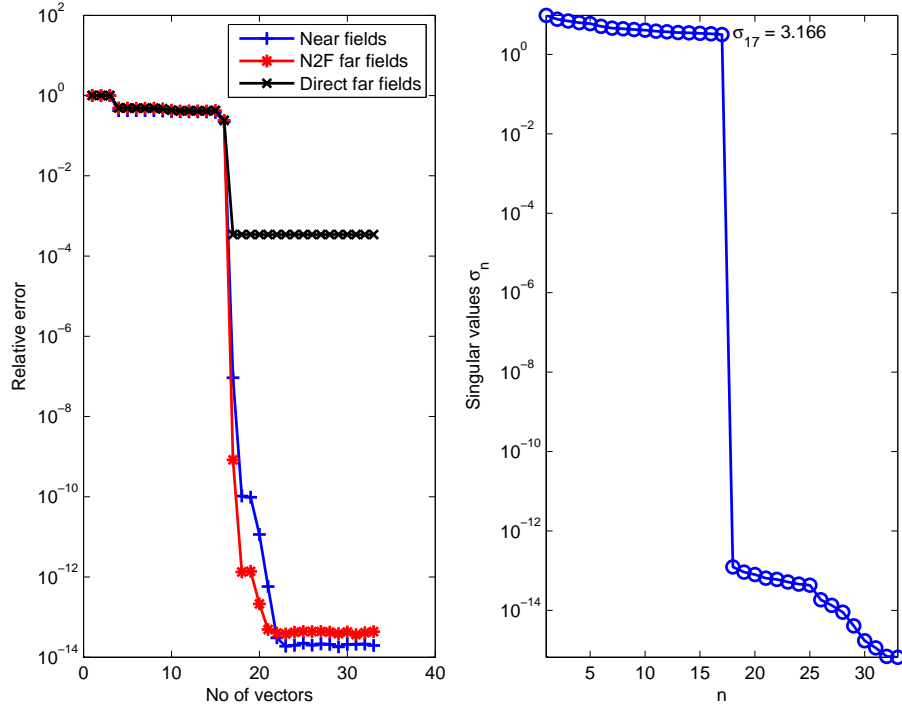


Figure 2.5: Error plot for the chosen array of 17 by 1 point sources equally spaced of $5 \lambda/4$.

Conclusion 1 *The numerical rank (the rank referred to the chosen numerical null threshold) of the scan angle space, resulting from a beamsteering operation along a single direction, equals the number of radiating elements along that direction. Furthermore, the error in the pattern computation depends on the relative spacing between the radiating elements, and within the range that avoids grating lobes, the error grows as the array becomes electrically larger.*

Figure 2.6 illustrates the state of the space spanned by 17 vectors, chosen in the same exponential manner, for a linear array of 17 point sources equally spaced of $\lambda/2$. We notice differences between the singular values related to the space spanned by 17 vectors and the one with 33 vectors (figure 2.2), even if $\mathbf{A}_\theta|_{17} = \text{span} \left\{ \bigcup_{n=1}^{17} \Psi_n \right\} \subset \mathbf{A}_\theta|_{33} = \text{span} \left\{ \bigcup_{n=1}^{33} \Psi_n \right\}$. To see how different are the basis on which the near field picture tested is projected, let us compare the performances of a low rank projector of dimension q , assuming $r = 17$ as the rank of the scan angle space, when the space built has 17 vectors, 33 vectors and 65 vectors, using the same exponential scan angle

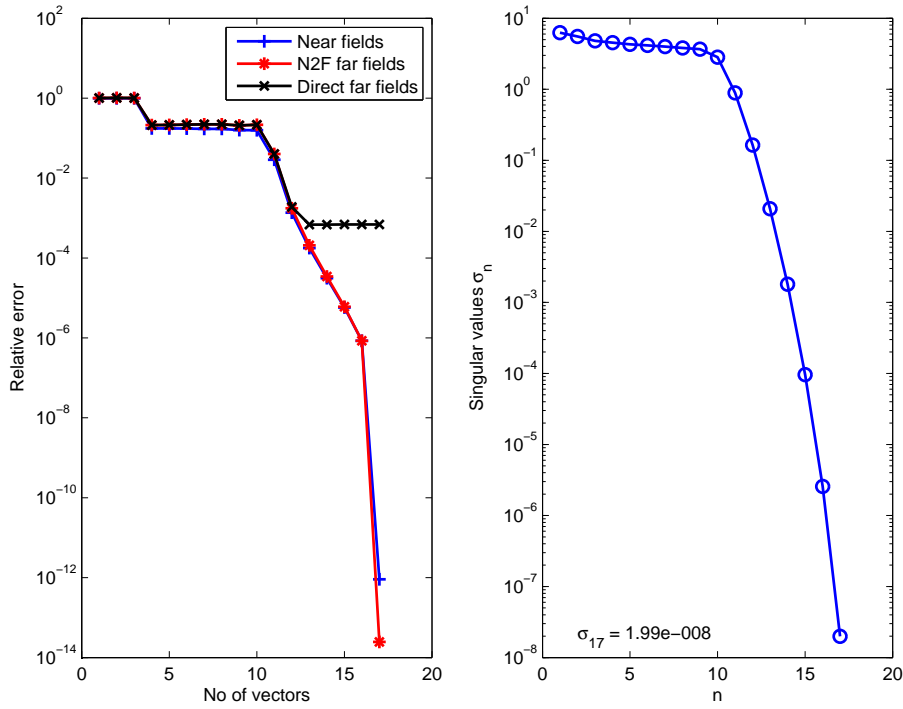


Figure 2.6: Error plot relative to the number of vectors $\psi_{(\theta_x^\circ, 0^\circ)}$ up to 17 (left) and singular values related to the scan angle space built with 17 vectors (right) for an array of 17 by 1 point sources equally spaced of $\lambda/2$.

	17 vectors		33 vectors		65 vectors	
q	n.f. error	f.f. error	n.f. error	f.f. error	n.f. error	f.f. error
17	$1.963 \cdot 10^{-12}$	$3.005 \cdot 10^{-13}$	$7.153 \cdot 10^{-14}$	$2.948 \cdot 10^{-13}$	$6.933 \cdot 10^{-14}$	$3.062 \cdot 10^{-13}$
16	$2.975 \cdot 10^{-06}$	$9.877 \cdot 10^{-06}$	$1.233 \cdot 10^{-07}$	$4.309 \cdot 10^{-07}$	$1.536 \cdot 10^{-06}$	$5.406 \cdot 10^{-06}$
15	$2.301 \cdot 10^{-05}$	$7.737 \cdot 10^{-05}$	$3.008 \cdot 10^{-05}$	0.0001065	$2.831 \cdot 10^{-05}$	0.0001012
14	0.0001395	0.0004772	0.0002284	0.0007944	0.0002965	0.001039
13	0.0007067	0.00248	0.001282	0.004903	0.001119	0.004345
12	0.001066	0.00343	0.013	0.04836	0.01246	0.0462
11	0.03508	0.1508	0.01581	0.07227	0.01728	0.07936
10	0.2715	1.104	0.2271	0.9225	0.2049	0.8253

Table 2.1: Error in the near fields (n.f.) approximation of order q and resulting N2F far fields (f.f.).

selection space such that $\mathbf{A}_\theta|_{17} = \text{span}\left\{\bigcup_{n=1}^{17} \psi_n\right\} \subset \mathbf{A}_\theta|_{33} = \text{span}\left\{\bigcup_{n=1}^{33} \psi_n\right\} \subset \mathbf{A}_\theta|_{65} = \text{span}\left\{\bigcup_{n=1}^{65} \psi_n\right\}$ and retaining the first 17 relevant left singular vectors to build the projector. Table 2.1 shows values of relative errors in the near field and in their N2F patterns. The order is slightly the same for all the cases. However, the space spanned by 17 vectors may allow an truncation order up to 12 vectors, where the N2F

error is below our accuracy criterion ($5 \cdot 10^{-3}$, see section 1.2.2.2), while the others would be limited to 13 vectors for the same criterion.

Conclusion 2 *Reduction of the order of the near field scan angle space can be applied, depending on the importance of the basis vectors selected, that is on the values of the singular values associated to the left singular vectors retained in the order reduction. Furthermore, no effective improvement is achieved with vectors obtained by a lower order projection based on a larger number of scan angles selected exponentially.*

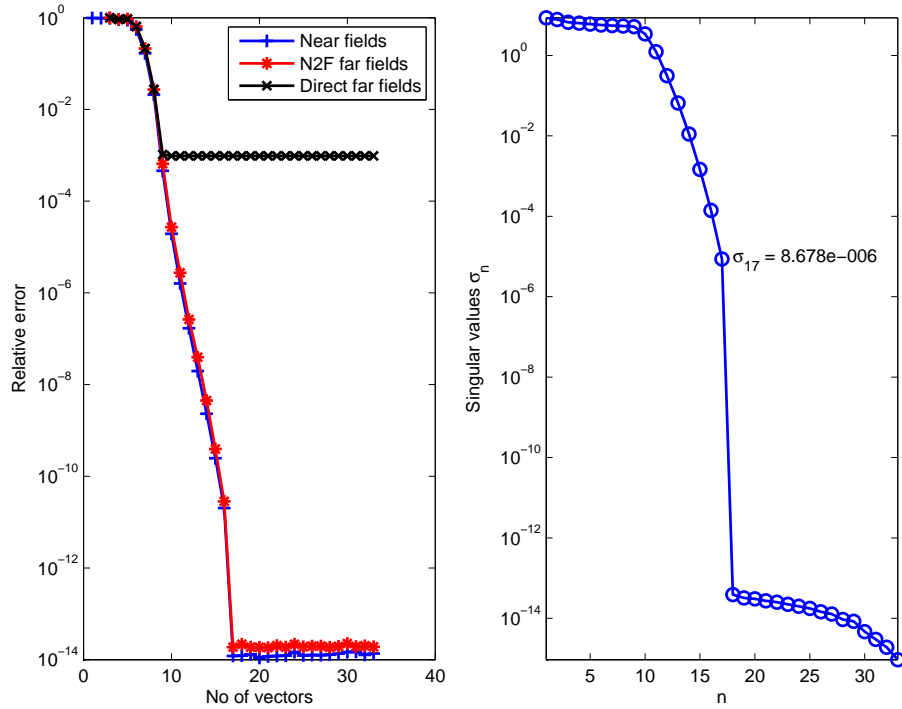


Figure 2.7: Error on the tested angle of 23.3251° and singular values for 33 vectors selected linearly with $\theta_x = 0^\circ \rightarrow 90^\circ$ (17 point sources linear array, spacing of $\lambda/2$).

To see whether the choice of the spanning angles is important while building \mathbf{A}_θ , let us try two other sequences: the linear sequences from $\theta_x = 0^\circ \rightarrow 90^\circ$ and *vice versa*, with a fixed $\Delta\theta_x$. We have chosen up to 33 vectors ($\Delta\theta_x = 2.8125^\circ$) and the resulting errors are shown in figures 2.7 and 2.8. In the first case, the tested angle of 23.3251° becomes included in the scan angle space interval $[0^\circ, 25.3125^\circ]$ with the 10th vector ($\Psi_{(25.3125^\circ, 0^\circ)}$), but the error begins its decreasing slope 5 vectors before, and the error becomes numerically null at the 17th vector (size of the array). In the second case,

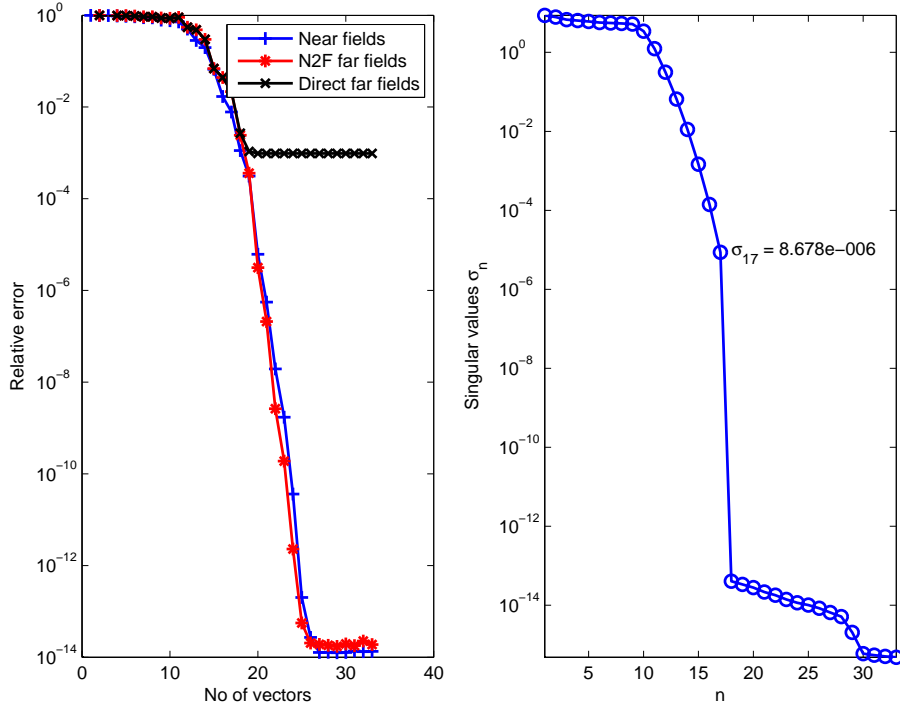


Figure 2.8: Error on the tested angle of 23.3251° and singular values for 33 vectors selected linearly with $\theta_x = 90^\circ \rightarrow 0^\circ$ (17 point sources linear array, spacing of $\lambda/2$).

we need to wait until the 25th vector ($\psi_{(22.5^\circ, 0^\circ)}$) to see the error dropping below the numerical noise floor ($< 10^{-13}$). The final 33 vectors, being the same in the two cases, are such that, obviously, we achieve the same singular values. Looking at figures 2.9

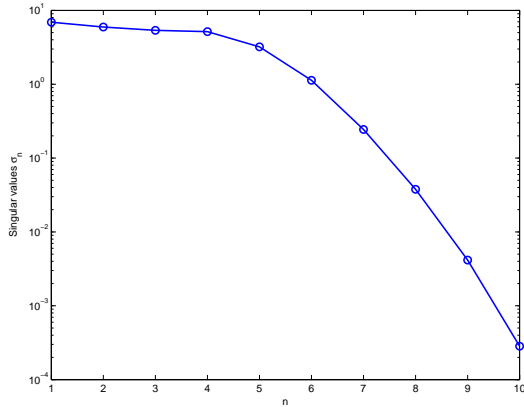


Figure 2.9: Singular values of the space spanned by 10 vectors in a linear selection of angles from $0^\circ \rightarrow 90^\circ$.

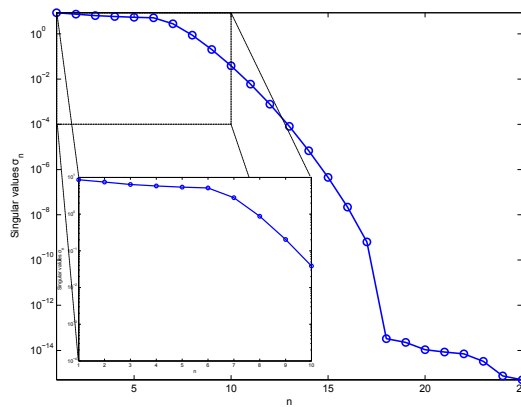


Figure 2.10: Singular values of the space spanned by 25 vectors in a linear selection of angles from $90^\circ \rightarrow 0^\circ$.

and 2.10, respectively, the singular values for the space spanned by only 10 vectors

with the first angles selection and those for the space spanned by 25 vectors with the inverse angles selection, we notice that the slope in the singular values begins slightly earlier in the first (about 2 vectors before). This confirms that

Conclusion 3 *The selected angles for the near field used in the scan angle space influences the convergence to the full space. Moreover, the projection of a near field picture on that space leads to high error values if the scan angle of the projected picture is not included in the range of the selected scan angles to span the space, independently on whether the number of column vectors has superseded the rank of the space.*

Let us now check how the error grows while slightly increasing the dimension of the array above 17 point sources and projecting the chosen test vector onto a space spanned by 17 vectors obtained with equally spaced scan angles by an exponential scan angle selection. In order to have the maximum error, the tested angle have been changed to 2.8125° , that is an angle in the middle of 0° and 5.625° for which we have collected the fields to span our scan angle space. The results are shown in figures 2.11 and 2.12.

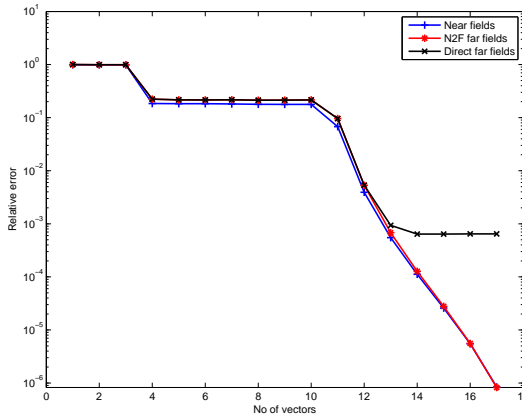


Figure 2.11: Error plot for an array of 18 point sources, spacing of $\lambda/2$.

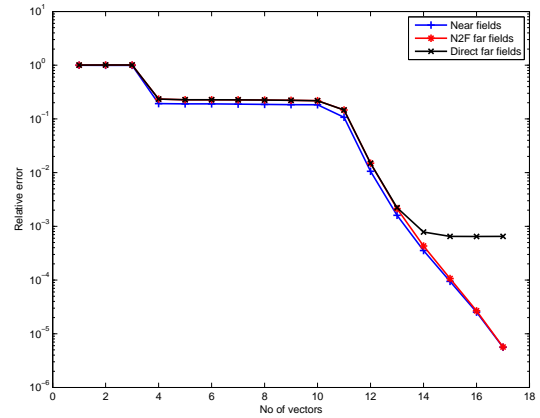


Figure 2.12: Error plot for an array of 19 point sources, spacing of $\lambda/2$.

The number of vectors that can be used as a basis for the fields produced by an array of 18 point sources, for the accuracy chosen of $5 \cdot 10^{-3}$, can be of 17. This is true for any test angle in the range $[0^\circ, 90^\circ]$. In effect, several angles have been tested, remaining in the middle of two spanning angles for the basis. The pattern resulting

from a linear array of 21 point sources, steered at $\theta_x = 2.8125^\circ$ and projected onto a basis of 17 vectors built by an exponential scan angle selection is shown in figure 2.13. As the N2F error, being of 0.01984 (n.f. error = 0.01724), has superseded

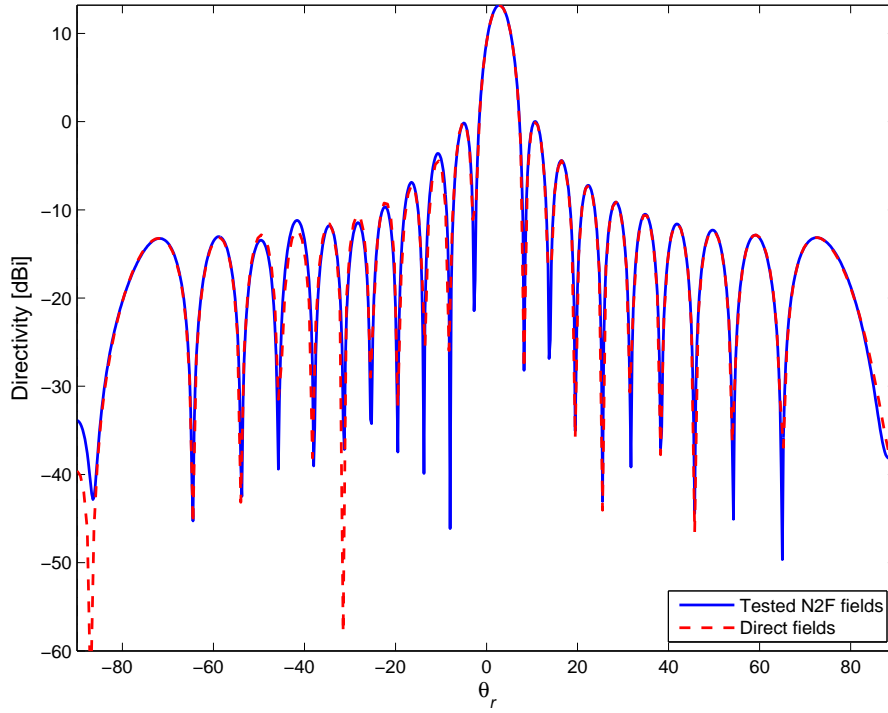


Figure 2.13: Pattern of the fields produced by a linear array of 21 point sources steered at 2.8125° and tested by a 17 vectors basis.

our accuracy threshold, we can see some misfits on the lateral lobes. However, for practical applications, this can be acceptable. Now testing the pattern steered at $5 \cdot 2.8125^\circ = 14.0625^\circ$ (figure 2.14), we obtain a N2F error of $1.55 \cdot 10^{-3}$ (n.f. error = $1.342 \cdot 10^{-3}$). Then for $11 \cdot 2.8125^\circ = 30.9375^\circ$ (figure 2.15) and for $21 \cdot 2.8125^\circ = 59.0625^\circ$ (figure 2.16) we have, respectively, the errors $5.48 \cdot 10^{-5}$ (n.f. error = $5.042 \cdot 10^{-5}$) and $1.92 \cdot 10^{-7}$ (n.f. error = $2.82 \cdot 10^{-7}$).

We can conclude that, as the near field approximations are more accurate the nearest the tested angle is from the end fire direction (see figure 2.17),

Conclusion 4 *The near field produced by a beamsteering operation around the broad side direction require a higher order basis than the field resulting from a beamsteering close to the end fire direction.*

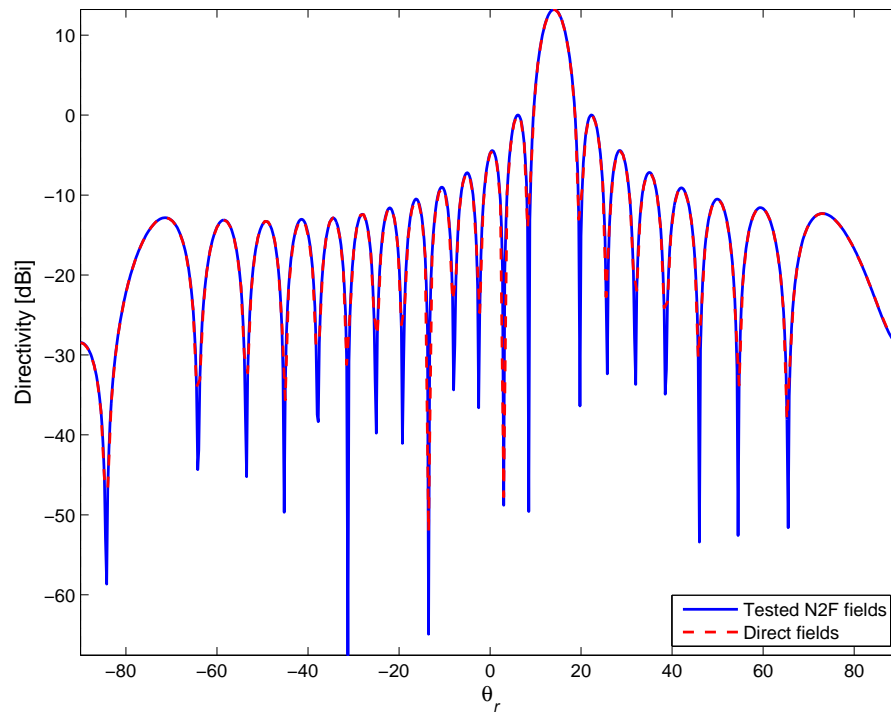


Figure 2.14: Pattern of the fields produced by a linear array of 21 point sources steered at 14.0625° and tested by a 17 vectors basis.

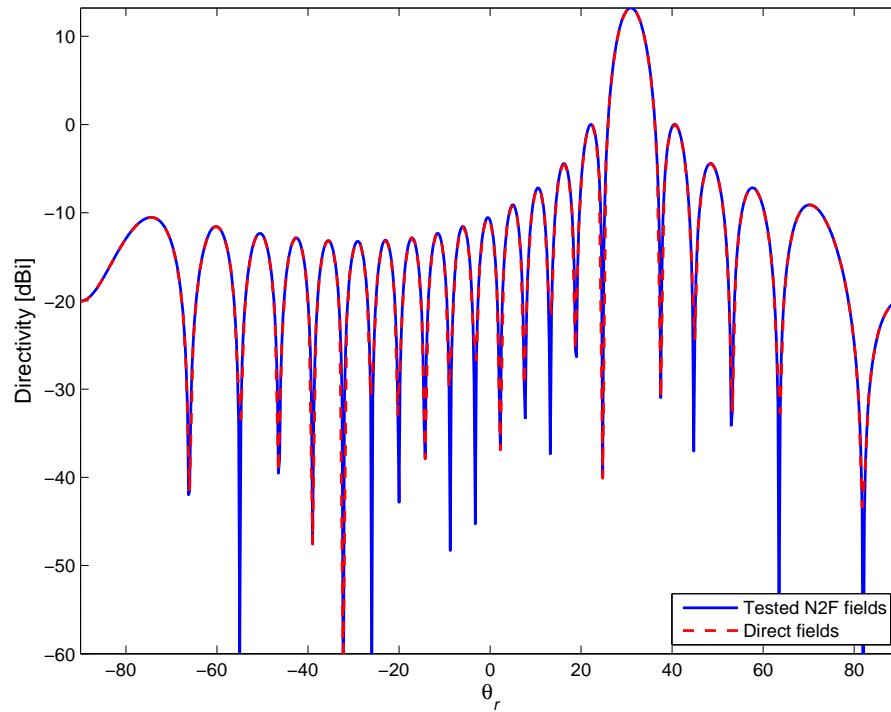


Figure 2.15: Pattern of the fields produced by a linear array of 21 point sources steered at 30.9375° and tested by a 17 vectors basis.

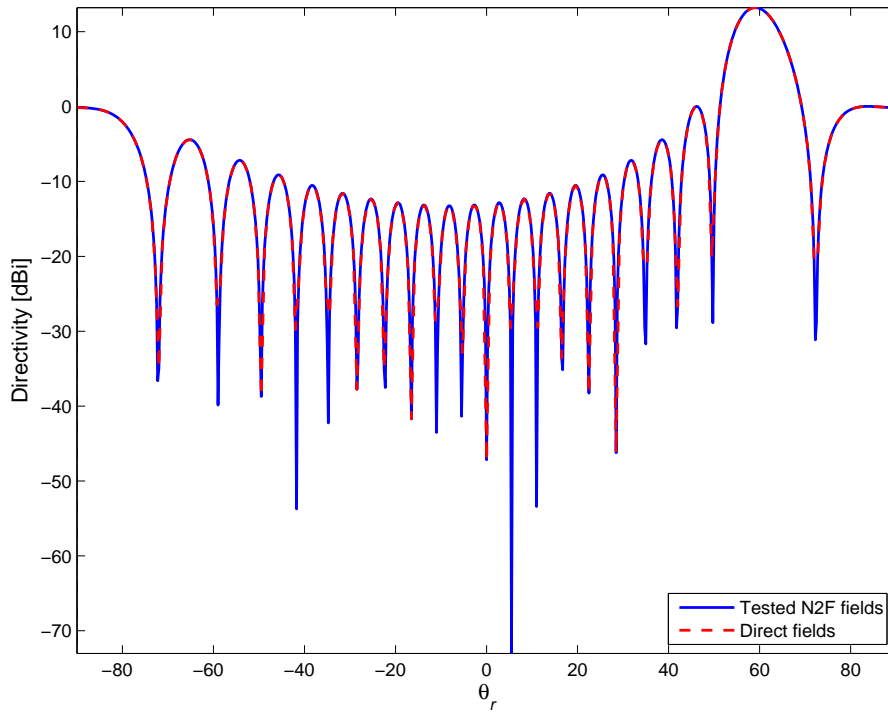


Figure 2.16: Pattern of the fields produced by a linear array of 21 point sources steered at 59.0625° and tested by a 17 vectors basis.

Thus, we can choose the spanning vectors with higher density of the scanned angles around the broad side direction in order to achieve a constant error (in the average) along the whole scanning range (see figure 2.18).

Seeking for further improvements in the space selection, we have performed transformations on the near fields pictures before we collect them for \mathbf{A}_θ . Exploiting the fact that the near field is sampled on a sphere, we have rotated the field around the y axis to let the scan direction go back to the broadside direction.

The results with rotated field are shown in figure 2.21. In figure 2.22 it is shown the results from a rotation in the direction in which the near field is maximal. For this case, it is necessary, in order to have the computed maximal direction to be around the scan angle, to increase the size of the bounding sphere, such that the constructive interference becomes visibly in the scan angle direction (the behavior in the near field is quite different from the one in the far field).

As we can see, no improvement is achieved in this manner. Even the rank of the

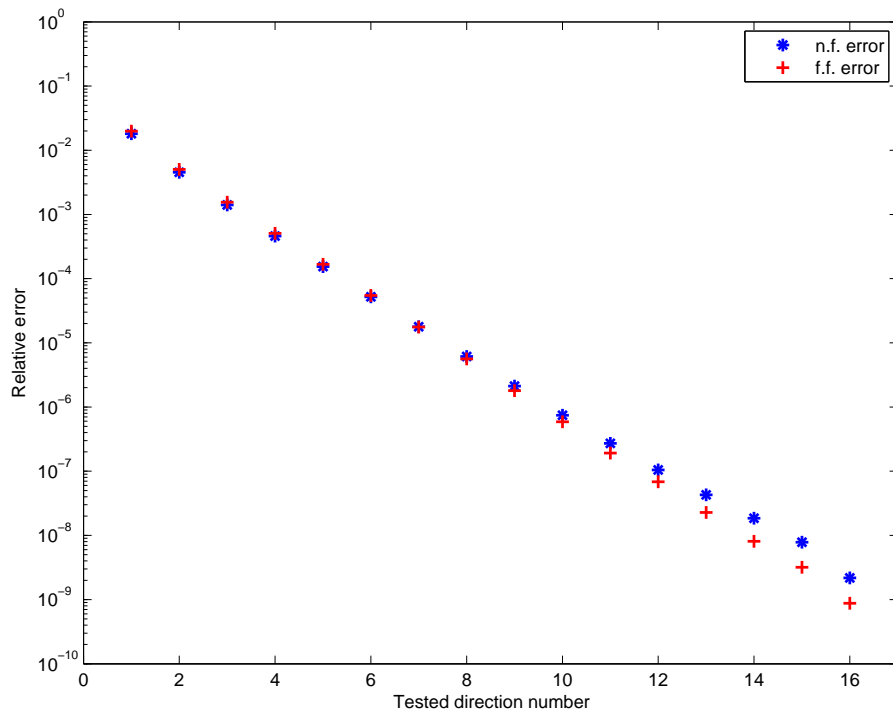


Figure 2.17: Near fields error and N2F error resulting from testing fields scanned in the middle of 17 exponentially selected scan angle spanning vectors for an array of 21 point sources.

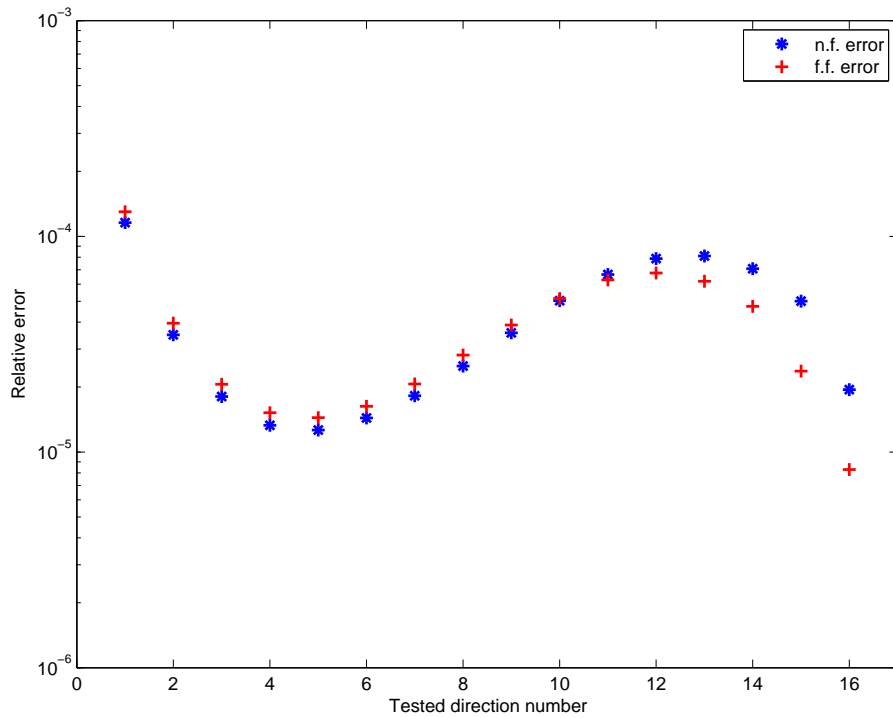


Figure 2.18: Possible correction applied to the selected angles for the spanning space. The gap between the angles is chosen to grow exponentially with base ≈ 1.1 .

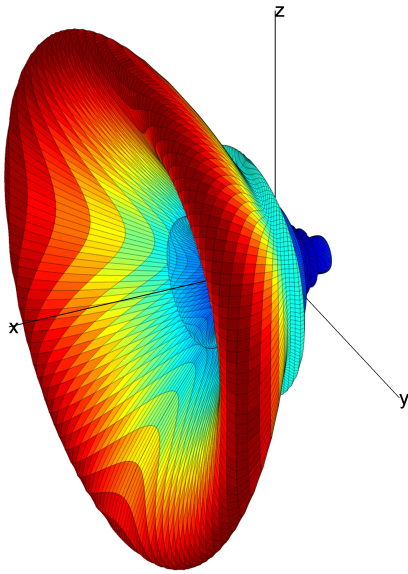


Figure 2.19: Near fields solid $|\psi|$ generated by a linear array of 9 point sources on the x direction steered at 30° .

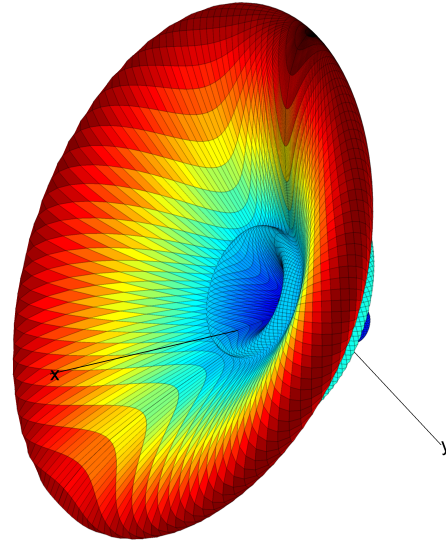


Figure 2.20: Near fields solid $|\psi|$ generated by a linear array of 9 point sources on the x direction steered at 30° rotated 30° backward.

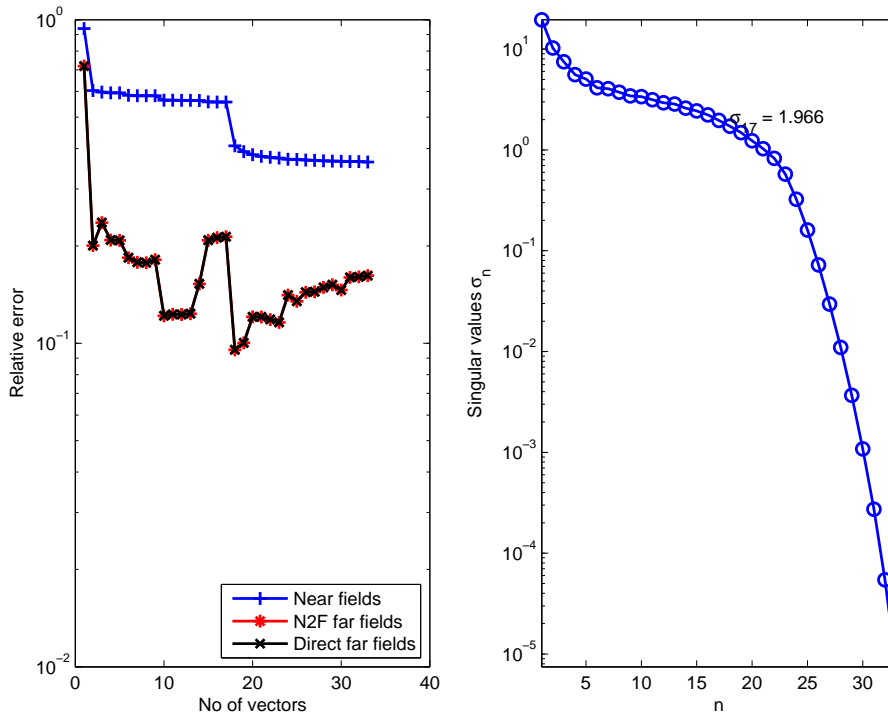


Figure 2.21: Error plot for the space spanned by fields rotated to broadside of the scan angle (linear array of 17 point sources).

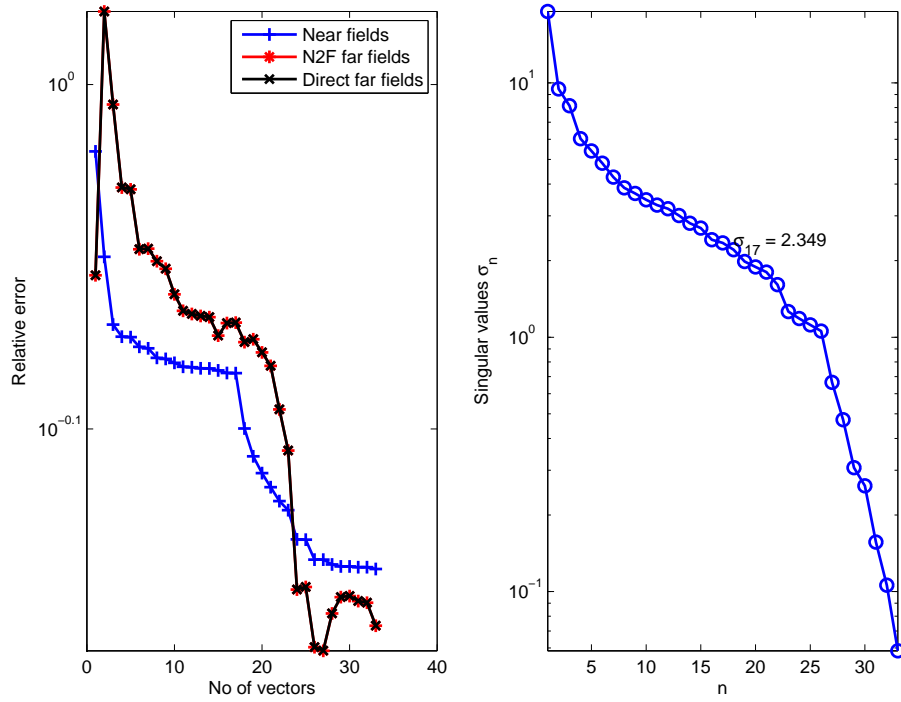


Figure 2.22: Error plot for the space spanned by fields rotated such that the maximum fields value goes to broadside (linear array of 17 point sources).

space is no more discernible, that is the spanning vectors are still very linearly dependent one from each other, thus cannot constitute a basis for the space sought.

2.2 Approximations of the near field to far field operator

The far field detectors presented in chapter 1 can be thought as the result of operators [16, 17] acting on the near field. In the scalar case, we can think of two (integral) operators, the first acting on the scalar near field and the second on its derivative³. In the vector case, six operators act on the components of the equivalent currents or, with some changes in the operators, of the near fields. In this section, we will treat only the scalar field to find an interpolation technique for the N2F operator. How-

³ In section 1.2.2.2, the derivatives were computed analytically in order to reduce the numerical errors that would be introduced by a numerical finite-differences-based derivation technique. However, we could have left the radial derivative to be part of the operator, leading into an integro-differential operator.

ever, the techniques that will be presented can be straightforwardly applied to vector fields. The far field detector of equation (1.2.87) become, in such an interpretation,

$$\begin{aligned}\tilde{\psi}_r^*(\hat{\mathbf{r}}; \omega) &= \mathcal{L}_\psi(\tilde{\psi}(\mathbf{r}'; \omega); \hat{\mathbf{r}}) + \mathcal{L}_{\psi'}\left(\frac{\partial \tilde{\psi}(\mathbf{r}'; \omega)}{\partial r'}; \hat{\mathbf{r}}\right) \\ &= \mathcal{L}\left(\tilde{\psi}(\mathbf{r}'; \omega), \frac{\partial \tilde{\psi}(\mathbf{r}'; \omega)}{\partial r'}; \hat{\mathbf{r}}\right),\end{aligned}\quad (2.2.5)$$

where \mathcal{L} is a linear⁴ functional parameterized in the look angle direction $\hat{\mathbf{r}} \in \mathcal{D} \subset \mathbb{R}^3$. In a first approach, we will restrain the look angle domain $\hat{\mathbf{r}} \in \mathcal{D}_{\phi=0^\circ} \subset \mathcal{D}$, seeking for an approximation of $\mathcal{L}(\hat{\mathbf{r}})$ along the pattern cut plane XZ ($\phi = 0^\circ$).

The main idea of the interpolation techniques presented below is to construct basis functions with a large informations content in order to reduce the number of basis coefficients needed to reach a certain level of accuracy in the outputs of interest.

2.2.1 Polynomial interpolation of the N2F operator

Given $\hat{\mathbf{r}} \in \mathcal{D}_{\phi=0^\circ}$, we first introduce parameter samples $\mathbf{s}_p \equiv \{\hat{\mathbf{r}}_1, \dots, \hat{\mathbf{r}}_P\}$, that is the chosen look angles for pattern plotting, and associated *operator snapshots* $\mathbf{L}_p = \text{colsp}\{\lambda_p \equiv \mathcal{L}(\hat{\mathbf{r}}_p), 1 \leq p \leq P\}$. The column vector of far field detectors $\boldsymbol{\psi}_r^*$ is given by the matrix vector product

$$\boldsymbol{\psi}_r^* = \mathbf{L}_p^T \boldsymbol{\psi}'' \quad (2.2.6)$$

where $\boldsymbol{\psi}'' = [\boldsymbol{\psi}; \boldsymbol{\psi}']$ is the column vector of vertically concatenated near field picture and its radial derivative, and \mathbf{L}_p^T is the transposed matrix of \mathbf{L}_p . Numerically speaking, \mathbf{L}_p is constructed modifying (1.2.94) in such a way that the summation becomes performed by the matrix multiplication (2.2.6). Thus we compute the values of the column vectors of \mathbf{L}_p by the following

$$\begin{aligned}\mathbf{L}_p &= \left[jk(\hat{\mathbf{r}}_p \cdot \hat{\mathbf{r}}'_m) e^{jk\hat{\mathbf{r}}_p \cdot \mathbf{r}'_m} \Delta S_m; -e^{jk\hat{\mathbf{r}}_p \cdot \mathbf{r}'_m} \Delta S_m \right], \\ m &= 1 \dots M, \quad p = 1 \dots P\end{aligned}\quad (2.2.7)$$

⁴ The surfaces enclosing the sources can be more than one, and the far field detector results in the sum of the application of the operator on each surface.

and the concatenated vectors of the field and its radial derivative are

$$\boldsymbol{\psi}'' = \left[\tilde{\psi}_m(\mathbf{r}'_m; \omega); \frac{\partial \tilde{\psi}_m(\mathbf{r}'_m; \omega)}{\partial r'_m} \right], \quad m = 1 \dots M. \quad (2.2.8)$$

Looking first at the singular values computed from the factorization of \mathbf{L}_P (figure 2.23) built for a sphere bounding a linear array of 5 point sources (radius of $3\lambda/2$), we see that the number of basis that may be required, at least for an approximation by projection, is about 48. This number is sensibly high, as we seek for a method that

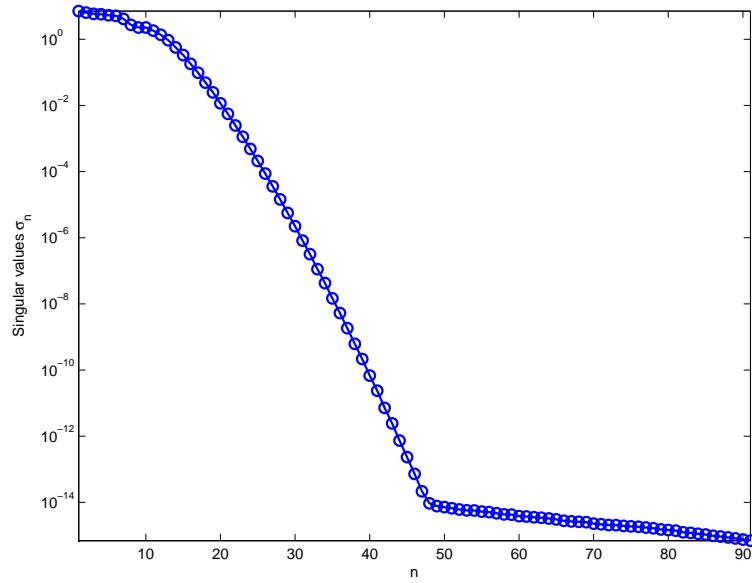


Figure 2.23: Singular values associated to the SVD of \mathbf{L}_P .

would be able to handle very large arrays (50 by 50 radiating elements and more). Thus, we proceed with a polynomial interpolation with the attempt to need less basis.

We introduce nested parameter samples $\mathbf{s}_Q \equiv \{\hat{\mathbf{r}}_1, \dots, \hat{\mathbf{r}}_Q\}$ and associated approximation spaces $\mathbf{L}_Q = \text{colsp} \{ \lambda_q \equiv \mathcal{L}(\hat{\mathbf{r}}_q), 1 \leq q \leq Q \}$ for $Q = 1, \dots, P$. Now, we evaluate $\mathcal{L}(\hat{\mathbf{r}})$ by the following sum

$$\hat{\mathcal{L}}(\hat{\mathbf{r}}) = \sum_{q=1}^Q \Theta_q(\hat{\mathbf{r}}) \mathcal{L}(\hat{\mathbf{r}}_q), \quad (2.2.9)$$

where $\Theta_q(\hat{\mathbf{r}})$ is a set of Q polynomial basis functions with compact supports $\mathcal{Q}_q \subset \mathcal{D}_{\phi=0^\circ}$ such that $\Theta_m(\hat{\mathbf{r}}_m) \Theta_n(\hat{\mathbf{r}}_n) = 0$ if $m \neq n$, $\forall m, n = 1, \dots, Q$. The affinity of \mathcal{L} in $\hat{\mathbf{r}}$, that is a polynomial dependence in the parameter, is a fundamental requisite in order

to apply the model order reduction. We actually seek for the best way to express this affinity.

Using *piece-wise linear* basis functions (1st order), we assume \mathbf{L}_Q to be our interpolating nodes, and their influence is limited to the domain $\mathcal{Q}_q \in (\hat{\mathbf{r}}_{q-1}, \hat{\mathbf{r}}_{q+1})$ through *roof-top* shape functions as depicted in figure 2.24. For each node q , the roof-top

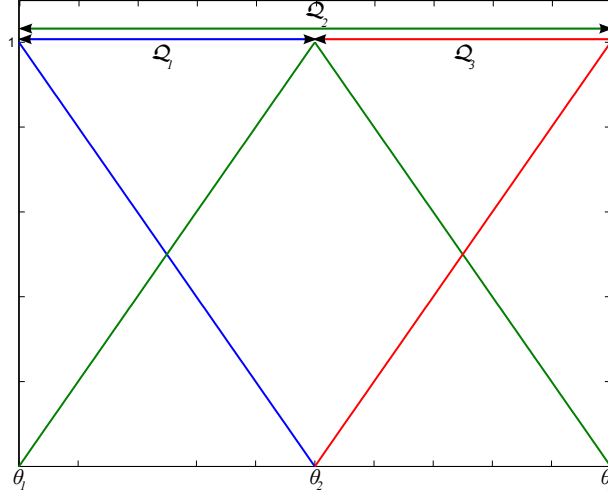


Figure 2.24: *Roof-top* interpolating functions for the first 3 nodes.

function can be defined as, being $\hat{\mathbf{r}} = \hat{\mathbf{r}}(\theta, \phi = 0^\circ) = \hat{\mathbf{r}}(\theta)$

$$\Theta_q(\hat{\mathbf{r}}) = \begin{cases} \frac{\theta - \theta_{q-1}}{\theta_q - \theta_{q-1}}, & \hat{\mathbf{r}}(\theta_{q-1}) \in \mathcal{D}_{\phi=0^\circ}, \hat{\mathbf{r}}(\theta) \in \mathcal{Q}_q, \\ \frac{\theta_{q+1} - \theta}{\theta_{q+1} - \theta_q}, & \hat{\mathbf{r}}(\theta_{q+1}) \in \mathcal{D}_{\phi=0^\circ}, \hat{\mathbf{r}}(\theta) \in \mathcal{Q}_q, \\ 0 & \text{otherwise.} \end{cases} \quad (2.2.10)$$

Numerically speaking, we can build the interpolated operator selecting first in the range of P look angles, Q of them equally spaced one from each other, building the matrix \mathbf{L}_Q of Q columns. Then we build the matrix $\mathbf{O}_Q \in \mathbb{R}^{P \times Q}$, which column vectors are the weighting values given by the roof-top functions. Finally, the product of these matrices gives

$$\tilde{\mathbf{L}}_P = \mathbf{L}_Q \mathbf{O}_Q^T \approx \mathbf{L}_P. \quad (2.2.11)$$

Now, we can compute $\Psi_r^* \Big|_{1^{\text{st}}} = \tilde{\mathbf{L}}_P^T \Psi$ and compare it to (2.2.6) in order to quantify the error introduced by the approximation of the operator. Figure 2.25 shows the errors

in the far field detectors relatively to the full non approximated ones and to the direct far field ones. The \mathbf{L}_p have been constructed with an average⁵ 1000 look angles in the range of $\theta \in [-90^\circ, 90^\circ]$, for a sphere of radius $3\lambda/2$ bounding a linear array of 5 point sources equally spaced of $\lambda/2$, with $\lambda/10$ of sampling resolution ($\epsilon_{\text{Direct-N2F}[\lambda/10]} = 2.68 \cdot 10^{-3}$). We notice that we need about 130 snapshots in order to introduce an error

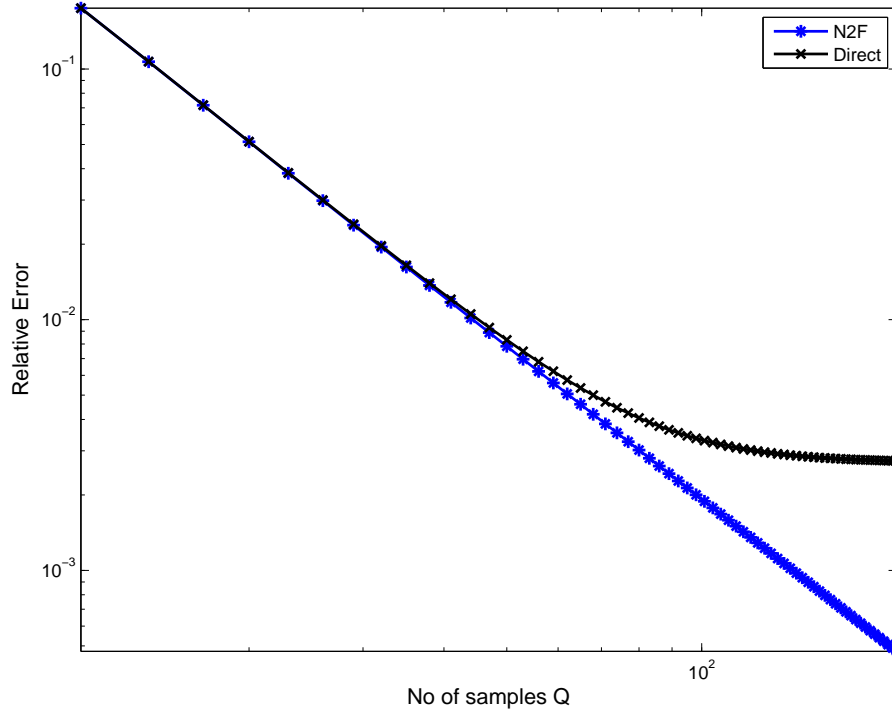


Figure 2.25: N2F error introduced with the *roof-top* interpolating functions.

below 10^{-3} , such that the approximated operator appears to be non-influent on the far fields computation.

As the pattern is in general a rapidly varying (many orders of magnitude between constructive and destructive interferences) function of the look angle dependent on the number of array elements, many snapshots would be needed to approximate accurately an array with more than 5 elements. We would need a higher slope in the errors as the number of snapshots increases, that is a quick convergence of the approximation into the exact operator. The finite element technique, also based on compact basis functions to approximate a global function, teaches us that we may

⁵ As we require the basis look angles to be equally spaced, the full operator dimension result to be proportional to the number of look angles sampled.

expect faster convergence with higher order polynomials [28]. Thus, we proceed introducing the 2nd order *Lagrange polynomials* as depicted in figure 2.26. The basis of

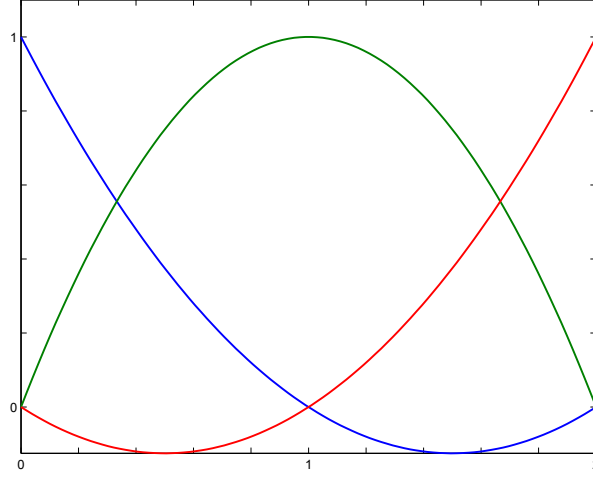


Figure 2.26: 2nd order interpolating polynomials for the first 3 nodes.

the first element (group of 3 nodes for quadratic basis functions) are expressed as,

$$\begin{aligned} \Theta_1(\hat{\mathbf{r}}) &= \begin{cases} (1-\xi)(2(1-\xi)-1), & \xi = \frac{\theta_3-\theta}{\theta_3-\theta_1}, \theta \in [\theta_1, \theta_3] \\ 0 & \text{elsewhere} \end{cases} \\ \Theta_2(\hat{\mathbf{r}}) &= \begin{cases} 4(1-\xi)(\xi), & \xi = \frac{\theta_3-\theta}{\theta_3-\theta_1}, \theta \in [\theta_1, \theta_3] \\ 0 & \text{elsewhere} \end{cases} \\ \Theta_3(\hat{\mathbf{r}}) &= \begin{cases} \xi(2\xi-1), & \xi = \frac{\theta_3-\theta}{\theta_3-\theta_1}, \theta \in [\theta_1, \theta_3] \\ 0 & \text{elsewhere} \end{cases} \end{aligned} \quad (2.2.12)$$

The sequence is then repeated for $q = 4, 5$ and 6 with the new range of $\theta \in [\theta_4, \theta_6]$ and $\frac{\theta_6-\theta}{\theta_6-\theta_4}$, and so on for $q > 6$. We proceed building the approximated operator, and compute the far fields detectors $\Psi_r^* \Big|_{2^{\text{nd}}}$. The sampled look angles define the full operator look angles, in order to preserve equal spacing between the interpolation angles. The error convergence plot is shown in figure 2.27. We can see that we get below 10^{-3} with only about 50 snapshots, compared to the ≈ 130 required by the roof-top approximation. For 200 snapshots, we notice that we achieve an error one order of magnitude lower.

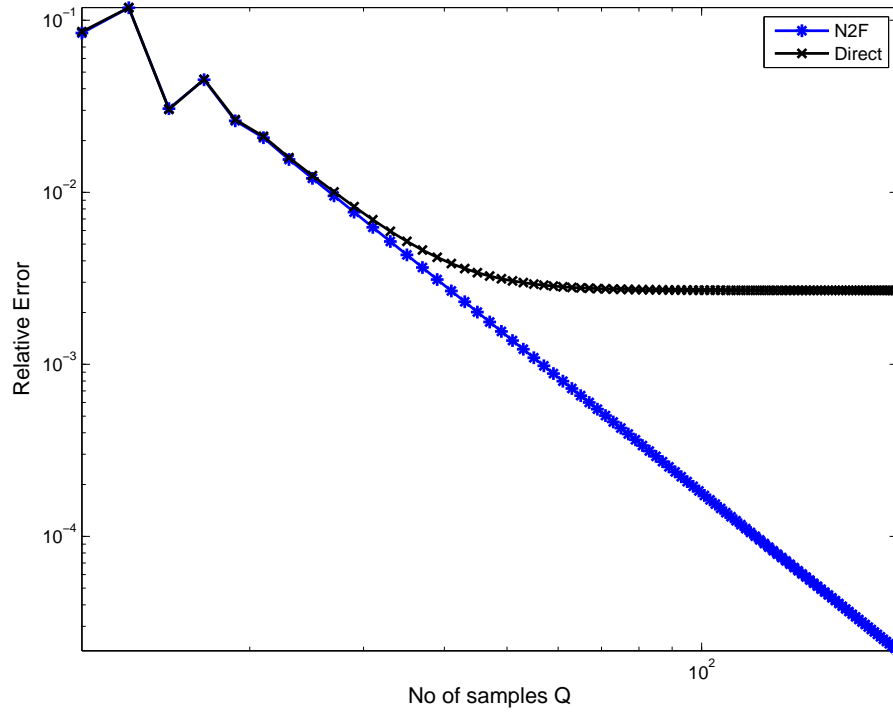


Figure 2.27: N2F error introduced with the 2nd order interpolating functions.

In order to see if we can achieve even faster convergence, 3rd order *Lagrange polynomials* have been also tested. Figure 2.28 shows the *cubic* basis of an element, and

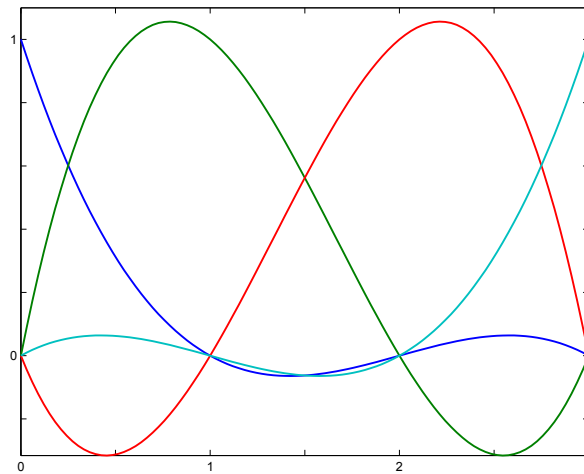


Figure 2.28: 3rd order interpolating polynomials for the first 4 nodes.

they are analytically expressed as

$$\begin{aligned}
 \Theta_1(\hat{\mathbf{r}}) &= \begin{cases} \frac{1}{2}(1-\xi)(2-3\xi)(1-3\xi), & \xi = \frac{\theta_4 - \theta}{\theta_4 - \theta_1}, \theta \in [\theta_1, \theta_4] \\ 0 & \text{elsewhere} \end{cases} \\
 \Theta_2(\hat{\mathbf{r}}) &= \begin{cases} \frac{9}{2}\xi(1-\xi)(2-3\xi), & \xi = \frac{\theta_4 - \theta}{\theta_4 - \theta_1}, \theta \in [\theta_1, \theta_4] \\ 0 & \text{elsewhere} \end{cases} \\
 \Theta_3(\hat{\mathbf{r}}) &= \begin{cases} \frac{9}{2}\xi(1-\xi)(3\xi-1), & \xi = \frac{\theta_4 - \theta}{\theta_4 - \theta_1}, \theta \in [\theta_1, \theta_4] \\ 0 & \text{elsewhere} \end{cases} \\
 \Theta_4(\hat{\mathbf{r}}) &= \begin{cases} \frac{1}{2}\xi(2-3\xi)(1-3\xi), & \xi = \frac{\theta_4 - \theta}{\theta_4 - \theta_1}, \theta \in [\theta_1, \theta_4] \\ 0 & \text{elsewhere} \end{cases}
 \end{aligned} \tag{2.2.13}$$

The results of the approximation, made similarly to the two previous cases, are shown in figure 2.29. The convergence slope is higher. Only about 35 snapshots are

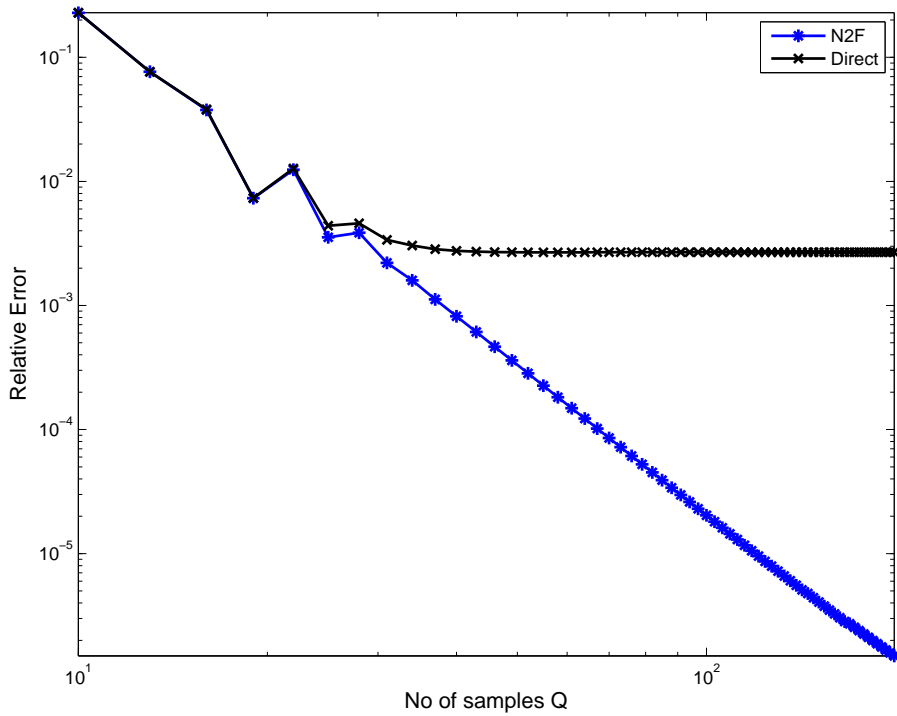


Figure 2.29: N2F error introduced with the 3rd order interpolating functions.

needed to achieve an error below 10^{-3} . With 200 snapshots, we have achieved an error

two orders of magnitude below the one we had with roof-top functions. Extrapolating the convergence behaviors for each of the error plots of figures 2.25, 2.27 and 2.29, we may conclude that

Conclusion 5 *Standard FEM 1st, 2nd, 3rd order polynomials allow the approximation of the N2F operator in the look angle parameter, and the convergence is in the order of, respectively, 40 dB/dec, 60 dB/dec and 80 dB/dec.*

The number of snapshots required by a 3rd order basis for the interpolation of an operator acting on the fields produced by an array of 5 point sources is about 35. Before we proceed in the trigonometric polynomials approximation, we check how the error increases as we further increase the radius of the sphere letting the number of the point sources double. The results are shown in figure 2.30. The number of

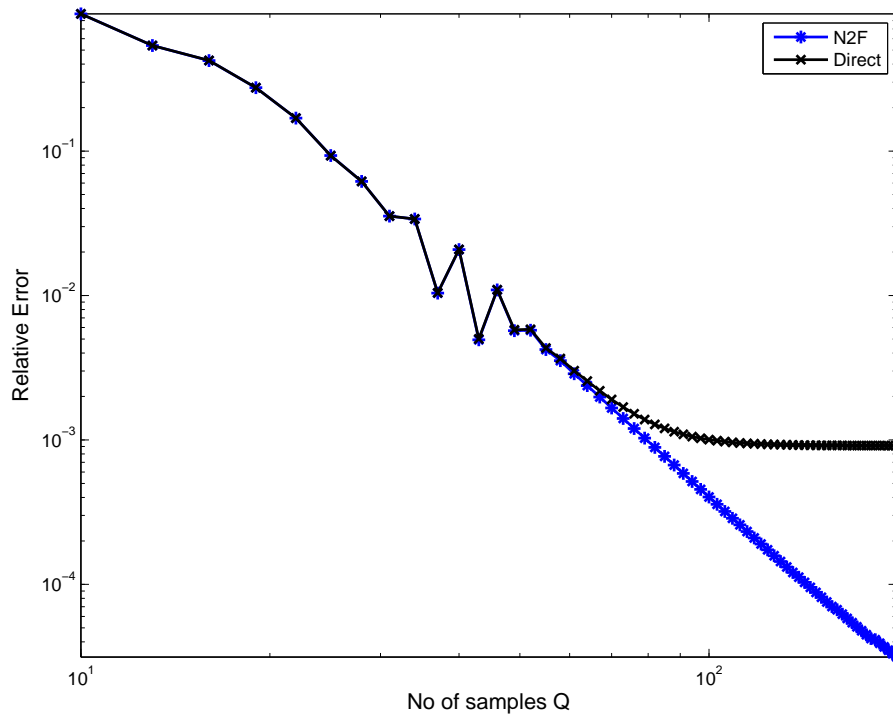


Figure 2.30: N2F error introduced with the 3rd order interpolating functions for an operator build on a sphere enclosing 10 point sources (radius of $5\lambda/4$ and sampling resolution of $\lambda/10$).

snapshots required to preserve the accuracy is about 100, a value that is too high to consider approximating very large arrays.

2.2.2 Trigonometric polynomials interpolation of the N2F

Operator

Using a similar formalism as introduced the previous sections 2.1.1 and 2.2.1, we extend the notion of polynomial basis approximation to the case of *complex trigonometric polynomials* of the form

$$z(\mathbf{r}(\theta)) = \frac{a_0}{2} + \sum_{m=1}^M [a_m \cos(m\theta) + b_m \sin(m\theta)],$$

$$a_m, b_m \in \mathbb{C} \text{ for } 0 \leq m \leq M, \quad \theta \in \mathbb{R}, \quad (2.2.14)$$

where we have assumed $\hat{\mathbf{r}} \in \mathcal{D}_{\phi=0^\circ}$. Using *Euler's formulas* with $e^{im\theta} = \cos(m\theta) + i \sin(m\theta)$, i being the imaginary unit, (2.2.14) can be rewritten as [31]

$$z(\mathbf{r}(\theta)) = \sum_{m=-M}^M c_m e^{im\theta}, \quad c_m \in \mathbb{C} \text{ for } -M \leq m \leq M, \quad \theta \in \mathbb{R}. \quad (2.2.15)$$

Now, the complex Fourier series approximation of a function $f(x)$, periodic⁶ of period L such that $f(x) = f(x + L)$, is given by

$$f(x) = \sum_{r=-\infty}^{\infty} c_r e^{i \frac{2\pi}{L} r x}, \quad (2.2.16)$$

and the complex coefficients c_r are

$$c_r = \frac{1}{L} \int_{x_0}^{x_0+L} f(x) e^{-i \frac{2\pi}{L} r x} dx, \quad x_0 \in \mathbb{R}. \quad (2.2.17)$$

$\phi_r(x) = e^{i \frac{2\pi}{L} r x}$, $\forall r \in \mathbb{Z}$ is a set of orthogonal functions or *eigenfunctions* in the sense of (2.1.2). Now, considering $x = \theta$, and as the domain of θ is, for the spherical geometry of the radiation problem, periodic of $360^\circ = 2\pi$, we set $L = 2\pi$. For $M \rightarrow \infty$, we have that the finite sum approximation (2.2.15) becomes the Fourier approximation stated in (2.2.16) with the variables changes made, thus we can use the highly developed mathematical and numerical foundations on the Fourier series to compute an approximant of $z(\mathbf{r}(\theta))$. As we are interested in an approximation of the operator, we evaluate $z(\mathbf{r}(\theta)) = \tilde{\mathcal{L}}(\hat{\mathbf{r}}(\theta))$ the approximated functional.

⁶ The first of the four Dirichlet conditions [30].

The coefficients c_r of (2.2.17) may be computed by a *Discrete Fourier Transform* (DFT), i.e. by a numerical integration of (2.2.17), the interval $[x_0, x_0 + L)$ being subdivided into N equal intervals, and the N samples of $f(x)$ taken in a domain of zero measure⁷. This step can be efficiently performed through the *Fast Fourier Transform* (FFT) algorithm [31]. The FFT computes the Fourier coefficients $\mathbf{X}(m)$ of a sequence $\mathbf{x}(n)$, assuming $\mathbf{x}(n)$ to be repeated infinitely and periodically along the sampling space and performing the following summations:

$$\mathbf{X}(m) = \sum_{n=1}^N \mathbf{x}(n) e^{-i \frac{2\pi}{N} (n-1)(m-1)}, \quad m = 1, \dots, N. \quad (2.2.18)$$

The assumption of the periodicity of $\mathbf{x}(n)$, in our case, is valid as long as our operator is built by scanning θ all over 360° . The sampled sequence can be recovered from the coefficients by the *Inverse FFT* (iFFT)

$$\mathbf{x}(n) = \frac{1}{N} \sum_{m=1}^N \mathbf{X}(m) e^{i \frac{2\pi}{N} (n-1)(m-1)}, \quad n = 1, \dots, N. \quad (2.2.19)$$

Now, assuming the N2F operator to be $\mathcal{L}(\hat{\mathbf{r}}(\theta)) = \mathcal{L}(\theta)$, and $\mathbf{x}(n)$ the sequence obtained by the snapshots

$$\mathbf{x}(n) = \mathcal{L}(\theta_n) = \mathcal{L}\left(\frac{2\pi}{N}(n-1)\right), \quad n = 1, \dots, N,$$

we can express $\mathcal{L}(\theta_n)$ by means of the Fourier coefficients $\mathbf{X}(m)$, $m = 1, \dots, N$ with their respective eigenfunction $e^{i\theta_n(m-1)}$, $m-1$ being the associated *eigenfrequency*. For the FFT algorithm, the spectrum of the eigenfrequencies is such that the first $m = 2, \dots, \lfloor N/2 \rfloor + 1$ correspond to positive frequencies $(m-1)$ and the next $m = \lfloor N/2 \rfloor + 2, \dots, N$ correspond to the negative frequencies $N+1-m$. The continuous spectral component corresponds to $m = 1$. *Aliasing* [31] in the original sequence reconstruction may occur, and for the *sampling theorem* we need to sample the operator such that $N \geq 2q$ where q is the highest eigenfrequency associated to non null (or numerically significant) coefficient values $\mathbf{X}(q)$.

The discretized eigenfunctions of the FFT can be extrapolated to the continuous case considering $\lim_{N \rightarrow \infty} \theta_n = \theta \in [0, 2\pi)$, and we obtain $\mathcal{L}(\theta_n) \rightarrow \mathcal{L}(\theta)$. Thus, we can

⁷ Zero measure for the sampled function is achieved by a Dirac comb, simplifying the integral by the sifting property of the Dirac delta.

express the N2F operator as, if the number of sampling points N is odd,

$$\begin{aligned}\mathcal{L}(\theta) = & \frac{1}{N} \left(\mathbf{X}(1) + \mathbf{X}(2)e^{i\theta} + \mathbf{X}(3)e^{i2\theta} + \dots \right. \\ & \dots + \mathbf{X}(\lfloor N/2 \rfloor + 1)e^{i\lfloor N/2 \rfloor \theta} + \mathbf{X}(\lfloor N/2 \rfloor + 2)e^{-i(\lfloor N/2 \rfloor + 1)\theta} + \dots \\ & \left. \dots + \mathbf{X}(N-2)e^{-i3\theta} + \mathbf{X}(N-1)e^{-i2\theta} + \mathbf{X}(N)e^{-i\theta} \right),\end{aligned}\quad (2.2.20)$$

or as, if the number of sampling points N is even,

$$\begin{aligned}\mathcal{L}(\theta) = & \frac{1}{N} \left(\mathbf{X}(1) + \mathbf{X}(2)e^{i\theta} + \mathbf{X}(3)e^{i2\theta} + \dots \right. \\ & \dots + \mathbf{X}(N/2)\cos\left(\frac{N}{2}\theta\right) + \dots \\ & \left. \dots + \mathbf{X}(N-2)e^{-i3\theta} + \mathbf{X}(N-1)e^{-i2\theta} + \mathbf{X}(N)e^{-i\theta} \right).\end{aligned}\quad (2.2.21)$$

Now, performing the trigonometric polynomials approximation or *DFT-truncation* by limiting the number of coefficients to $R \in \mathbb{N}$ around the continuous spectral component, that is the odd number of coefficients $2R + 1$, the full interpolations of (2.2.20) and (2.2.21) reduce to

$$\begin{aligned}\tilde{\mathcal{L}}(\theta) = & \frac{1}{N} \left(\mathbf{X}(1) + \mathbf{X}(2)e^{i\theta} + \mathbf{X}(3)e^{i2\theta} + \dots \right. \\ & \dots + \mathbf{X}(R+1)e^{iR\theta} + \mathbf{X}(N-R+1)e^{-iR\theta} + \dots \\ & \left. \dots + \mathbf{X}(N-2)e^{-i3\theta} + \mathbf{X}(N-1)e^{-i2\theta} + \mathbf{X}(N)e^{-i\theta} \right).\end{aligned}\quad (2.2.22)$$

It is now possible to apply the DFT-truncation to a selected N2F problem. We chose, in order to compare the results to those obtained by the FEM basis based approximation, a linear array of 5 point sources within a sphere of radius of $3\lambda/2$ and sampling resolution of $\lambda/10$. The number of look angles in order to build the operator matrix of snapshots \mathbf{x}_N is of $N = 300$ in the range $[0^\circ, 360^\circ)$. Figure 2.31 shows the spectral coefficients \mathbf{X} computed by an FFT on the rows (look angle dependent) of \mathbf{x}_N .

The spectrum is confined within ± 32 coefficients around the continuous spectral component, range over which they remain in the numerical null level ($\approx -250\text{dB}$).

The computation of the error induced in the pattern by the DFT-truncation is shown in figure 2.32. As we can see, the error drops rapidly from 11 coefficients till

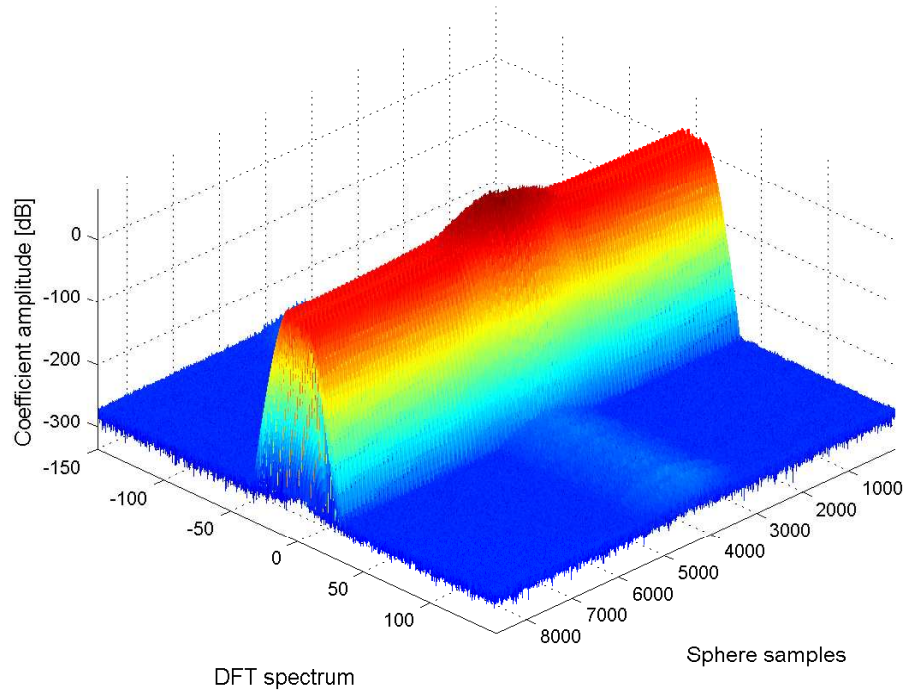


Figure 2.31: Spectral coefficients of an operator build for a sphere enclosing 5 point sources (radius of $3\lambda/2$ and sampling resolution of $\lambda/10$).

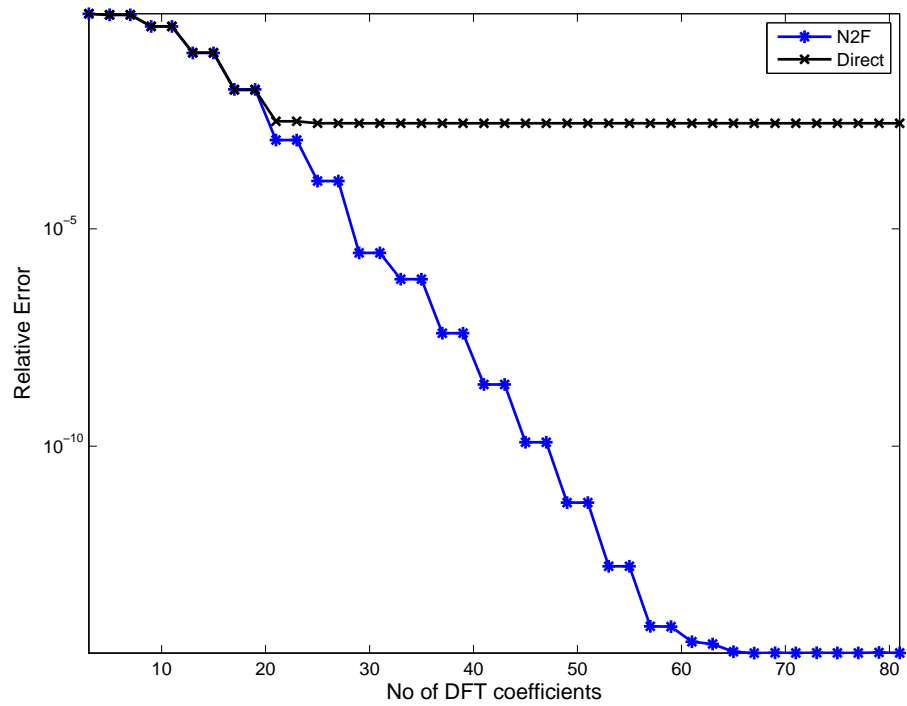


Figure 2.32: Error in the far fields induced by DFT-truncation.

we have null error with only 65 coefficients. For our purposes, we can retain 21 coefficients in order to achieve the required accuracy in the pattern. This value is lower than that of the 3rd order basis polynomial interpolation, where we needed about 35 snapshots.

We may now check the performances of the DFT-truncation as the array grows in the number of point sources. We choose 10 point sources in order to compare the performances to the 3rd order basis approximation results of figure 2.30. The results are depicted in figure 2.33. Only 41 coefficients are needed to accurately perform the

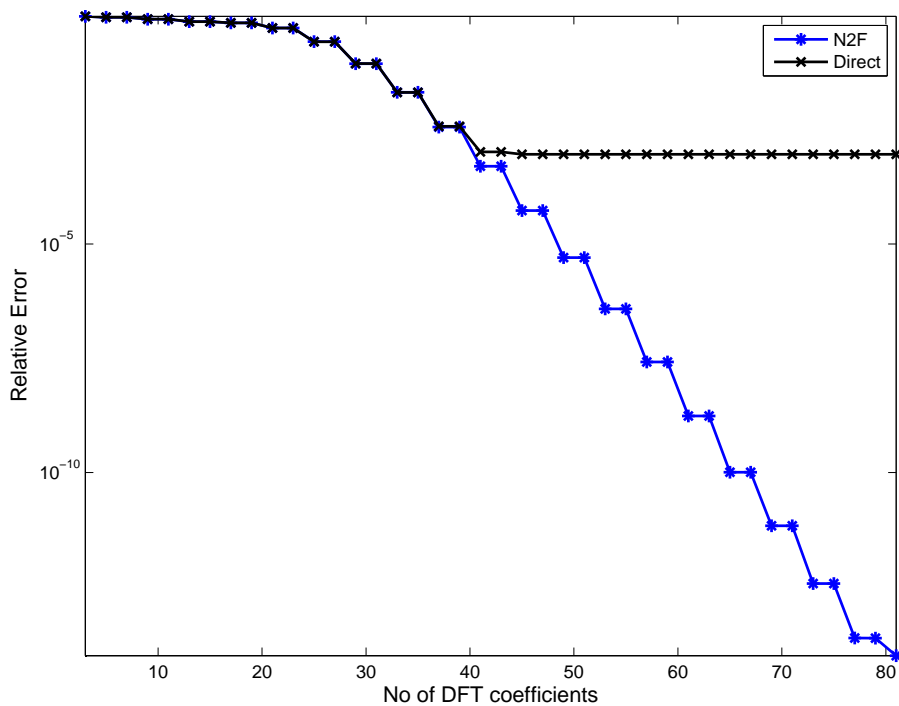


Figure 2.33: Error in the far fields induced by DFT-truncation for the linear array of 10 point sources.

pattern computations, which is definitely lower than the 100 required for the 3rd order basis approximation.

As we have seen along the process of choosing the appropriate approximation space for the N2F operator, we can conclude that

Conclusion 6 *The relevant Fourier coefficients have resulted to be a few ones, allowing us to represent the N2F operator as a finite sum of trigonometric polynomials. The*

performances of the DFT-truncation are better than those achieved by the polynomial interpolation. To compute the values of the coefficients, it is required to oversample the operator in order to avoid aliasing, and this step is dependent on the size of the array enclosed which determines the highest eigenfrequency. The DFT-truncation technique is very promising for large arrays approximations.

2.3 Low-rank approximations on a bounding parallelepiped

Similar results as those obtained for a bounding sphere, either in the approximation of the near field, unless the field rotation test that specifically requires a sphere (fig. 2.20), or that of the N2F operator, have been obtained for a bounding parallelepiped. Thus, to avoid redundancy, the results for a bounding parallelepiped won't be presented. Notice that, as the number of sampling points with the bounding box are lower than those for the bounding sphere, the computations require less time. The main reason we have decided to perform the computations on a box is that the finite element domain of computation is reduced to a parallelepiped, especially for planar arrays. Using a bounding sphere would lead to an enormous waste of computational resources that we must avoid in order to handle very large arrays.

MODEL ORDER REDUCTION OF PHASED ARRAY ANTENNAS

Even with the immense computing power nowadays available, the electromagnetic modeling of electrically large structures, due to their high computational resources demand, still remains a challenge. Techniques such as the *domain decomposition* [25, 26] may be used in order to split a large computational domain into smaller ones, reducing in this way the memory requirements and the overall computational time. The finite elements analysis of arbitrarily shaped radiating structures is usually achieved by the decoupling of the finite elements formulation, that is a system of differential equations stated in a weak form to obtain a linear system of equations, from the boundary integrals required to compute the radiated far fields from equivalent surface currents. Thus the finite elements domain is limited to the near fields region, truncating the finite elements domain such that the memory requirements become acceptable. Then the fields computed from a surface bounding the radiating elements allow the near fields to far fields transformations computing the integrals presented in chapter 1.

The Petrov-Galerkin projections [13] on the finite elements differential equations leads to a linear system of equations in which the unknowns are the coefficients for the chosen basis expansion. This linear system can be thought as the input linear system of equations of a radiating model, and the spanning coefficients of the basis as a *state vector*. Then, an output system of equations, based on the N2F operator introduced in chapter 2, modified in order to act on the state vector, completes the modeling of an analyzed radiating structure.

The full system obtained in such a way is composed by very large but sparse matrices, typically with hundred thousands and even hundred millions of unknowns. The application of projection based model order reduction techniques, leading to full matrices but of several orders of magnitude lower, allows fast on-line stage computations. Furthermore, the approximations made in the far-fields operators through the DFT-truncation allow to minimize the size of the system output matrix, especially for very large planar arrays.

In a first part of this chapter, the general FEM formulation for the input system matrices will be viewed, together with the construction of the output system matrices, in order to build the full radiation model. Then, the choice of the approximation spaces for the near fields will be discussed for the model order reduction, keeping particular attention on the error introduced. Finally, the effectiveness of a model order reduction applied to two different radiating structures will be shown, comparing the results to the full-model computations.

3.1 The FEM vector Helmholtz formulation

The most commonly employed formulation of the full-wave finite elements for solving the Maxwell's equations in a bounded domain is the vector Helmholtz equation for the electric field, recast in a weak form (*weighted residuals*) to achieve a linear equations system. The weak form is supplied by the testing of (1.1.31) with oppor-

tune basis, the *curl-conforming vector finite elements*¹. Consider the domain $\Omega \subset \mathbb{R}^3$ to be bounded by $\partial\Omega = \Gamma = \Gamma_E \cup \Gamma_H \cup \Gamma_{WG} \cup \Gamma_R$ as depicted in figure 3.1. Γ_E corresponds

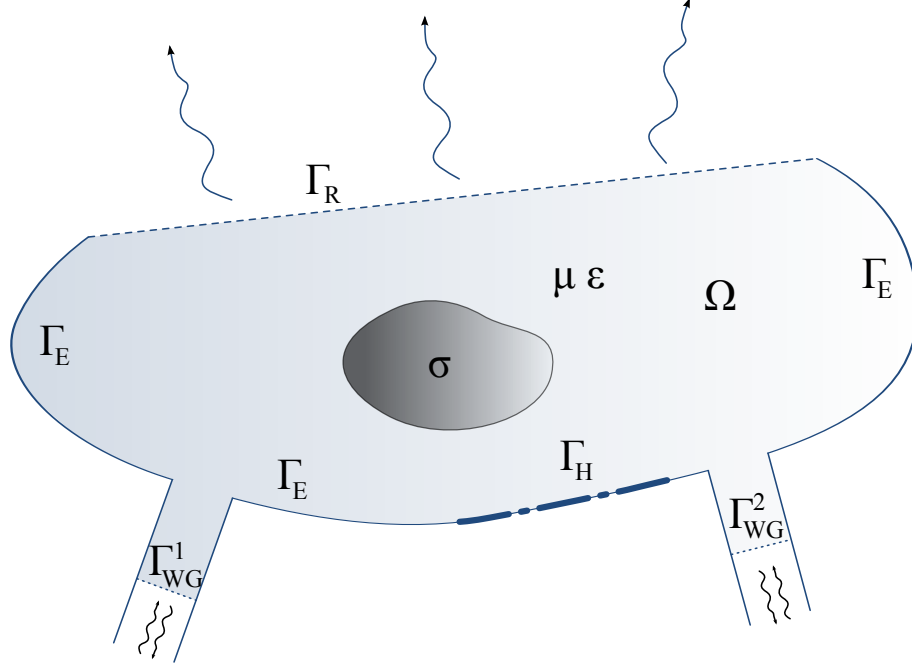


Figure 3.1: FEM domain of the radiation problem.

to Dirichlet conditions boundaries, Γ_H to Neumann conditions boundaries, Γ_{WG} to waveguides truncation boundaries, and Γ_R is an boundary through which the electromagnetic power flows, that is the radiation boundary. Consider now the discretized domain $\Omega_h = \bigcup_{n=1}^N \Omega_n \subset \Omega$, where the subdomains Ω_n (the tetrahedra for example) are such that $\Omega_n \cap \Omega_m = \{0\}$ for $n \neq m$. Ω_h is parameterized in by the maximum diameter h of the subdomains Ω_n , and we shall assume that as $h \rightarrow 0$, $\Omega_h \rightarrow \Omega$. With $\hat{\mathbf{n}}$ pointing outwardly from Ω , consider the *Sobolev* space [34] $\mathcal{W} = \mathcal{W}(\Omega_h) \subset \mathcal{H}(\text{curl}; \Omega)$ of the *trial* functions \mathbf{w} , defined by the direct sum of two closed subspaces as follows

$$\begin{aligned} \mathcal{W} &= \mathcal{W}_D \oplus \mathcal{W}_E, \\ \mathcal{W}_D &:= \{\mathbf{w} \in \mathcal{W} \mid \hat{\mathbf{n}} \times \mathbf{w} = 0 \text{ on } \Gamma_E\} \subset \mathcal{H}(\text{curl}; \Omega), \\ \mathcal{W}_E &:= \{\mathbf{w} \in \mathcal{W} \mid \hat{\mathbf{n}} \times \mathbf{w} \neq 0 \text{ on } \Gamma_E\} \subset \mathcal{H}(\text{curl}; \Omega, \Gamma_E). \end{aligned} \quad (3.1.1)$$

¹ Initially introduced by Nédélec, then developed by the research community into the so-called *hierarchical finite element basis* for vector fields.

\mathcal{W}_D is in fact the subspace of the imposed Dirichlet conditions. The total electric field is given by the approximation finite summations

$$\begin{aligned} \mathbf{E} &= \hat{\mathbf{E}} + \mathbf{E}_D, \\ \hat{\mathbf{E}} &:= \sum_i x_i \mathbf{w}_i, \quad \mathbf{w}_i \in \mathcal{W}_E, \\ \mathbf{E}_D &:= \sum_j x_j \mathbf{w}_j, \quad \mathbf{w}_j \in \mathcal{W}_D. \end{aligned} \quad (3.1.2)$$

With Galerkin projections (the test functions are the same as the trial functions), it is possible to construct an algebraic linear system with as unknowns only the coefficients x_i . In effect, x_j are not problem unknowns as they are given by the boundary conditions.

Now, as Ω does not contain any impressed current sources, only induced currents persist and (1.1.31) can be rewritten as [33]

$$\nabla \times \frac{1}{\mu_r} \nabla \times \mathbf{E} + j k_0 \zeta_0 \sigma \mathbf{E} - k_0^2 \epsilon_r \mathbf{E} = 0, \quad (3.1.3)$$

with $k_0 = \omega \sqrt{\epsilon_0 \mu_0}$ the free space wave number and ζ_0 the free space plane wave impedance. For notation disambiguation, notice that the formulation presented is a frequency-domain one, and the spectrum $\tilde{\mathbf{E}}(\mathbf{r}, \omega)$ has to be computed by means of a frequency sweep. Thus, consider $\tilde{\mathbf{E}}(\mathbf{r}, \omega) \Big|_{\omega=\omega_n} = \mathbf{E}$ to be the electric field at a given angular frequency ω_n . The boundary conditions can be stated as

$$\begin{aligned} \hat{\mathbf{n}} \times (\mathbf{E} \times \hat{\mathbf{n}}) &= \bar{\mathbf{E}}_t, \quad \text{on } \Gamma_E, \\ \hat{\mathbf{n}} \times (\mathbf{H} \times \hat{\mathbf{n}}) &= \bar{\mathbf{H}}_t, \quad \text{on } \Gamma_H, \\ \hat{\mathbf{n}} \times (\mathbf{E} \times \hat{\mathbf{n}}) &= Z_s \mathbf{H} \times \hat{\mathbf{n}}, \quad \text{on } \Gamma_R, \\ \hat{\mathbf{n}} \times (\mathbf{H} \times \hat{\mathbf{n}}) &= \sum_k (a_k^i - a_k^r) \mathbf{H}_t^k, \quad \text{on } \Gamma_{WG}, \end{aligned} \quad (3.1.4)$$

$\bar{\mathbf{E}}_t$ and $\bar{\mathbf{H}}_t$ known values, Z_s the wave impedance at the radiation boundary, and a_k^i, a_k^r the k^{th} complex modal incident and reflected amplitudes. We proceed with the Galerkin projections, obtaining [33]

$$\int_{\Omega} \nabla \times \mathbf{w}_i \cdot \frac{1}{\mu_r} \nabla \times \mathbf{E} d\Omega + j k_0 \zeta_0 \int_{\Omega} \mathbf{w}_i \cdot \sigma \mathbf{E} d\Omega +$$

$$\begin{aligned}
& j k_0 \zeta_0 \int_{\Gamma_R} \hat{\mathbf{n}} \times \mathbf{w}_i \cdot \frac{1}{Z_s} \hat{\mathbf{n}} \times \mathbf{E} d\Gamma - k_0^2 \int_{\Omega} \mathbf{w}_i \cdot \epsilon_r \mathbf{E} d\Omega \\
& = j k_0 \zeta_0 \int_{\Gamma_{WG}} \mathbf{w}_i \cdot \hat{\mathbf{n}} \times \mathbf{H}_t d\Gamma, \quad \forall \mathbf{w}_i \in \mathcal{W}_E.
\end{aligned} \tag{3.1.5}$$

On Γ_{WG} , if we consider the wave ports to be fed only by the dominant mode (lowest cutoff frequency), the following relation holds for the k^{th} port [32, 35]

$$\hat{\mathbf{n}} \times \mathbf{H}_t^k = \frac{1}{Z_k} \hat{\mathbf{n}} \times \hat{\mathbf{n}} \times \mathbf{E}_t^k - \frac{2}{Z_k} \hat{\mathbf{n}} \times \hat{\mathbf{n}} \times \mathbf{E}_t^{k \text{ inc}}, \quad \text{on } \Gamma_{WG}^k, \tag{3.1.6}$$

where $\mathbf{E}_t^{k \text{ inc}}$ is the incident electric field and Z_k the modal impedance. Assuming the waveguides segments on which the wave ports are applied to be long enough such that the higher order modes are evanescent and once they encounter the electromagnetic structure's discontinuities (e.g. the junction to the antenna) their power contribution is several order of magnitude lower than the dominant mode, this so-called *transfinite elements method* [35] allows to feed a generic structure though waveguides and (3.1.5) becomes

$$\begin{aligned}
& \int_{\Omega} \nabla \times \mathbf{w}_i \cdot \frac{1}{\mu_r} \nabla \times \mathbf{E} d\Omega + j k_0 \zeta_0 \int_{\Omega} \mathbf{w}_i \cdot \sigma \mathbf{E} d\Omega - \\
& k_0^2 \int_{\Omega} \mathbf{w}_i \cdot \epsilon_r \mathbf{E} d\Omega + j k_0 \zeta_0 \int_{\Gamma_R} \hat{\mathbf{n}} \times \mathbf{w}_i \cdot \frac{1}{Z_s} \hat{\mathbf{n}} \times \mathbf{E} d\Gamma + \\
& \sum_{m=1}^M \frac{j k_0 \zeta_0}{Z_m} \int_{\Gamma_{WG}^m} \hat{\mathbf{n}} \times \mathbf{w}_i \cdot \hat{\mathbf{n}} \times \mathbf{E}_t d\Gamma \\
& = \frac{j 2 k_0 \zeta_0}{Z_k} \int_{\Gamma_{WG}^k} \hat{\mathbf{n}} \times \mathbf{w}_i \cdot \hat{\mathbf{n}} \times \mathbf{E}_t^{k \text{ inc}} d\Gamma, \quad \forall \mathbf{w}_i \in \mathcal{W}_E
\end{aligned} \tag{3.1.7}$$

where M is the total number of ports and $1 \leq k \leq M$. The present formulation, for the summation all over the ports entering into the computational domain, couples one port to the others, hence models the mutual couplings between the radiating elements. The condition on Γ_R is an impedance condition, the so-called *absorbing boundary condition* (ABC), which ideally annihilates the plane wave reflection on the boundary. Actually, the reflection coefficient is strongly dependent on the incidence angle of the plane wave, being null for perpendicular one. In order to keep sufficient validity in the computation of the fields in opened structures, the ABCs must

be placed sufficiently far away from the radiating elements or scatterers such that incidence becomes less oblique. For example, in the commercial CAD HFSS², the recommendations are to place the radiation boundaries at least at $\lambda_{\min}/2$ away from the radiating sources, where λ_{\min} is associated to highest frequency set in a frequency sweep.

Equation (3.1.7) leads, with the field expansion of (3.1.2) and setting the solving frequency ($k_0 = \omega \sqrt{\epsilon_0 \mu_0}$), to a linear system of the form [28, 32]

$$\mathbf{A} \mathbf{x} = \mathbf{b}, \quad (3.1.8)$$

where $\mathbf{A} \in \mathbb{C}^{N \times N}$ is a symmetric matrix, $\mathbf{x}, \mathbf{b} \in \mathbb{C}^N$ and N the number of unknowns or *degrees of freedom* (DoFs).

The system of (3.1.8) is such that, in the case we are analyzing an electrically large structure, N is in the order of hundred thousands to several millions. This is due to the fact that the size of the elements h has to be very low respectively to the wavelength in order to reduce the fields *jumps* from one element to a neighboring one. Typical values are comprised between $\lambda/3$ and $\lambda/10$ in order to keep sufficient accuracy while not exceeding in the computational resources demand. Also, when using higher order polynomials to approximate the fields, as the number of basis functions increase, the number of unknowns or DoFs increase. Where the fields are known to vary rapidly, e.g. next to fields singularities like the edges of a conducting plate, the size of the elements must be lowered to achieve better accuracy. All these factors have to be taken into account for an effective design, and the final system dimension depends on them.

² Ansoft HFSSTM (acquired by Ansys Inc.). Further informations available at <http://www.ansys.com/products/electromagnetics/>.

3.2 Projection-based model order reduction

Definition 2 Consider the single input, single output (SISO) polynomially parameterized full system

$$\begin{aligned} \mathbf{A} \mathbf{x}(p) &= \left(\sum_{i=1}^M \Theta_i(p) \mathbf{b}_i \right) u(p), \\ y(q) &= \left(\sum_{j=1}^Q \Omega_j(q) \mathbf{c}_j^H \right) \mathbf{x}(p), \end{aligned} \quad (3.2.9)$$

with $\mathbf{A} \in \mathbb{C}^{N \times N}$, $\mathbf{x}, \mathbf{b}_i, \mathbf{c}_i \in \mathbb{C}^N$, \mathbf{b}_i being the i^{th} system input vector, \mathbf{c}_j the j^{th} output vector, $\Theta_i(p)$ the i^{th} term of the polynomial parameterization in p the input system matrix and $\Omega_j(p)$ the j^{th} term of the polynomial parameterization in q of the output matrix. The projection-based reduced order model (ROM) is given by [33]

$$\begin{aligned} \tilde{\mathbf{A}} \tilde{\mathbf{x}}(p) &= \left(\sum_{i=1}^M \Theta_i(p) \tilde{\mathbf{b}}_i \right) u(p), \\ y(p) &= \left(\sum_{j=1}^M \Omega_j(q) \tilde{\mathbf{c}}_j^H \right) \tilde{\mathbf{x}}(p), \end{aligned} \quad (3.2.10)$$

with

$$\begin{aligned} \tilde{\mathbf{A}} &:= \mathbf{W}^H \mathbf{A} \mathbf{V} \\ \tilde{\mathbf{b}}_i &:= \mathbf{W}^H \mathbf{b}_i, \\ \tilde{\mathbf{c}}_j &:= \mathbf{V}^H \mathbf{c}_j, \end{aligned} \quad (3.2.11)$$

and $\mathbf{W}, \mathbf{V} \in \mathbb{C}^{N \times n}$, $n \ll N$.

The full unknowns vector is approximated by $\mathbf{x} \approx \mathbf{V} \tilde{\mathbf{x}}$, that is \mathbf{x} is spanned by the column space of \mathbf{V} (trial vectors) through the coefficients $\tilde{\mathbf{x}}$ computed from the solution of the ROM input system. Thus, \mathbf{V} constitute a set of global basis vectors for the full FEM system. \mathbf{W}^H applied to the column vectors of a matrix or to a vector is a testing operation with the space spanned by the columns of \mathbf{W} (see chapter 2).

3.3 Scan and look angles parameterized radiation model

The full system (3.2.9) represents our electromagnetic model of a phased array. Each column vector \mathbf{b}_i represent a different right-hand side of the system, considering one by one each of the g excitation ports. In effect, with (3.1.7) the right-hand side is build for each k with $1 \leq k \leq M = g$, one by one while looking at the fields, that is the unknowns to find, produced by the excitations taken singularly. The superposition of the solutions, as the system is invariant (\mathbf{A} remains the same all along this process), gives the fields produced by the ports excited contemporaneously. This is obvious if we think of the linearity property of the system. Now, as we are seeking for a beamsteering operation, and we know that it is achieved by relative phase shifts between the excitations given by (1.2.97), the polynomial terms are given by $\Theta(\theta_x, \theta_y) = \{a_i e^{-jk(x_i \sin(\theta_x) + y_i \sin(\theta_y))}, 1 \leq i \leq g\}$ where $a_i \in \mathbb{C}$ is complex coefficient that can be devoted to pattern shaping [3, 4] or left to 1 if we desire only the beamsteering. We can rewrite the right-hand side of the input equation of (3.2.9) as the sum of coefficient-vector products

$$\mathbf{A} \mathbf{x} = a_1 e^{-jk(x_1 \sin(\theta_x) + y_1 \sin(\theta_y))} \mathbf{b}_1 + \dots + a_g e^{-jk(x_g \sin(\theta_x) + y_g \sin(\theta_y))} \mathbf{b}_g, \quad (3.3.12)$$

emphasizing the parameterization of the system by the scan angle (θ_x, θ_y) . We have reduced this way the inputs variability to only two values, that is the scan angles in both x and y directions.

The output equation now has to be formulated in such a way that, from the solutions computed by the input equations, we derive the fields in several sampling points surrounding the array, then, applying the N2F operator we obtain the sought spherical components of the far fields detectors. The *solutions-to-fields* operator $\mathcal{F}(x)$ can be viewed as a large (as large as the unknowns) but sparse matrix that opportunely selects the solutions related to the elements in which the fields have to be sampled, then using them in the expansion (3.1.2), recovers the vector fields, electric and magnetic, in each selected point providing for example their Cartesian compo-

nents. Notice that, for Faraday's law (1.1.15) and the constitutive relation (1.1.21), the magnetic field is derived from the electric field by a curl operation. Then, from the near fields we can apply our N2F operator $\mathcal{L}(\cdot; \theta)$ (having opportunely included in the operator (1.3.109) the $\hat{\mathbf{n}} \times \cdot$ operation on the fields to achieve the tangential components, that is the equivalent currents, and the Cartesian to spherical transformation of note 17) to the operator $\mathcal{F}(x)$, that is $\mathcal{L}(\mathcal{F}(x); \theta)$ to obtain the far fields detectors in the look angle direction θ for the chosen ϕ plane. As we have chosen to supply a DFT-truncation in order to reduce the dimensions of the output operator, the operator $\mathcal{L}(\cdot; \theta)$ is now given by the approximation (2.2.22), such that the rows are given by the $c = 2R + 1$ coefficients chosen in the expansion. We can thus write the output matrix as

$$\begin{aligned} \mathbf{c}_j &= \text{col}_j \left(\mathbf{F}^H \tilde{\mathbf{X}}^H \right) \Omega_j^\dagger(\theta) = \mathbf{c}'_j \Omega_j^\dagger(\theta), \\ \mathbf{F} &\in \mathbb{C}^{l \times N}, \tilde{\mathbf{X}} \in \mathbb{C}^{1 \times l}, \mathbf{c}'_j \in \mathbb{C}^{N \times 1}, 1 \leq j \leq Q = c, \end{aligned} \quad (3.3.13)$$

with $\Omega(\theta) = \{1, e^{j\theta}, \dots, e^{jR\theta}, e^{-jR\theta}, \dots, e^{-j\theta}\}$ the polynomial terms of the output system parameterized in the look angle θ . l is the number of vector components for all the sampling points, that is 6 times the number of sampling points. To handle the θ and ϕ polarizations, it is necessary to provide two different DFT coefficients matrices \mathbf{X}_ϕ and \mathbf{X}_θ , computing separately the far field detectors in each polarization, here considered in the only output y . The full system of the radiating model can be stated as

$$\begin{aligned} \mathbf{A} \mathbf{x} &= a_1 e^{-jk(x_1 \sin(\theta_x) + y_1 \sin(\theta_y))} \mathbf{b}_1 + \dots + a_g e^{-jk(x_g \sin(\theta_x) + y_g \sin(\theta_y))} \mathbf{b}_g \\ y &= \left(\mathbf{c}'_1^H + \dots + e^{jR\theta} \mathbf{c}'_{R+1}^H + e^{-jR\theta} \mathbf{c}'_{R+2}^H + \dots + e^{-j\theta} \mathbf{c}'_{2R+1}^H \right) \mathbf{x}, \\ \mathbf{z} &= \mathbf{F} \mathbf{x}. \end{aligned} \quad (3.3.14)$$

The power radiated may be computed separately using (1.3.114), considering the near fields (\mathbf{z}) obtained by $\mathbf{F} \mathbf{x}$, with \mathbf{F} a *solutions-to-near-fields* operator. According to [22], it is possible to include the power radiated computation into the output functional $\mathcal{L}(\mathcal{F}(x); \theta)$, combining the power reflected at the ports and the power losses that may occur in dispersive media. Notice that the total power radiated vary

during the beamsteering operation, the mutual couplings varying as the excitations change, thus has to be computed for each scan angle selected. Finally, the patterns are derived using (1.3.112) and (1.3.113). A model schematic is illustrated in figure 3.2.

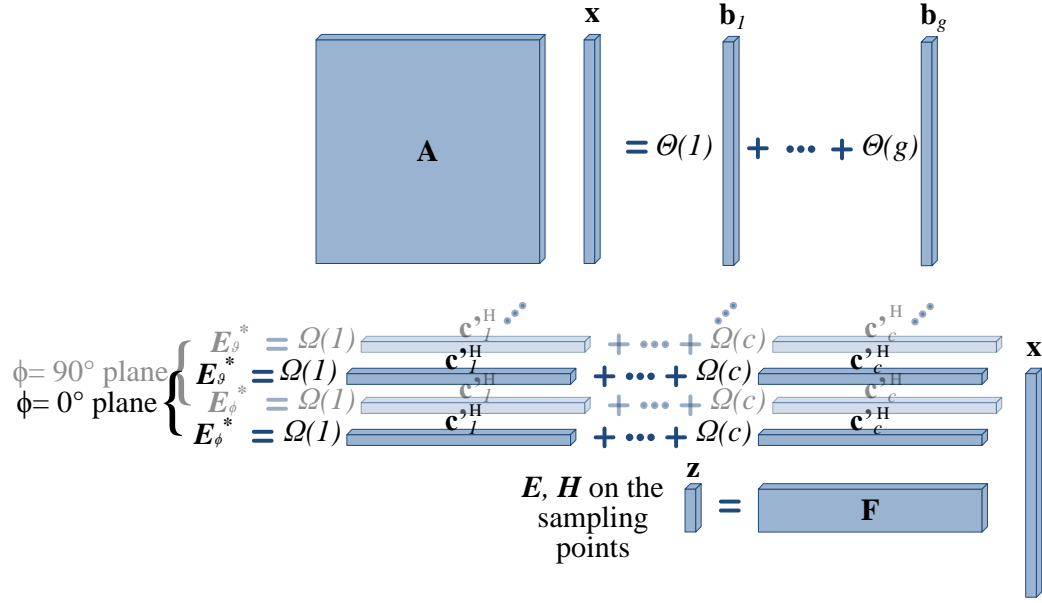


Figure 3.2: Schematic of the full radiation model.

We proceed applying the model order reduction definition (3.2.10) to the SISO-system of (3.3.14):

$$\begin{aligned}
 \tilde{\mathbf{A}} \tilde{\mathbf{x}} &= a_1 e^{-jk(x_1 \sin(\theta_x) + y_1 \sin(\theta_y))} \tilde{\mathbf{b}}_1 + \dots + a_g e^{-jk(x_g \sin(\theta_x) + y_g \sin(\theta_y))} \tilde{\mathbf{b}}_g \\
 y &= \left(\tilde{\mathbf{c}}_1^H + \dots + e^{jR\theta} \tilde{\mathbf{c}}_{R+1}^H + e^{-jR\theta} \tilde{\mathbf{c}}_{R+2}^H + \dots + e^{-j\theta} \tilde{\mathbf{c}}_{2R+1}^H \right) \tilde{\mathbf{x}}, \\
 \mathbf{z} &= \tilde{\mathbf{F}} \tilde{\mathbf{x}}.
 \end{aligned} \tag{3.3.15}$$

where the reduced order matrices of the system are $\tilde{\mathbf{A}} = \mathbf{W}^H \mathbf{A} \mathbf{V}$, $\tilde{\mathbf{b}}_i = \mathbf{W}^H \mathbf{b}_i$, $\tilde{\mathbf{c}}_j = \mathbf{V}^H \mathbf{c}_j$ or analogously, doing the transpose conjugate in both hand-sides, $\tilde{\mathbf{c}}_j^H = \mathbf{c}_j^H \mathbf{V}$, $\tilde{\mathbf{F}} = \mathbf{F} \mathbf{V}$, and $\mathbf{W}, \mathbf{V} \in \mathcal{X}^{N \times n}$, $n \ll N$, are respectively trial and test matrices we need to define in order to properly reduce the model.

3.4 Proper choice of the trial and test spaces

The model order reduction is mainly based on the fact that we approximate the solutions as $\mathbf{x} = \mathbf{V}\tilde{\mathbf{x}}$. If \mathbf{V} is an orthonormal basis, then $\tilde{\mathbf{x}} = \mathbf{V}^H \mathbf{x}$ and this means to test the solutions vector with an orthonormal basis, i.e. to provide a change of basis, and the testing returns the coefficients $\tilde{\mathbf{x}}$ for the expansion in terms of this new basis. Now, to choose \mathbf{V} , we need to think of what we are testing. The solutions vector is straightly related to the fields by the expansion (3.1.2). They are in fact the coefficients of the expansion in terms of orthogonal shape functions that approximates the near fields. Hence, from the results obtained from chapter 2, section 2.1.3, we can express the near fields pictures to span the testing space in terms of solutions obtained for various scan angles.

We need to collect several *solutions pictures* to span the scan angle space. Using the input system of (3.3.14), we compute α solutions \mathbf{x}_α for a set of α scan angles $(\theta_x, \theta_y)_\alpha$. The dimension of the scan angle space, as it was shown in chapter 2, depends on the array structure: the relative spacing and the number of radiating elements are the principal parameters. To compute the orthonormal vectors \mathbf{V} , either the SVD (right singular vectors) or the QR factorization (with \mathbf{Q} a matrix of orthonormal column vectors) [20] can be used, depending on the number of solutions pictures collected. In effect the complexity of an SVD is in the order of $2mn^2 + 11n^3$ while the QR factorization requires $2mn^2$, where m here corresponds to the DoFs while n is the number of scan angle pictures selected. For large n , the QR has a lower cost than the SVD, however with the QR we pay the price that the factorization is not always accurate [20].

The trial space can, in a first attempt, be the same as the testing space, leading to a Galerkin projection. Thus if we chose $\mathbf{W} = \mathbf{V}$, we may expect a total matching for the scan angles selected and for the remaining scan angles an approximated solution. Thus we can define the trial and test spaces as

$$\text{span} \left\{ \bigcup_{i=1}^{\alpha} \mathbf{x}_i(\theta_x, \theta_y) \right\} \subseteq \text{colsp} \{ \mathbf{V} \}, \quad (3.4.16)$$

$$\text{span} \left\{ \bigcup_{i=1}^{\alpha} \mathbf{x}_i(\theta_x, \theta_y) \right\} \subseteq \text{colsp} \{ \mathbf{W} \}. \quad (3.4.17)$$

Another possibility in the choice of \mathbf{W} is, according to [37], to use as trial space the solutions provided by the *dual problem* or *adjoint problem*. These solutions are given by the dual problem input system equation

$$\mathbf{A}^H \mathbf{z} = \sum_{j=1}^Q \Omega_j(\theta, \phi) \mathbf{c}'_j. \quad (3.4.18)$$

In a similar manner as done for the test space, we compute α solutions \mathbf{z}_α of (3.4.18) for a set of α look angles $(\theta, \phi)_\alpha$. An inconvenience resulting from the radiation model definition is that any matching we may achieve in the look angle with the dual problem approach is related to one cut-plane and one polarization. In effect, the vectors \mathbf{c}'_j are built for each polarization and for each cut-plane, and an expansion in the trial vectors derived from a look angle selection space for one polarization and one plane does not necessarily mean matching in the others. The scan and look angles selections spaces for the dual problem method can be defined as, respectively,

$$\text{span} \left\{ \bigcup_{i=1}^{\alpha} \mathbf{x}_i(\theta_x, \theta_y) \right\} \subseteq \text{colsp} \{ \mathbf{V} \}, \quad (3.4.19)$$

$$\text{span} \left\{ \bigcup_{i=1}^{\alpha} \mathbf{z}_i(\theta, \phi) \right\} \subseteq \text{colsp} \{ \mathbf{W} \}. \quad (3.4.20)$$

3.5 Numerical examples

The following examples have been realized combining several computational steps. First, the array structure is designed with HFFS, choosing the mesh density (h) and polynomial degree (p) parameters and individuating the resonant frequency of the single element. Then, the simulation is run with the internal solver, in order to provide data for comparison with our results. For proper comparison, the mesh and material data are extracted from the HFSS model, then the system matrices are built with the LTE³ proprietary code and loaded into Matlab. We now have the input system matrix \mathbf{A} and vectors $\mathbf{b}_i, 1 \leq i \leq g$. A direct solver optimized for sparse matrices

³ Lehrstuhl für Teoretische Elektrotechnik, Universität des Saarlandes, <http://www.lte.uni-saarland.de/>.

is used to solve the input system. Finally, with the N2F operator and the solutions-to-near-fields operator, together with the bounding surface informations, the entire full model is achieved and its reduced order version is computable. In this section, we will mainly discuss on the spanning spaces for projection, and the accuracy of the reduced order model respectively to the full model.

3.5.1 3 by 5 patch antennas array

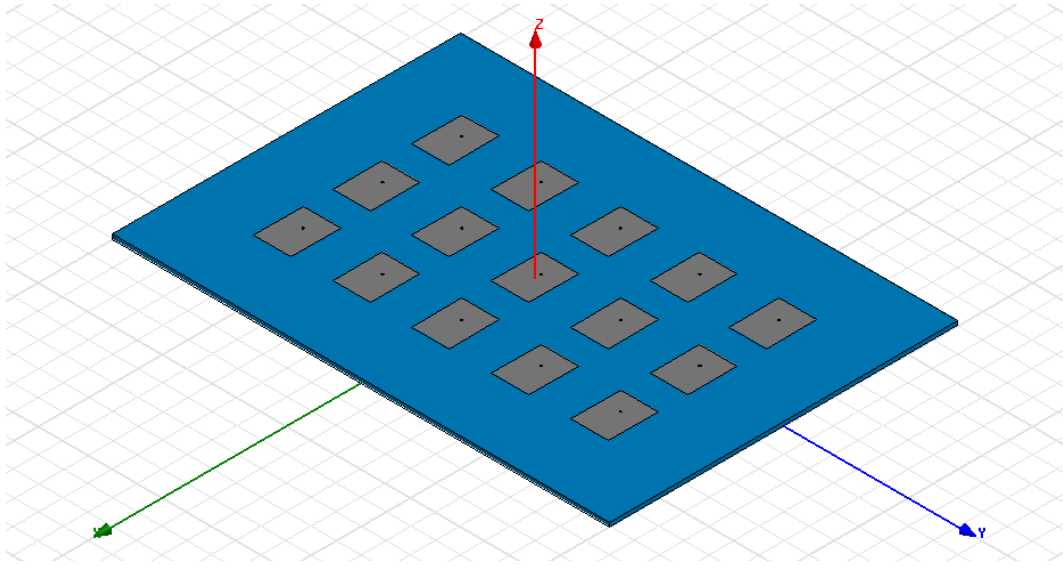


Figure 3.3: 3 by 5 patch antennas array fed by coaxial probes.

Figure 3.3 shows the an array of 3 by 5 patch antennas, equally spaced of $\lambda_0/2$, fed by 15 (g) individual coaxial wave ports. The metal materials, that is the ground plane, the patches, an the coaxial lines and probes [3] are set to be *perfect electrical conductors* (PEC). The coaxial dielectric, necessary to hold the core of the waveguide, is made of *Teflon* with $\epsilon_r = 2.1$ and its *dielectric loss tangent* is of $\delta = 0.001$. The dielectric substrate of the patches is of *Rogers RT/duroid 5880*, which has an $\epsilon_r = 2.2$ and a $\tan\delta = 0.0009$. The patches have been designed in order to be resonant at 2.35 GHz. The triangulated mesh, performed by the h -adaptive solver of HFSS, for a minimum $\Delta S = 0.05$ (scattering parameters at the ports) between the adaptive steps is shown in figures 3.4 and 3.5. The basis chosen are first order polynomials and the maximum tetrahedra dimension $h = \lambda/3$ (not $\lambda_0/3$, as in the dielectric media the

wavelength is shorter). The total computation time have been of about 58 minutes on a dual core, 2 GHz machine, with a maximum physical memory requirement of 1.5 GB.

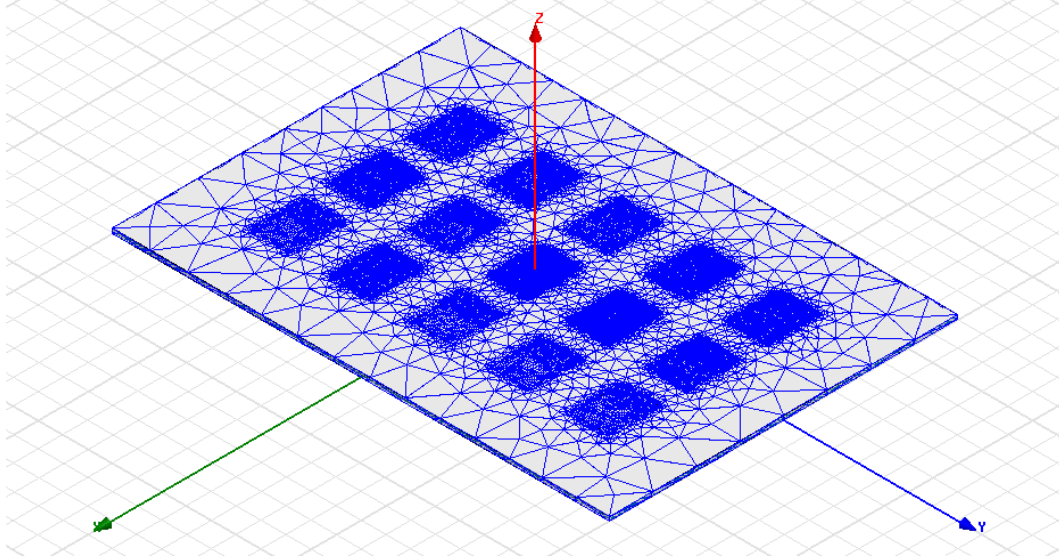


Figure 3.4: Resulting mesh of the 3 by 5 patch antennas array.

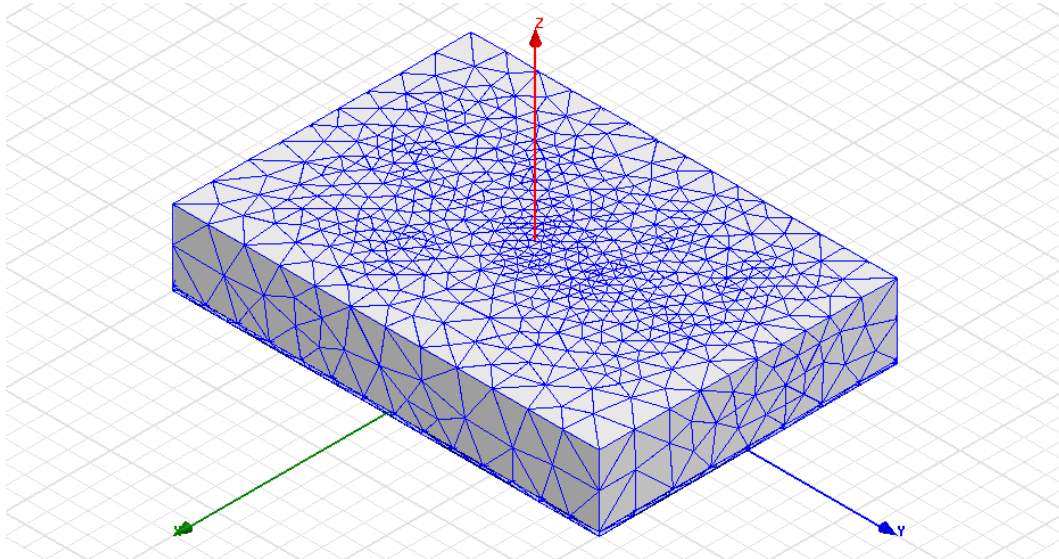


Figure 3.5: Resulting bounding box mesh of the 3 by 5 patch antennas array.

From these physical data, it has been possible to build the input system matrices of our model. Using the same interpolation basis, the resulting number of unknowns has been of 358 648. The total time required to build the full model is of about 45

minutes, and most of the time is used to build \mathbf{F} and the solutions of the input system matrix. Before we proceed generating the output system matrices, we must select the sampling points within the FEM domain. The sampling resolution we have chosen is of $\approx \lambda_0/10$, with $\lambda_0 = 12.76\text{cm}$ at 2.35 GHz. As we have seen in section 1.3.4, such a sampling resolution provides an error of about $\varepsilon_{[\lambda/10]} \approx 2 \cdot 10^{-3}$, which is adequate for our patterns computations. Further errors are introduced by the sampling operation in a FEM domain. In effect, the field within the discretized domain suffers of discontinuities at the interfaces between the elements, especially if the fields that are approximated vary rapidly. The h -adaptive meshing reduces this undesired behavior, but cannot eradicate it completely. Thus for better accuracy, a volume interpolation should be performed as proposed in [38], where the surface integrals are achieved through volume integrals within a thin layer that contains the fields sampling points. Also, the finite element method suffers of numerical dispersion in electrically large electromagnetic models [39], especially for high h (tetrahedra dimension) and low p (polynomial order). In our approach, we will consider these errors to be absent, remembering that they involve both the full and the reduced order models, and a comparison between these two models is unaffected by such errors. The near fields sampling grid is shown in figure 3.6. The ABCs are located $\approx 0.6\lambda_0$ from the center

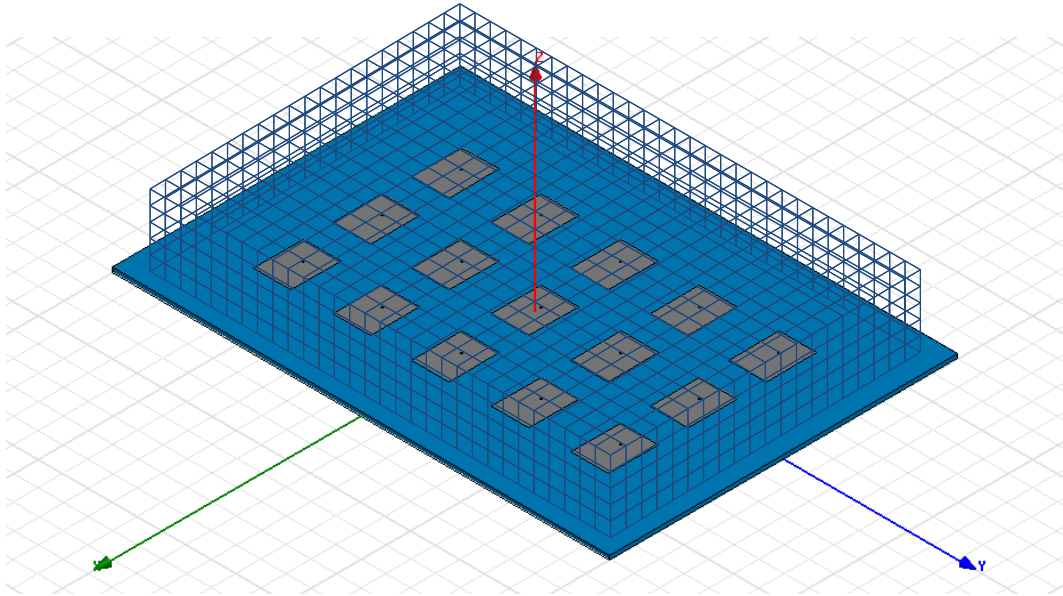


Figure 3.6: Sampling grid on the 3 by 5 patch antennas array.

Matrix	Memory [Bytes]
A	109 231 240
$\text{span}\{\mathbf{b}_1, \dots, \mathbf{b}_{15}\}$	488
$\text{span}\{\mathbf{x}_1, \dots, \mathbf{x}_{15}\}$	86 075 520
XZ plane : $\text{span}\{\mathbf{c}'_1, \dots, \mathbf{c}'_{21}\}_\theta + \text{span}\{\mathbf{c}'_1, \dots, \mathbf{c}'_{21}\}_\phi$	9 037 568
YZ plane : $\text{span}\{\mathbf{c}'_1, \dots, \mathbf{c}'_{21}\}_\theta + \text{span}\{\mathbf{c}'_1, \dots, \mathbf{c}'_{21}\}_\phi$	9 037 568
Total	$\approx 221\text{MB}$

Table 3.1: Memory requirements for the full radiation model.

of the patches and the sampling grid at $\approx \lambda_0/2$. The bottom face of the parallelepiped have been neglected, as the fields on the PEC ground plane are known to be null. The pattern computed by HFSS is shown in figure 3.7. The output system matrices, ac-

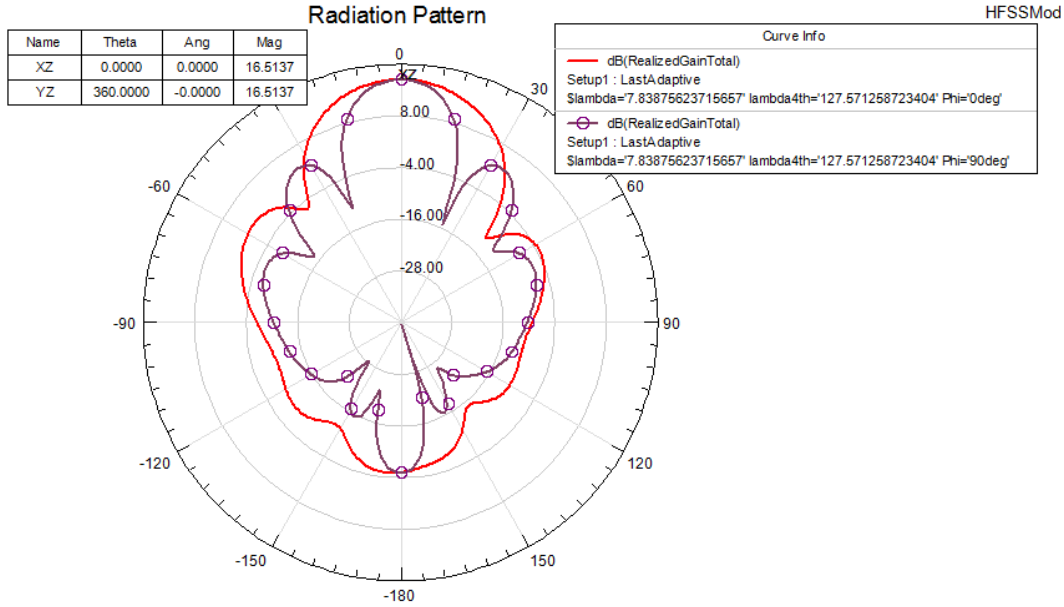


Figure 3.7: Broadside pattern of the 3 by 5 patch antennas array computed by HFSS.

ording to the results of figure 2.32, can be built with a DFT-truncation retaining only 21 coefficients. Hence, we obtain an output matrix $\text{colsp}\{\mathbf{c}'_j\} \in \mathbb{C}^{358648 \times 21}, 1 \leq j \leq 21$ for each polarization, and the planes of pattern computation will be the XZ and YZ cut planes. This completes our radiation model. The total memory employed, considering double precision, is detailed in table 3.1. As most of the matrices are sparse, the only real contributions are given by the FEM system matrix and the solution vectors which are not sparse. Thanks to the DFT truncation and to the few number of

sampling points (1100), the output system matrix is very low memory consuming, and building a matrix in order to compute the pattern on 5000 points within $[0^\circ, 360^\circ]$ requires only 1.6 MB more. Notice that this matrix is the same for all the planes, thus has to be computed only once.

We can now build our reduced order model. Before we proceed with Galerkin projection method, we may discuss on the array configuration and how should be the near fields scanning space. According to the results of section 2.1.3, the rank for a scanning along the x direction, as we have 3 patches spaced of $\lambda_0/2$, should be of 3. Analogously, along the y direction, as we have 5 patches spaced of $\lambda_0/2$, the rank should be of 5. Thus, until we use 3 or 5 solutions pictures, for each cut-plane respectively, we expect the error to be non negligible.

To check the functionality of the ROM, we have performed a Galerkin projection selecting as scan angle the broadside direction. The resulting pattern is shown in figure 3.8. The total relative error introduced by the model order reduction is numerically null ($3.395 \cdot 10^{-13}$). There are some differences between the pattern computed by HFSS and ours. This is mainly due to the fact the our sampling points are distant from the radiation boundaries from which HFSS computes the far fields patterns imposing the ABCs. In effect, as we chose sampling points slightly distant from the radiation boundaries (1mm close to the surface), we notice a higher similitude of our pattern with HFSS's one, as shown in figure 3.9. However, the main purpose of this thesis is to discuss the application of the projection-based model order reductions on phased arrays, with an emphasis on the reduced order dimension. Hence, we proceed working on the first near fields sampling points selection, without carrying on whether HFSS or our implementation is more accurate.

3.5.1.1 Galerkin projection method on cut planes

We have chosen the beamsteering angles to be along the y direction in which we have 5 groups of 3 antennas excited with a linear phase, each group having the same phase. The spanning scan angles are chosen equidistant in the range of $\theta_y \in [0^\circ, 90^\circ]$.

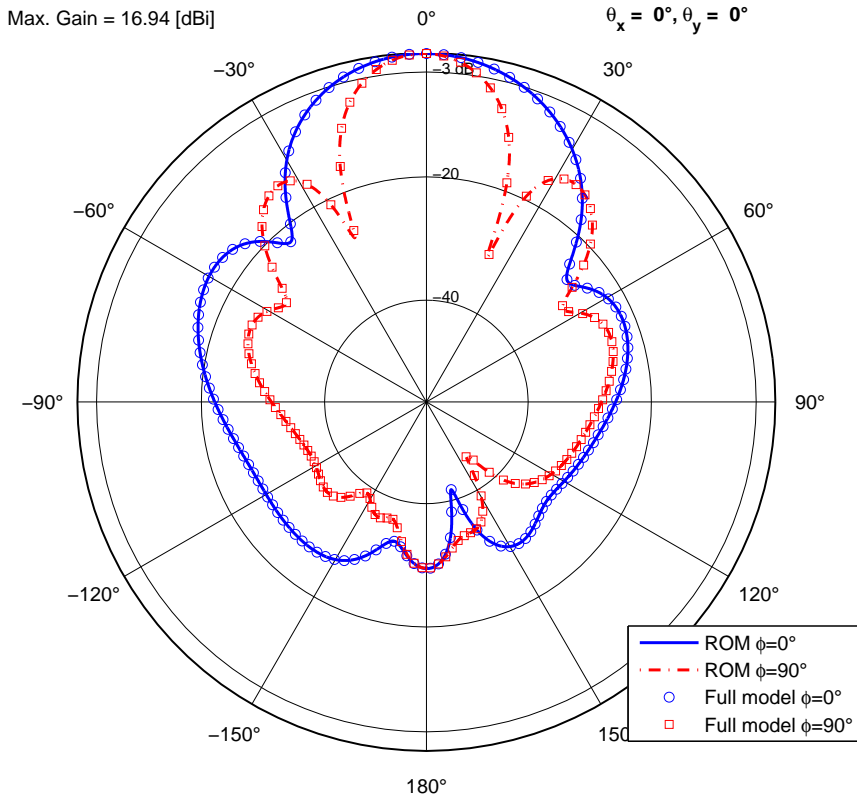


Figure 3.8: Total far fields pattern computed in the broadside direction by the full model and the ROM of the 3 by 5 patch antennas array.

Then the error is computed for 21 tested scan angles chosen in the same range, returning for each spanning space dimension the average relative error between the full model and the MOR computed far fields detectors on both XZ and YZ planes. The results are shown in figure 3.10. The average error value computed with a scan angle space of dimension 4 is of 0.2189. This is still too high for accurate computations, and a steered patterns in that conditions are shown in figures 3.11 and 3.12. As we expected from conclusion 4, the pattern next to end fire is more accurate than that close to broadside. Furthermore, this behavior should be enhanced by the element factor allowing us to choose spanning angles much closer to the broadside direction. Now, we conclude discussing on the error we obtain with the ROM of order 5: it is null for all steering angles chosen along the y direction. This is the most interesting information achieved from the model order reduction of phased arrays. The final model is constituted of the following full (not sparse) matrices : $\tilde{\mathbf{A}} \in \mathbb{C}^{5 \times 5}$, $\text{colsp}\{\tilde{\mathbf{b}}_1, \dots, \tilde{\mathbf{b}}_{15}\} \in \mathbb{C}^{5 \times 15}$,

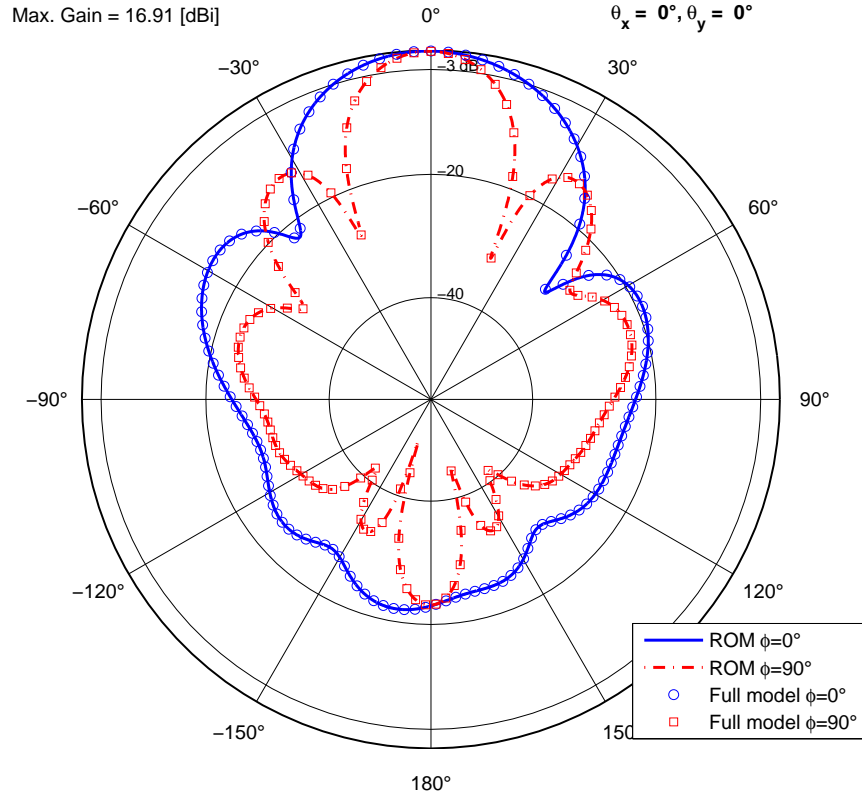


Figure 3.9: Broadside pattern computed from a surface 1mm next to the radiation boundaries.

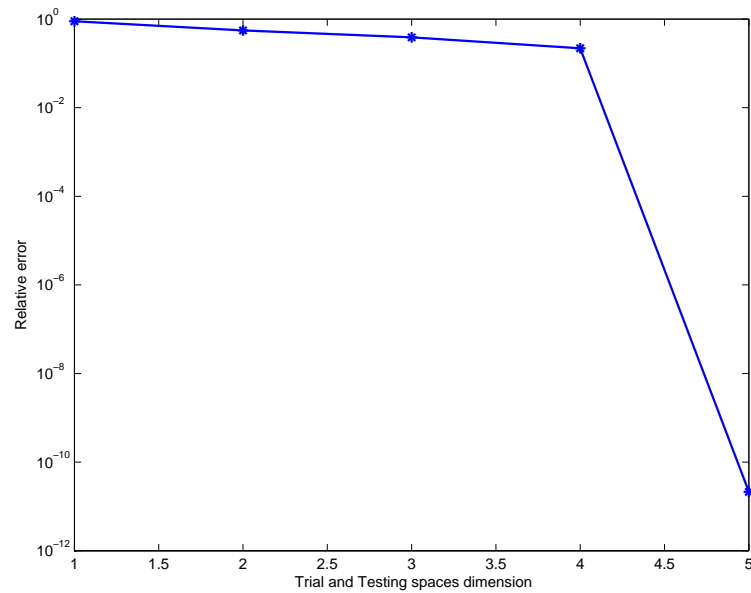


Figure 3.10: Relative error in the far fields detectors for the full model and those for the reduced model.

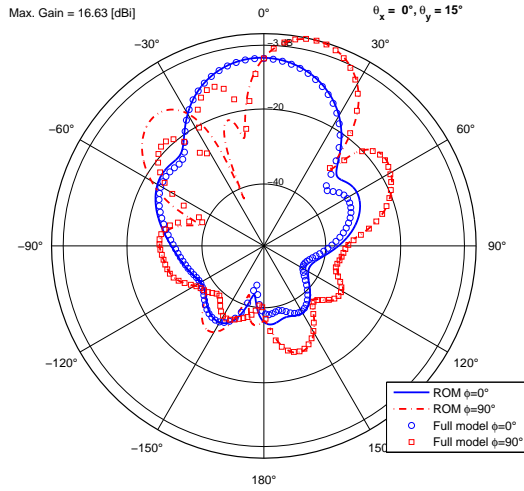


Figure 3.11: Steered pattern close to broad side computed from a ROM of order 4.

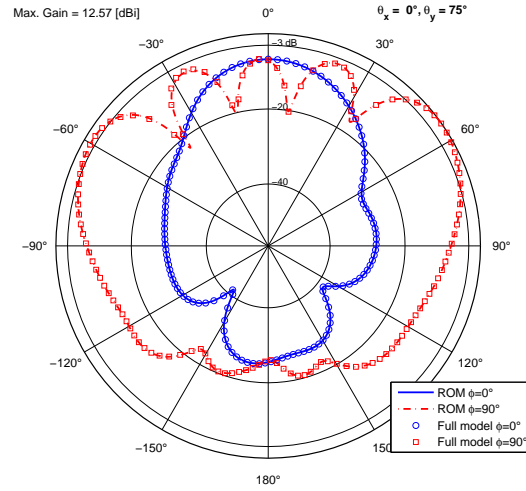


Figure 3.12: Steered pattern close to end fire computed from a ROM of order 4.

$\text{colsp}\{\tilde{\mathbf{c}}'_1, \dots, \tilde{\mathbf{c}}'_{21}\}_\theta, \text{colsp}\{\tilde{\mathbf{c}}'_1, \dots, \tilde{\mathbf{c}}'_{21}\}_\phi \in \mathbb{C}^{5 \times 21}$ for each cut-plane, and $\tilde{\mathbf{F}} \in \mathbb{C}^{1100 \times 5}$, necessary in order to compute the radiated power from $p = 1100$ near fields sampling points. 420 kB are occupied by this ROM, and we only need to supply the scan angles $\Theta_i(0^\circ, \theta_\gamma)$ and the output trigonometric polynomials values $\Omega_j(\theta, \phi = 0^\circ, 90^\circ)$, the latter depending on the required pattern resolution (we used a $\Delta\theta$ of 0.036° building a matrix of about 1.6 MB in this case), to compute the cut-planes patterns. The error is now pending on the sampling resolution of $\lambda/10$, which has been considered to provide accurate patterns.

3.5.1.2 Dual space projection method on cut planes

We proceed illustrating the effectiveness of the dual problem based projections. We need to compute further 21 solutions from the output vectors we dispose. We have chosen to match the look angles in the θ polarization, using the output matrix $\text{colsp}\{\mathbf{c}'_1, \dots, \mathbf{c}'_{21}\}_\theta$, with matching look angles in 89.7297° , 179.8198° and 269.9099° and the test space is matched in 0° , 45° and 90° to build a ROM of order 3. As 11° is not an interpolation angle for both the test and trial spaces, we use that scan angle to compute the error. Figures 3.13 and 3.14 show that the pattern is matched (null error) in the look angles selected for the trial space in the XZ plane (dash-dotted ver-

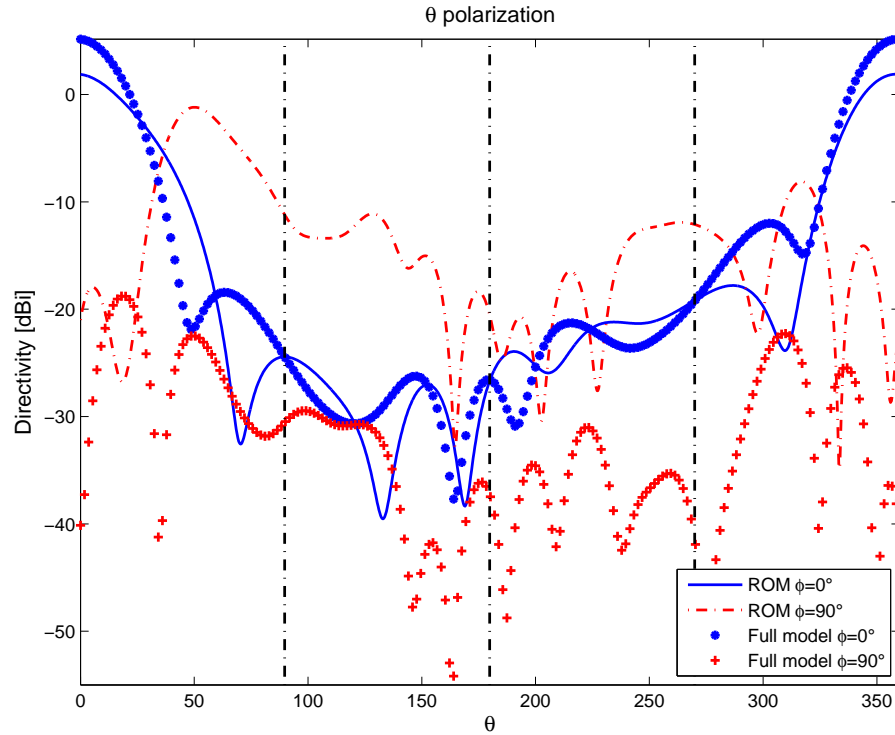


Figure 3.13: θ polarization pattern for the full model and those for the reduced model of order 3 with look angle trial space.

tical lines) only for the θ polarization on the XZ plane, while the whole pattern error remains very high. We achieve only a local matching on the selected look angles and this is a result we could expect from the definition of the look angle. While the scan angle contains informations on the whole near fields on the bounding surface, the look angle, being the result of a near-to-far transformation, does not maintain any information on the near fields, hence on the total pattern. Furthermore, as the trial and the test spaces must have equal dimensions to allow the inversion of $\tilde{\mathbf{A}}$ during the solution of the reduced order input system, it will never be possible to cover the entire pattern matching the look angle space. Another non negligible negative point is associated to the fact that the number of coefficients retained with the DFT-truncation, considering all the polarizations and all the cut-planes, is typically higher than the number of scan angles that span the trial space, leading in further computations that may not improve the accuracy.

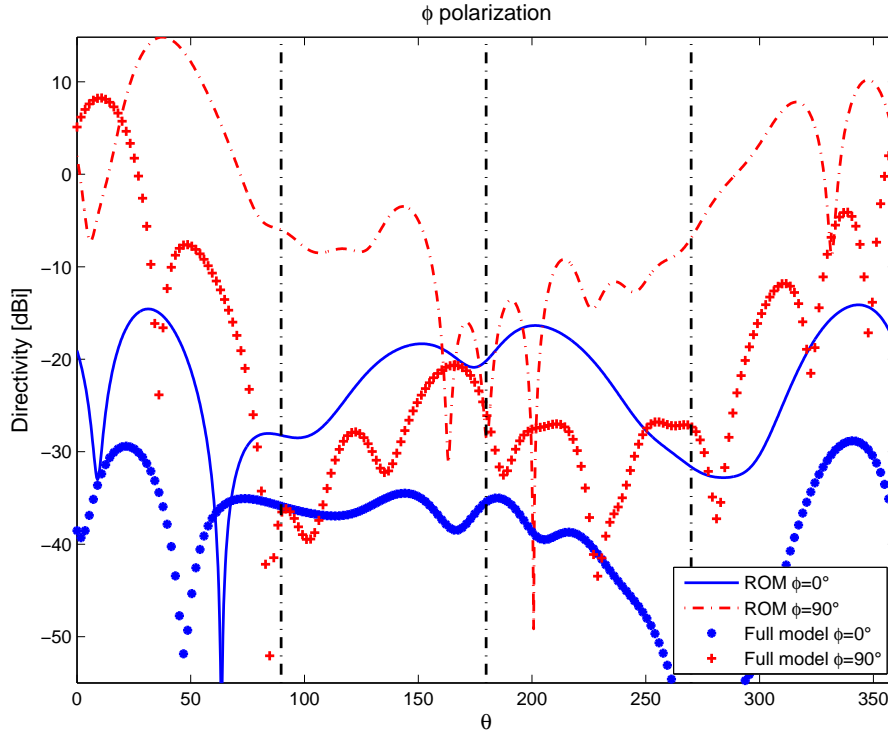


Figure 3.14: ϕ polarization pattern for the full model and those for the reduced model of order 3 with look angle trial space.

3.5.1.3 Galerkin projections for tridimensional pattern

It is our interest to see now whether the ROM behaves if we want to scan the whole tridimensional space. In a first attempt, we build the scan angle spaces from scan angles in both x and y directions, that is with 3 angles ($\theta_x, \theta_y = 0^\circ$) and 5 angles in ($\theta_x = 0^\circ, \theta_y$), with $\theta_x, \theta_y \in [0^\circ, 90^\circ]$. The 8 selected angles, chosen properly in order to avoid the redundancy in the broadside direction, and the tested scan angles in the $\phi = 45^\circ$ are shown in figure 3.15. The resulting error, illustrated in figure 3.16, shows that we cannot consider the oblique scan angles as a linear combination of the space spanned by scan angles in the x and y beamsteering directions: the error never drops below 10^{-2} .

From this results we understand that we need to select more vectors, with scan angles in the entire septentrional hemisphere. The first idea that comes to our minds is to employ a spiraling helicoidal trajectory to select the scan angles for the test space

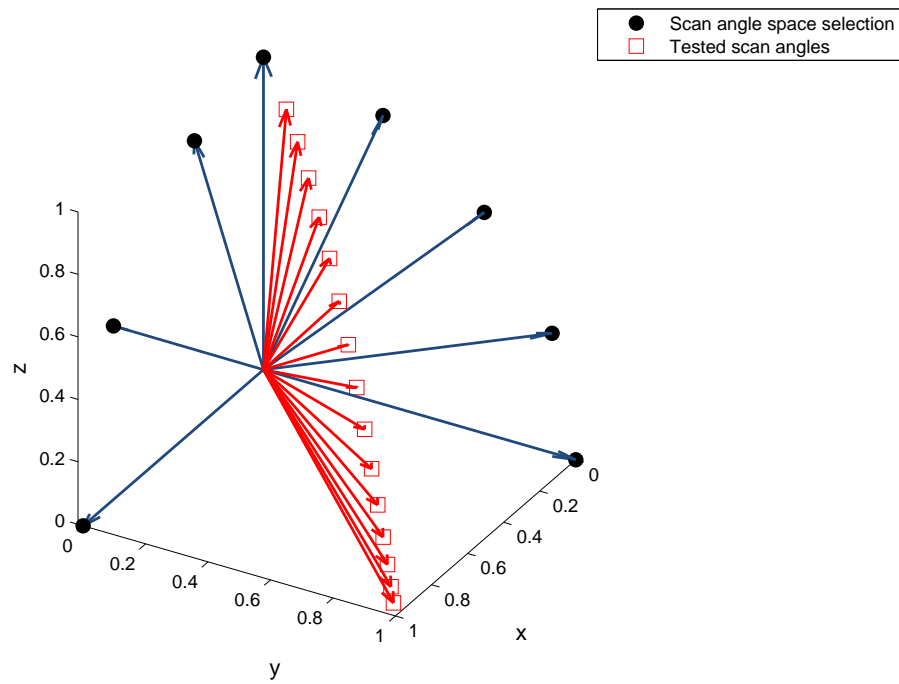


Figure 3.15: Scan angle selected for the projection space and tested angles (unit vectors of the directions).

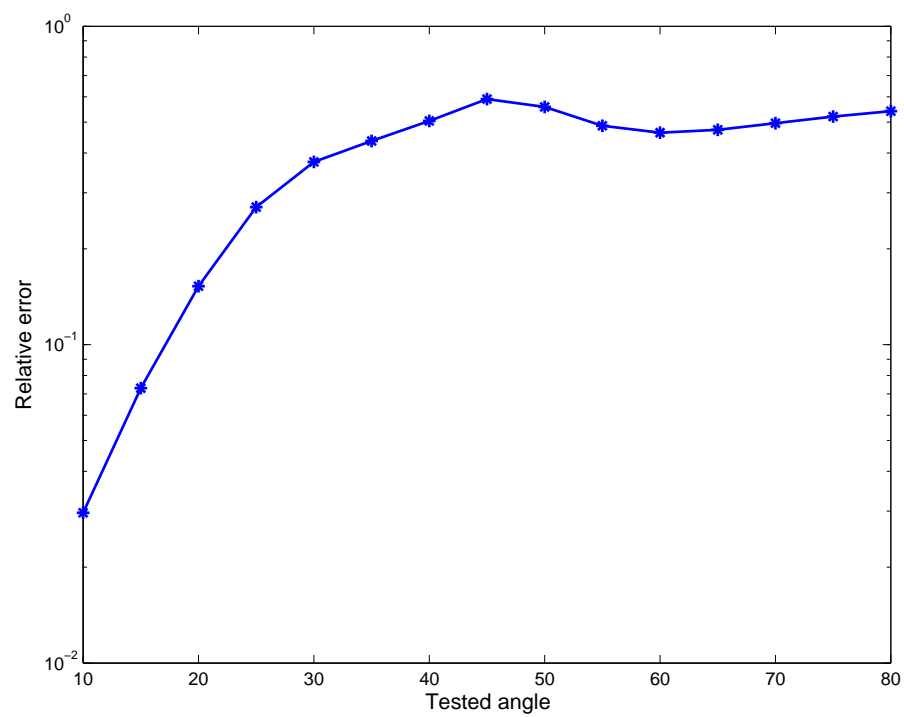


Figure 3.16: Error resulting from an oblique scan angle testing.

and an opposite one to test the quality of the space spanned. Those trajectories are depicted in figure 3.17. We proceed computing the errors increasing the size of the

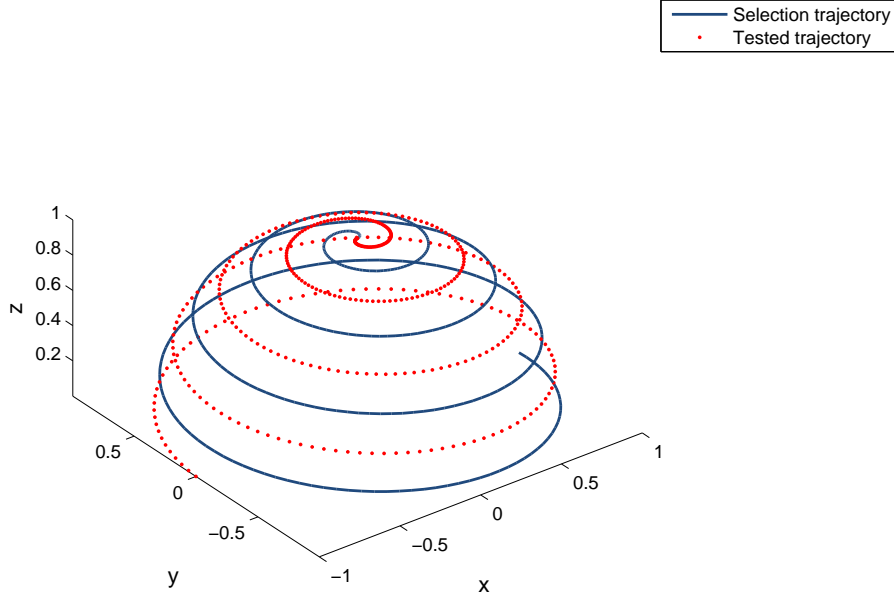


Figure 3.17: Scan angles selection trajectory and error test scan angles trajectory.

scan angle space, the results are shown in figure 3.18. First we notice that the error becomes numerically null at 15 scan angles on the selection trajectory, that is the total number of array antennas. The error suddenly becomes non null with 17 scan angles. This is mainly due, as we can see in figure 3.19, to the spherical pyramid edge sampling condition we have achieved with 17 scan angles. The resulting vectors are linearly dependent, located only on x and y directions, hence the full rank of 15 is not attained. We can conclude that

Conclusion 7 *The number of scan angles required in order to correctly approximate a tridimensional steering operation all over an hemisphere, for $\lambda/2$ spaced array elements, is of the total number of radiating array elements. Furthermore, the scan angles must be chosen properly, in order to obtain a set of linearly independent vectors. These can be selected along a spiraling helicoidal trajectory over the septentrional hemisphere of a sphere aligned with the center of the array.*

Finally, we can compute the radiation solid with the ROM of order 15. To scan

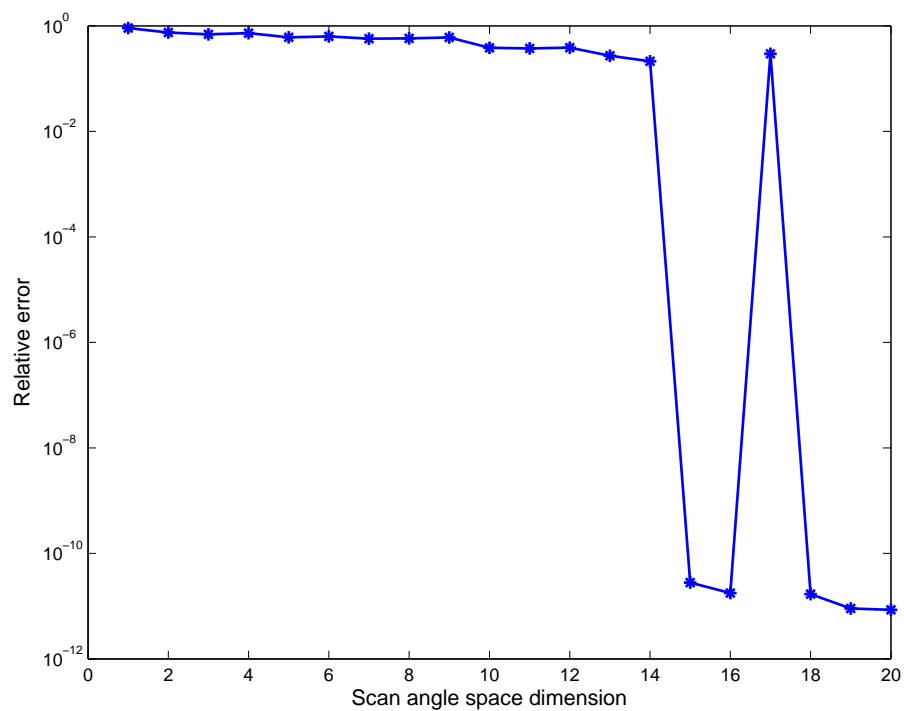


Figure 3.18: Average error on the test scan angles patterns with a space spanned with a spiraling helicoidal trajectory.

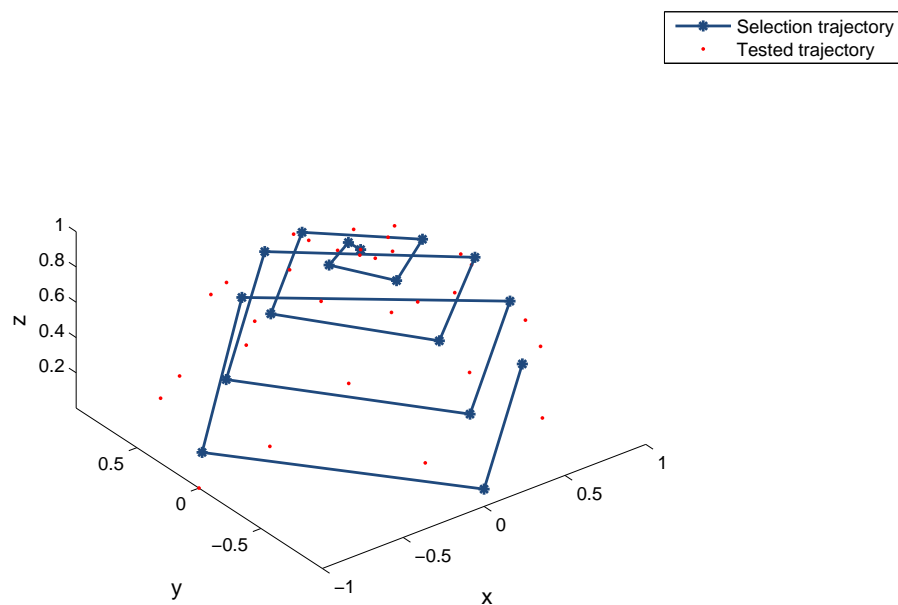


Figure 3.19: 17 scan angles selection trajectory and 31 error test scan angles trajectory.

the whole space, we have chosen cut-planes in the range $\phi \in [0^\circ, 180^\circ)$ with a $\Delta\phi \approx 3^\circ$, while the sampled trigonometric polynomials matrix \mathbf{t} covers the range $[0^\circ, 360^\circ)$. The total ROM occupies only 3.2 MB of memory, and each new scan angle pattern is computed with the sampling resolution accuracy of $\approx 2 \cdot 10^{-3}$ in about 0.07 seconds on a dual core 2 GHz machine, while the full model requires 0.55 seconds for each scan angle

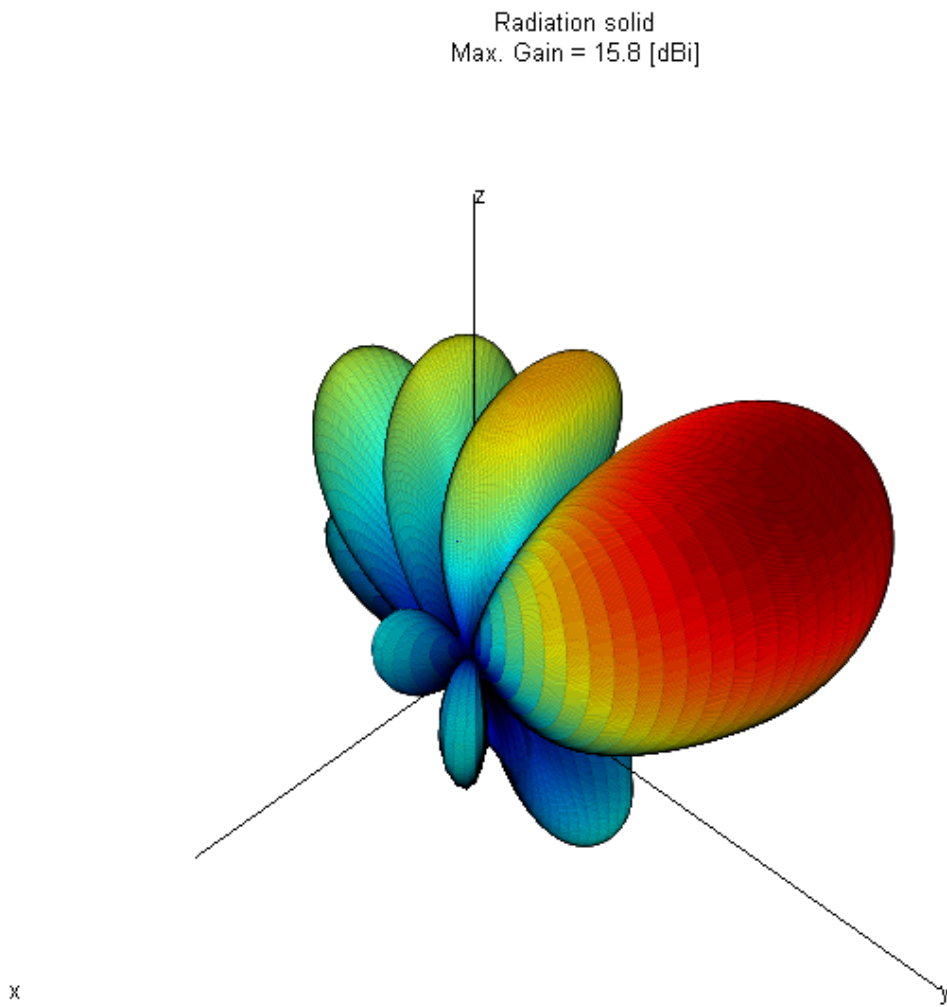


Figure 3.20: Radiation solid scanning in $(\theta_x = -10^\circ, \theta_y = 45^\circ)$ computed by the reduced order model.

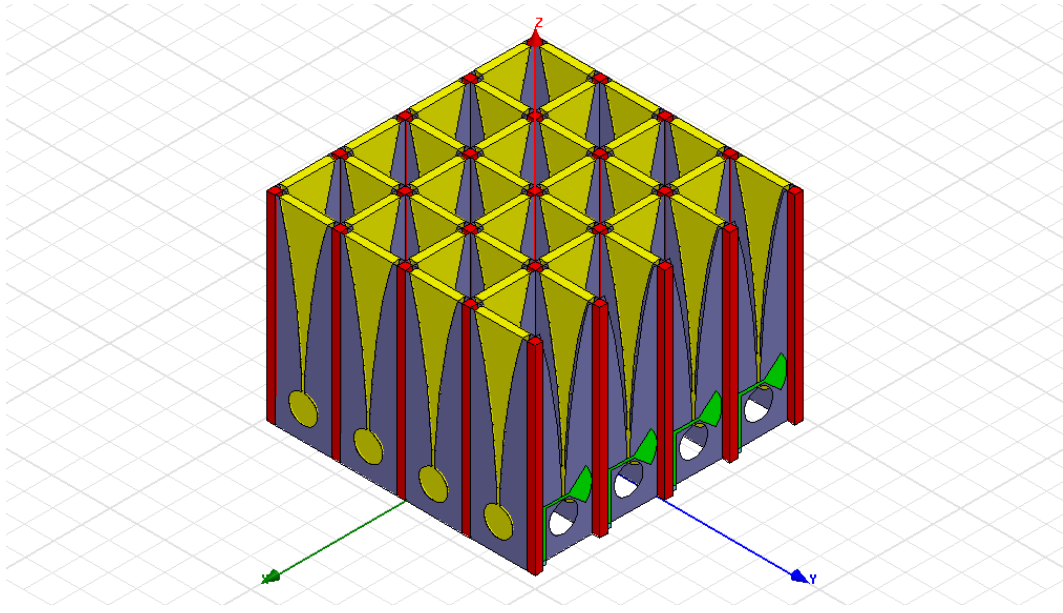


Figure 3.21: Array of tapered slot antennas equally spaced of $\approx \lambda_0/5$.

3.5.2 40 dual-polarized tapered slot antennas

To emphasize the importance of the relative spacing between the radiating elements, we now illustrate the results of the model order reduction applied to the array of in figure 3.21. It is a dual polarized array of 40 tapered slot antennas (TSAs), also called *Vivaldi* antennas, that is actually built superposing orthogonally two arrays (each ideally linearly polarized) of 4 by 5 of TSAs. The model has been designed according to [40]. Notice that in figure 3.21, the front x directed row of TSAs have some dielectrics parts hidden in order to show the feeding stripline, with radial stub termination. The radiating slots are tapered exponentially, while short circuited at the non radiating side. With the given geometrical parameters, the TSA achieves a bandwidth, in terms of *Voltage Standing Wave Ratio* (VSWR) below 2, of about 5.5 GHz when steering in the broadside direction, centered at 4 GHz. We have chosen to build the radiation model at 3 GHz, for which the spacing between the TSAs, being of 2cm, is of $\approx \lambda_0/5$. The near fields sampling resolution is chosen to be of $\lambda_0/10$ and the number of coefficients retained in the DFT-truncation is of 51. To build the ROM with Galerkin projections, the steering direction chosen is x , where we have a maximum of 9 groups radiating elements, 5 being cross polarized. From the singular values of figure 3.22,

we realize that the rank of the scan angle space in that direction is of 9 (for scan angles selected equidistantly in the range $\theta_x \in [0^\circ, 90^\circ]$, $\theta_y = 0^\circ$). The singular values are de-

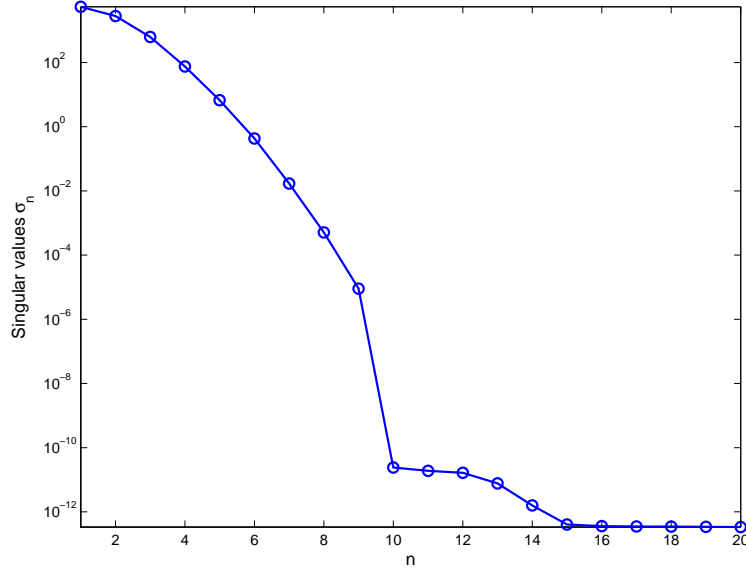


Figure 3.22: Singular values of the TSAs array steered in the x direction.

creasing rapidly even before we attain the numerical rank. As we have seen in figure 2.1, the far fields detectors error was low even before the number of vectors arrived to the number of radiating elements. Thus we expect the ROM to require an order lower than 9 while keeping the sampling resolution error. As we can see in figure 3.23, the maximum ROM approximation error, attained near the broadside direction (figure 3.24), is slightly lower than the near fields sampling resolution error once we use 5 spanning scan angles, and using 6 out of 9 renders the approximation error irrelevant to the radiation model. Figure 3.24 reports the error for several tested angles, the scan angles selected to span the projection space being of $\theta_x = 0^\circ, 22.5^\circ, 45^\circ, 67.5^\circ, 90^\circ$. This results in the fact we need much less than 81 spanning scan angles to scan the whole septentrional hemisphere. Figures 3.25 and 3.26 show that only 40 vectors (out of 81 that may be required for $\lambda/2$ of relative spacing between the antennas) are required to build an accurate ROM for tridimensional beamsteering of the tapered slot antennas array designed.

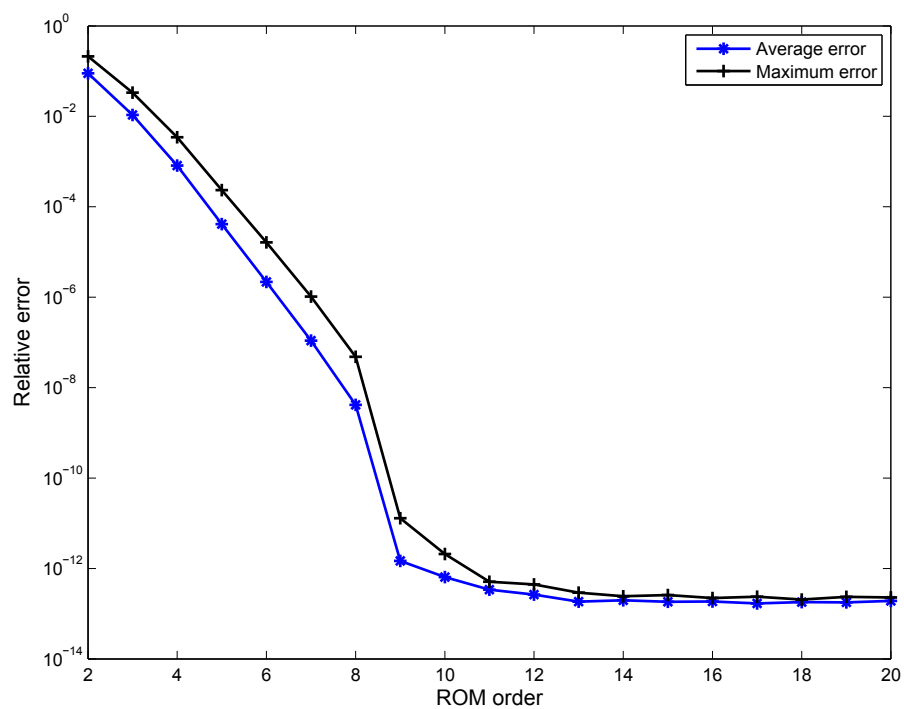


Figure 3.23: Error for several orders of the TSAs array ROM.

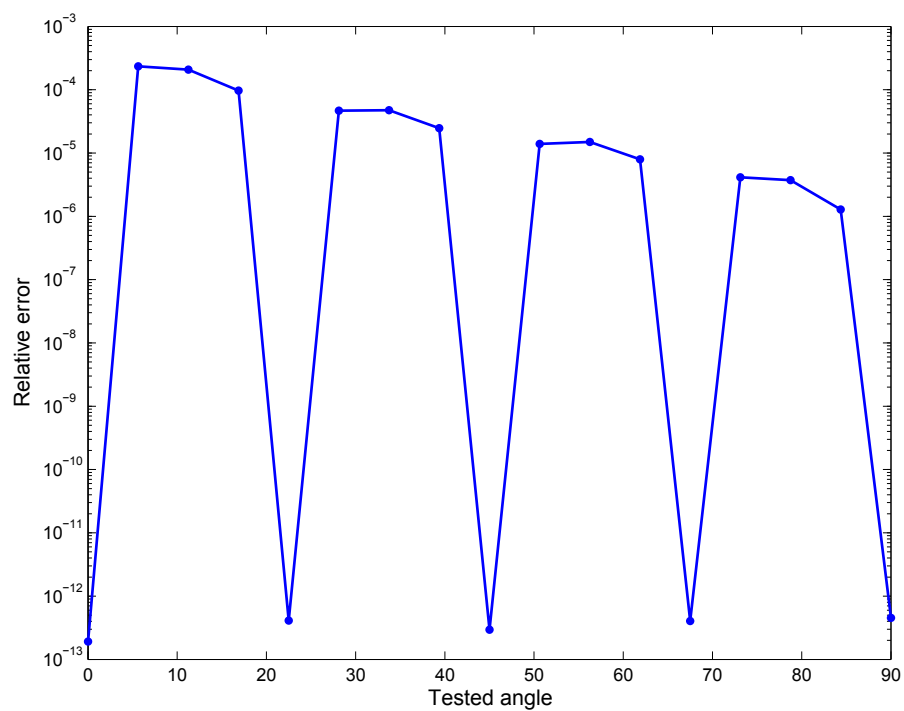


Figure 3.24: Error introduced by a ROM of order 5 for several tested angles.

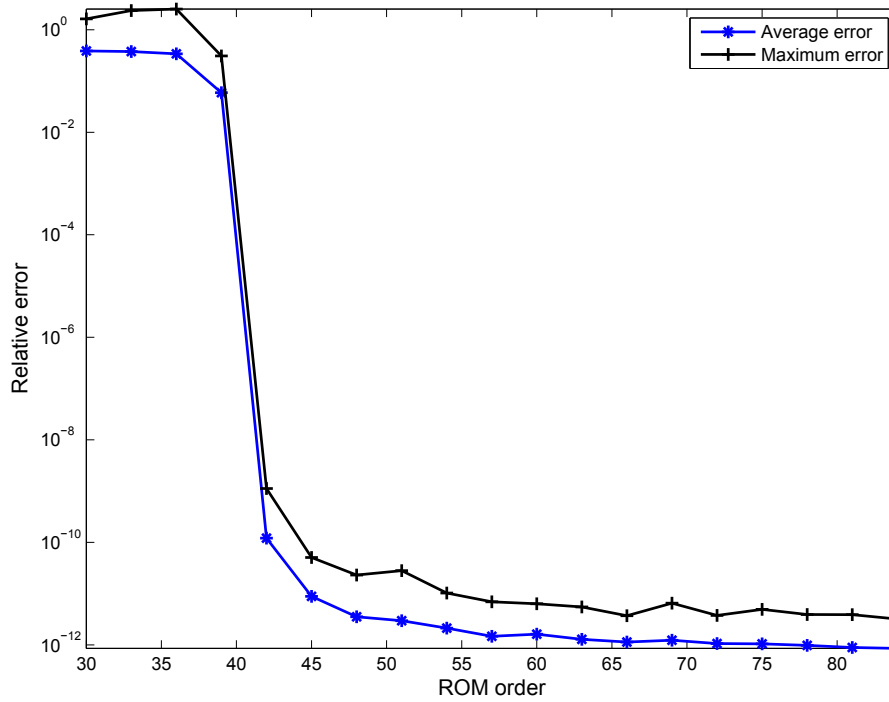


Figure 3.25: Error for several orders of ROM able to scan the whole tridimensional space.

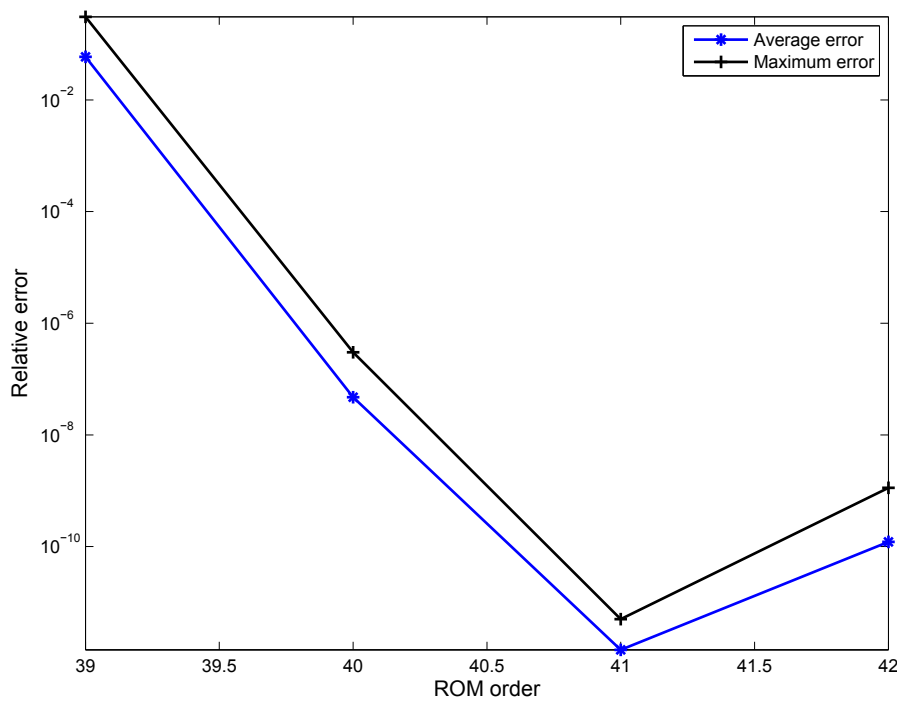


Figure 3.26: Error for 39, 40, 41 and 42 ROM orders.

CONCLUSIONS

The model order reduction techniques have demonstrated in the last two decades to be very promising in the full-wave analysis of electromagnetic structures. The most interesting issues arise from the fact it is possible to achieve, with less computational requirements, the response of the electromagnetic structure in front of a parameter sweep [26], and even multiple parameters sweeps [33]. Well established methodologies for computing fast frequency sweeps are nowadays available. For example, the *Adaptive Lanczos-Padé Sweep* (ALPS) [36] is implemented in HFSS, confirming its robust formulation. In scattering problems [37], the incidence angles of plane waves have been parameterized in order to achieve the radar cross section of a scatterer through model order reduction.

The fundamental idea on which the projection-based model order reductions is based is the possibility to project a full order model onto a low dimensional parameterized subspace of appropriate global shape functions, keeping the necessary information associated to that subspace. In this thesis, it has been shown that, parameterizing the input and output system vectors of the radiation model of a phased array in the scan and look angles then projecting the system onto an appropriately chosen scan angle subspace, highly efficient computations of the far fields pattern in front of a beam steering process can be achieved. The technique employed lead to reduced order models of dimensions comparable to the number of radiating elements that compose the array, where the original model, due to the high accuracy of the full-wave analysis, was several orders of magnitude higher.

According to [33], it is possible to include further polynomial parameterizations in

finite element models of microwave structures. Taking into account the frequency response of the radiating elements, and including variability of the dielectric and eventually ferroelectric materials properties by appropriate polynomial parameterization of the system matrices, may lead to multivariate reduced order models of phased arrays capable to give to the designer precious informations on the tolerances associated to physical realization.

The significant computational timings reduction, typically of several orders compared to the full model parameter sweep requirements [26], may allow fast optimization processes, either with deterministic algorithms or non-deterministic ones like the genetic algorithms, thus improving significantly the overall design process.

REFERENCES

- [1] C. A. Balanis, *Antenna Theory, Analysis and Design*, 2nd ed., John Wiley & Sons Inc., 1997. 1, 42
- [2] W. L. Stutzman, G. A. Thiele, *Antenna Theory and Design*, John Wiley & Sons Inc., 1981. 26, 29, 54
- [3] T. A. Milligan, *Modern Antenna Design*, 2nd ed., IEEE Press, Wiley-Interscience, 2005. 38, 42, 90, 95
- [4] S. Selleri, *Elementi di Teoria degli Array*, Pitagora Editrice Bologna, 2001. 25, 90
- [5] R. J. Mailloux, *Phased Array Antenna Handbook*, 2nd ed., Artech House Inc., 2005. 1
- [6] A. E. Zooghby, *Smart Antenna Engineering*, Mobile Communications series, Artech House Inc., 2005. 1
- [7] E. J. Rothwell, M. J. Cloud, *Electromagnetics*, CRC Press LLC, 2001. 6, 10, 11, 12, 15, 17, 18, 19, 42
- [8] S. J. Orfanidis, *Electromagnetic Waves and Antennas*, Rutgers University, 2008, available at www.ece.rutgers.edu/~orfanidi/ewa. 16, 19
- [9] J. A. Stratton, *Electromagnetic Theory*, McGraw-Hill Book Compagny Inc., 1941. 18
- [10] J. G. Van Bladel, *Electromagnetic Fields*, 2nd ed., IEEE Press, Wiley-Interscience, 2007. 12

- [11] J. G. Van Bladel, *Singular Electromagnetic Fields and Sources*, Oxford University Press, 1991. 39
- [12] A. Bondeson, T. Rylander, P. Ingelström, *Computational Electromagnetics*, Springer, 2005 25
- [13] V. Thomée , *Galerkin Finite Element Methods for Parabolic Problems*, 2nd ed., Springer, 2006. 50, 84
- [14] A. Chatterjee, *Introduction to the Proper Orthogonal Decomposition*, Current Science, Vol. 78, No. 7, 10 April 2000. 50
- [15] P. R. Halmos, *Measure Theory*, Springer-Verlag, 2000. 50
- [16] W. Rudin, *Functional Analysis*, McGraw-Hill Book Compagny Inc., 1973. 67
- [17] M. Giaquinta, G. Modica, *Mathematical Analysis, Linear and Metric Structures and Continuity*, Birkhäuser, 2007. 27, 67
- [18] Y. Saad, *Iterative Methods for Sparse Linear Systems*, University of Minnesota, 2nd ed., 2000, available at <http://www-users.cs.umn.edu/~saad/>. 52
- [19] S. J. Orfanidis, *SVD, PCA, KLT, CCA, and All That*, Rutgers University, 2007, available at www.ece.rutgers.edu/~orfanidi/ece525/svd.pdf.
- [20] L. N. Trefethen, D. Bau, *Numerical Linear Algebra*, SIAM, 1997. 51, 52, 93
- [21] A. C. Antoulas, *Approximation of Large-Scale Dynamical Systems*, SIAM, Advances in Design and Control, 2005. 51, 54
- [22] D.B.P. Huynh, A.T. Pater, *Reduced basis approximation and a posteriori error estimates for stress intensity factors*, International Journal for Numerical Methods in Engineering, 72 (10): 1219-1259, 2007, available at <http://augustine.mit.edu/methodology/papers/atpIJNMEpreprint.pdf>. 91
- [23] M. Barrault, Y. Maday, N. C. Nguyen, A. T. Patera, *An “empirical interpolation” method: application to efficient reduced-basis discretization of partial differen-*

- tial equations*, Académie des Sciences, Elsevier SAS, 2004, available at <http://augustine.mit.edu/methodology/papers/atpCRAS2004.pdf>.
- [24] G. Rozza, D.B.P. Huynh, A.T. Patera *Reduced Basis Approximation and a Posteriori Error Estimation for Affinely Parametrized Elliptic Coercive Partial Differential Equations*, Archives of Computational Methods in Engineering, vol. 15, num. 3, pp. 229-275, 2008, available at <http://www.springerlink.com/content/vur203773327381j/>.
- [25] G. Guarnieri, G. Pelosi, L. Rossi and S. Selleri *FE-DD Based Permittivity Tolerance Analysis in Microwave Waveguide Filters* COMPEL, Vol. 27 No. 6, pp. 1236-1248, 2008, available at <http://dx.doi.org/10.1108/03321640810905729.83>
- [26] S. Selleri, O. Farle, G. Guarnieri, M. Losch, G. Pelosi, R. Dyczij-Edlinger, *A Combined Domain Decomposition - Model Order Reduction Technique for Fast Finite Element Parametric Sweeps* IEEE Antennas and Propagation Society International Symposium, 2008, available at <http://ieeexplore.ieee.org/stamp/stamp.jsp?tp=&arnumber=4619422>. 2, 83, 113, 114
- [27] F. Bertazzi, O. A. Peverini, M. Goano, G. Ghione, R. Orta, R. Tascone, *A Fast Reduced-Order Model for the Full-Wave FEM Analysis of Lossy Inhomogeneous Anisotropic Waveguides*, IEEE Transactions on Microwave Theory and Techniques, Vol. 50, No. 9, Sept 2002, available at <http://ieeexplore.ieee.org/stamp/stamp.jsp?tp=&arnumber=1028951>. 2
- [28] J. Jin, *The Finite Element Method in Electromagnetics*, John Wiley & Sons Inc, 2002. 72, 88
- [29] A. Schneider, *Matrix decomposition based approaches for model order reduction of linear systems with a large number of terminals*, Diploma thesis, Chemnitz University of Technology, Department of Mathematics, April 2008, available at <http://www-user.tu-chemnitz.de/~schnea/Data/diplomarbeit.pdf>.
- [30] K.F. Riley, M.P. Hobson, S. J. Bence, *Mathematical Methods for Physics and Engineering*, Cambridge University Press, 2006. 76

- [31] E. O. Brigham, *The Fast Fourier Transform*, Prentice-Hall, 1974. 76, 77
- [32] G. Pelosi, R. Coccioli, S. Selleri, *Quick Finite Elements for Electromagnetic Fields*, Artech House, 1998. 87, 88
- [33] O. Farle, *Ordnungsreduktionsverfahren für die Finite-Elemente-Simulation parameterabhängiger passiver Mikrowellenstrukturen*, Universität des Saarlandes, Doctorate Thesis, 2007. 2, 86, 89, 113
- [34] P. Monk, *Finite Element Methods for Maxwell's Equations*, Oxford University Press, 2003. 85
- [35] Y. Zhu, A. C. Cangellaris, *Multigrid Finite Element Methods for Electromagnetic Field Modeling*, IEEE Press, Wiley-InterScience, 2006. 87
- [36] J. E. Bracken, D. K. Sun, Z. J. Cendes, *S-Domain Methods for Simultaneous Time and Frequency Characterization of Electromagnetic Devices* IEEE Transactions on Microwave Theory and Techniques, Vol. 46, No. 9, September 1998, available at <http://ieeexplore.ieee.org/stamp/stamp.jsp?arnumber=00709471>. 113
- [37] P.D. Ledger, J. Peraire, K. Morgan, O. Hassan, N.P. Weatherill, *Parameterised Electromagnetic Scattering Solutions for a Range of Incident Wave Angles*, Elsevier, 2004, available at <http://dx.doi.org/10.1016/j.cma.2004.01.032>. 2, 94, 113
- [38] P. Monk, *The Near Field to Far Field Transformation*, COMPEL, The International Journal for Computation and Mathematics in Electrical and Electronic Engineering, Vol 14, No 1, P. 41-56, 1995, available at <http://dx.doi.org/10.1108/eb010137>. 97
- [39] F. Ihlenburg, I. Babuška, *Dispersion Analysis and Error Estimation of Galerkin Finite Element Methods for the Helmholtz Equation*, International Journal for Numerical Methods in Engineering, Vol 38, P. 3745-3774, 1995. 97

- [40] T.H. Chio, D.H. Schaubert, *Parameter Study and Design of Wide-Band Widescan Dual-Polarized Tapered Slot Antenna Arrays*, IEEE Transactions on Antennas and Propagation, vol. 48, no. 6, pp. 879-886, June 2000. 109

